FRONTIERS OF PHYSICS

REVIEW ARTICLE
Volume 18 / Issue 5 / 53603 / 2023

Recent developments in CVD growth and applications of 2D transition metal dichalcogenides

Hui Zeng[1,*], Yao Wen[1,*], Lei Yin[1], Ruiqing Cheng[1], Hao Wang[1], Chuansheng Liu[1], Jun He[1,2,3,4,†]

1 Key Laboratory of Artificial Micro- and Nano-structures of Ministry of Education, and School of Physics and Technology, Wuhan University, Wuhan 430072, China
2 Wuhan Institute of Quantum Technology, Wuhan 430206, China
3 Hubei Luojia Laboratory, Wuhan 430079, China
4 Shanxi Normal University, Taiyuan 030031, China
Corresponding author. E-mail: †He-jun@whu.edu.cn
*These authors contributed equally to the work.
Received December 7, 2022; accepted March 20, 2023

ABSTRACT

Two-dimensional (2D) transition metal dichalcogenides (TMDs) with fascinating electronic energy band structures, rich valley physical properties and strong spin–orbit coupling have attracted tremendous interest, and show great potential in electronic, optoelectronic, spintronic and valleytronic fields. Stacking 2D TMDs have provided unprecedented opportunities for constructing artificial functional structures. Due to the low cost, high yield and industrial compatibility, chemical vapor deposition (CVD) is regarded as one of the most promising growth strategies to obtain high-quality and large-area 2D TMDs and heterostructures. Here, state-of-the-art strategies for preparing TMDs details of growth control and related heterostructures construction via CVD method are reviewed and discussed, including wafer-scale synthesis, phase transition, doping, alloy and stacking engineering. Meanwhile, recent progress on the application of multi-functional devices is highlighted based on 2D TMDs. Finally, challenges and prospects are proposed for the practical device applications of 2D TMDs.

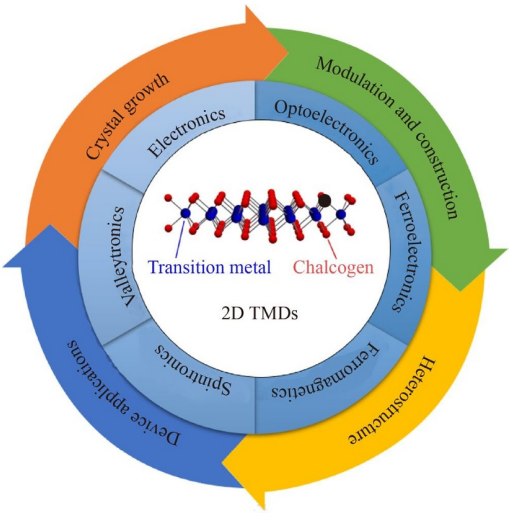

Keywords two-dimensional (2D) semiconductor, transition metal dichalcogenides (TMDs), chemical vapor deposition (CVD), heterostructures, device applications

Contents

Higher Education Press

https://doi.org/10.1007/s11467-023-1286-2

1 Introduction

Two-dimensional (2D) transition metal dichalcogenides (TMDs) have attracted widespread attention in both theoretical studies and practical device applications due to their distinct properties, such as atomically thin geometry, dangling-bond free interface, tunable bandgap, photoresponse properties, spin and valley polarization, superconductivity and ferroelectricity [1–7]. To realize the potential of 2D TMDs, efficient and convenient preparation methods are highly required. Generally speaking, mechanical exfoliation, liquid exfoliation, vapor phase deposition, and molecular beam epitaxy are commonly adopted strategies for the fabrication of 2D TMDs, which can be divided into top-down and bottom-up synthetic approaches. As the representation of top-down synthetic approaches, mechanical exfoliation is first applied to obtain thin-layer 2D materials from bulk [8] due to the weak van der Waals interaction at the interface. However, it is acknowledged that large-scale 2D TMDs are hard to be fabricated through mechanical exfoliation. Moreover, the quality of crystal edge and domain can be hardly controlled during the exfoliation process. Compared with top-down strategies, bottom-up strategies enable the weak interaction of micro particles (such as atoms and molecules) to self-assemble into a relatively large and complex structural system. By controlling the growth conditions, several above-mentioned challenges can be overcome. Molecular beam epitaxy (MBE) is an efficient bottom-up technology for synthesizing high-quality 2D crystal films. High purity sources are evaporated in the ultra-high vacuum ($<10^{-7}$ Pa) reaction vessel and form beams in the form of molecular clusters. Compared with mechanical exfoliation, MBE shows tunability in crystal component and structure. Nevertheless, the shortcomings of MBE are also obvious for costly facilities, complex processes and slow growth rates.

Chemical vapor deposition (CVD) is regarded as the most promising technique for large scale and high-quality growth of 2D TMDs [9]. It is worth mentioning that the morphology, phase, domain size, number of layers, orientation and defect degree in CVD-grown TMDs can be effectively modulated by growth parameters, such as temperature, carrier gas, pressure, growth time, substrate and the ratio of precursors [10–18]. Several researches demonstrate the influence of the parameters from the aspect of thermodynamics and kinetics [19, 20]. For instance, compared with the bilayer counterpart, the monolayer MoS_2 flake in a small lateral size is thermodynamically favorable due to the monolayer preference at the initial stage of nucleation, while the bilayer MoS_2 flake becomes dominant with the increase of lateral size. Through the strong coupling between substrate and TMDs, mono- and bilayer MoS_2 can be adjustable [21]. During the nucleation process via CVD method, growth temperature plays a significant role because the vapor pressures of solid TMD precursors are highly sensitive to temperature. For example, WS_2 epitaxially grows on top of the MoS_2 monolayer to form vertically stacked heterostructures at high temperature, while WS_2 grows on edge of the MoS_2 monolayer to create seamless and atomically sharp lateral heterostructures at low temperature [22]. Since the growth of several high-quality thin films can be only achieved by high-temperature CVD, methods for reducing the melting point of precursors are required, such as adding salts or decreasing growth pressure. Yang *et al.* [23] synthesized 6-inch monolayer MoS_2 on the solid soda-lime glass in the low-pressure CVD growth process. The MoS_2 growth rate on glass substrate is approximately 38 times higher than that on quartz substrate because of the Na adsorption. Density functional theory (DFT) calculations reveal that the energy barriers for MoS_2 growth along the S-terminated edges are evidently reduced with the incorporation of Na, which promotes the formation of large-scale MoS_2. To summarize, the properties of made-up products are sensitive to growth parameters during the CVD process, so the proper design of a growth system in a controllable way is highly required.

Stacking 2D TMDs for constructing artificial functional structures, attractive physical and chemical characteristics in electronic [1, 24, 25], optoelectronic [26, 27], ferroelectronic [28, 29], ferromagnetic [30, 263], spintronic [31, 32] and valleytronic [6, 33, 34] fields may emerge. In general, van der Waals (vdW) interaction is the force that holds hybrid heterostructures between constituent 2D TMD

nanosheets. According to the source of force, the vdW interaction includes three different types: dipole–dipole interaction (orientation force), dipole-induced dipole interaction (induction force) and instantaneous dipole-induced dipole interaction (dispersion force). All the three types of vdW interaction are about 2–3 orders of magnitude weaker than that of ionic or covalent bonds. Therefore, the interface properties can be easily tuned by external factors, such as doping, strain, intercalation, electric and magnetic fields, offering unprecedented opportunities for both theoretical studies as well as adventurous device applications.

Herein, we start with the modulation of 2D TMD crystal growth via CVD method, including wafer-scale synthesis, phase transition, doping and alloy engineering. Then, the stacking engineering for heterostructures is summarized. After that, recent progress on the application of multi-functional devices based on 2D TMDs is highlighted. Finally, the challenges and prospects are proposed for the practical device applications of 2D TMDs.

2 Growth modulation and heterostructure construction

Herein, we conclude several methods for modulating TMD growth via CVD method and constructing nanoscale heterostructures, each of which has its own unique properties. For instance, wafer-scale synthesis provides opportunity for realizing massive and high-end device applications of 2D TMDs; phase transition engineering enhances physical and chemical properties like many-body interaction, modulating bandgap and electron-photon coupling; doping and alloying introduce more defects and activate the active centers of the basal plane and edge sites. The construction of vertical and lateral heterostructures regulates the relative formation energy in the interfaces between two or more different materials and emanates massive interesting physical phenomena. Below, we will give several concrete examples to introduce methods for growth modulation and heterostructures construction.

2.1 Wafer-scale synthesis

Chemical vapor deposition (CVD) growth of wafer-scale single-crystalline two-dimension transition metal dichalcogenides (TMDs) is of great importance in electronics, optoelectronics, spintronics, valleytronics, etc. To completely realize massive and high-end device applications of 2D TMDs, fast growth speed and high-quality single-crystalline are two main challenges up to now. Based on relevant studies in regard to growth dynamics, faster growth of domains would further lower the appearance of new nuclei for shorter growth time and higher coverage. The introduction of oxygen to the growth environment has been shown to accelerate the decomposition of hydrocarbons and edge deposition of carbon [10]. Apart from oxygen, fluorine released from the decomposition of metal fluorides can play a more efficient role to increase the growth rate of 2D materials. Liu *et al.* [11] placed the WO_3 powder on the BaF_2 substrate. When the temperature rose, the fluorine released by the BaF_2 substrate participated in the reaction and significantly enhanced the growth of WS_2 seeds [Fig. 1(a)]. The domain size of WS_2 increased from ~1 μm to ~100 μm and the growth rate increased from 0.2 $\mu m \cdot min^{-1}$ to 20 $\mu m \cdot min^{-1}$, while star-like WS_2 domains formed without a fluorine supply for the same time [11] [Figs. 1(b, c)]. This method of accelerating formation of crystal seeds via self-capping vapor-liquid-solid can be also applied in the growth of other large-scale 2D TMDs such as WSe_2 [35] and MoS_2 [36], which turns out to be a universal kinetic and thermodynamic modulation method for growth promotion. Another challenge in the wafer-scale CVD growth of 2D TMDs is to grow high-quality single crystals. To solve this problem, there are two mainstream strategies. One is to control the precursors so that only one nucleus forms and grows up. The other is to control all the nuclei that have the same orientation. It is acknowledged that 2D domains with the same orientation can seamlessly stitch into an entire single-crystalline piece. And the core idea is to regulate the interplay between domains and the single-crystalline substrates [37]. Unlike graphene [38–40] and hexagonal boron nitride growing on metal surfaces [41], 2D TMDs single crystal films are difficult to grow on wafer-scale insulating substrates because of substantial differences in growth kinetics. The challenge mainly comes from the non-centrosymmetric C_{3v} lattice of TMDs, which leads to nonparallel domain orientation on most high-symmetry substrate surfaces. To solve this problem, Wang *et al.* [9] took advantage of a new mechanism of double coupling coordinated regulation of in-plane van der Waals coupling and step interaction between 2D TMDs and insulating substrates. The sapphire substrates were first annealed in oxygen atmosphere to stabilize the parallel atomic steps, which broke the C_2 symmetry of α-plane sapphire and guide the unidirectional alignment of WS_2 islands for the epitaxial growth of the single-crystal monolayer film [Fig. 1(d)]. The coupling between WS_2 and α-plane sapphire induced WS_2 islands to grow along two energetically degenerated antiparallel alignments. And the coupling between WS_2 and step edges of sapphire broke the degeneracy of two antiparallel alignments of WS_2 islands on the α-plane sapphire surface so that the domain retained only one dominant orientation. Researchers used a series of characterization techniques from macroscopic scale to atomic scale to confirm the single nuclei orientation in the two-inch monolayer firms.

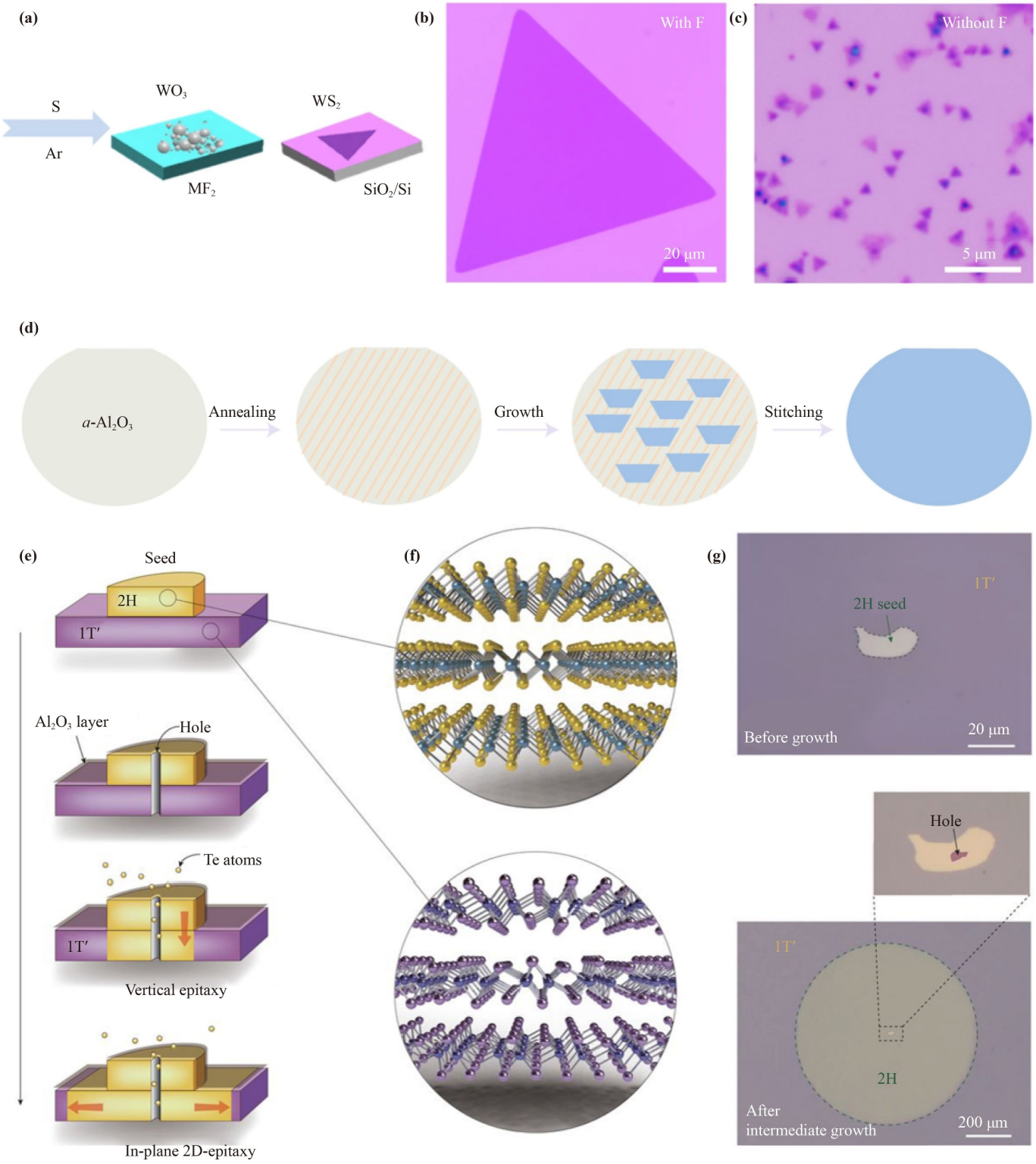

Fig. 1 CVD growth of wafer-scale single-crystalline 2D TMDs. **(a)** Schematics of the experimental design for WS_2 growth; the WO_3 precursor powder is directly placed on a BaF_2 substrate. **(b, c)** Optical images of the WS_2 domains on SiO_2/Si substrates with **(b)** and without **(c)** a fluorine supply for the same growth time. **(d)** Schematic of the growth process of a WS_2 monolayer on vicinal a-plane sapphire. **(e)** Schematic diagrams for the in-plane 2D-epitaxy synthesis of wafer-scale single-crystalline 2H-$MoTe_2$ thin film. **(f)** Optical image of a 2H-$MoTe_2$ nanoflake assembled in the center of the 1T′-$MoTe_2$ wafer as a seed to induce the phase transition and recrystallization. **(g)** Optical image of the wafer after intermediate growth at 650 °C for 2 hours. Inset shows the seed crystal with a needle probe-punched hole. (a–c) Reproduced with permission [11]. Copyright © 2019, Springer Nature. (d) Reproduced with permission [9]. Copyright © 2021, Springer Nature. (e–g) Reproduced with permission [44]. Copyright © 2021, The American Association for the Advancement of Science.

At present, most studies of the wafer-scale single-crystal 2D TMDs growth focus on nucleation at different sites and regulating the interface between domains and substrate surface; however, both of the two strategies cannot make sure 100% 2D film coverage, which limits industrial implementation of 2D semiconductors for next-generation nanoelectronics. Phase transition proves to be a nonnegligible method for growth of wafer-scale single-crystal 2D TMDs. Taking $MoTe_2$ as an example, the free energy difference between semiconducting 2H phase and metallic 1T′ phase (~40 meV per $MoTe_2$ formula unit) [42] is small enough to realize phase transition in a wafer-scale large. DFT calculations confirm that the 1T′ phase is more stable phase when the Te deficiency is larger than 2% [43], so 1T′-$MoTe_2$ phase was first formed. As increasing growth time, 2H-$MoTe_2$ circles emerged, grew up and finally formed a uniform 2H-$MoTe_2$ film. Xu *et al.* [44] first prepared a polycrystalline 1T′-$MoTe_2$ wafer, and a single-crystal 2H-$MoTe_2$ nanoplate was placed on the surface of 1T′-$MoTe_2$ wafer as the seed. A needle probe-punched hole was created for Te atoms supply. The phase transition process was driven by Te atom diffusion and formed an in-plane 2H/1T′ $MoTe_2$ heterostructure [Fig. 1(e)]. After a long-term growth, the entire film transformed into 2H phase with continuous, smooth and uniform surface [Figs. 1(f, g)]. It is worth noting that the whole in-plane phase transition process is accompanied by recrystallization with 2H-$MoTe_2$ as the template, so that the lattice structure and lattice orientation of the whole film after phase transformation are completely consistent with the single-crystal seed [44].

Currently, 2D devices based on wafer-scale TMDs mainly concentrate on electronics, optoelectronics, spintronics and catalysis. In digital electronic device applications, the field-effect-transistor (FET) is the most basic and significant component with the function of a switch, which means two terminals (source and drain) must be short-circuit or open-circuit whenever the voltage applied to the gate is larger than the threshold voltage [45]. Mobility (μ) and on/off ratio (I_{on}/I_{off}) are usually used as figures of merit to evaluate electronic device performance. Mobility (μ) affects the conductivity of semiconductor materials and the working frequency of devices. Improving μ can reduce the power consumption, improve the current carrying capacity and enhance the switching speed of FET. Generally speaking, devices for high-performance applications have high switching speed while possessing high power dissipation, even in standby. Therefore, higher I_{on}/I_{off} ratio can bring more effective switching and lower power consumption. The I_{on}/I_{off} ratio needs to be larger than 10^4 for future device generations [46]. Among TMDs, MoS_2 is an excellent semiconductor for its magnificent charge transport [47] and direct moderate bandgap [48] (1.8 eV for monolayer) so that it has become the most investigated 2D materials for realizing future-generation FETs. Li *et al.* [49] fabricated transparent MoS_2-based transistors and logic circuits on flexible substrates using 4-inch wafer-scale MoS_2 monolayers. 4-inch monolayer MoS_2 was epitaxially grown on sapphire via traditional powder chemical vapor deposition with only two crystal orientations: 0° and 60°. These wafer-scale MoS_2 monolayers on sapphire were transferred onto PET substrates pre-deposited with 30-nm indium tin oxide (ITO, serving as the back-gate electrode layer) and 35-nm aluminum oxide (serving as the dielectric layer) on the top to enable further device fabrications. The device obtained magnificent mobility (~55 $cm^2 \cdot V^{-1} \cdot s^{-1}$) and I_{on}/I_{off} ratio (10^{10}) performance compared with other large-scale flexible transistors [Fig. 2(a)]. Furthermore, the superior mobility and I_{on}/I_{off} ratio preserved after 10^3 cycled tests of bending and releasing [Fig. 2(b)], which proved the reliability of MoS_2-based transistors. Moreover, Seol *et al.* [50] prepared 6-inch wafer-scale monolayer MoS_2 and WS_2 via rapid metal-organic chemical vapor deposition (MOCVD) and fabricate high-performance FETs [Fig. 2(c)]. All the 900 FET devices showed a high I_{on} of 1.1 ± 0.1 μA, an extremely low I_{off} of 32.0±3.0 fA, a high I_{on}/I_{off} ratio of 10^7 and field-effect mobility μ_{FE} of 3.4 $cm^2 \cdot V^{-1} \cdot s^{-1}$ uniformly [Fig. 2(d)]. It provides a route for high-throughout, scalable production and low-temperature back-end-of-line (BEOL) integration into Si CMOS platforms.

Emblematic optoelectronic devices include photodetectors, light emitting device (LED) and photovoltaics. The most devices based on wafer-scale 2D TMDs so far are photodetectors [51]. Zeng *et al.* [52] synthesized wafer-scale $PdTe_2$ film by depositing Pt metal layers on SiO_2/Si using magnetron sputtering system and selenization via powder CVD. The $PdTe_2$/Si photodetector was fabricated by etching and photolithography. Solution-processable black phosphorus quantum dots (BPQDs) were decorated onto top surface of the $PdTe_2$ film by spin-coating method to synthesize hybrid structure [Fig. 2(e)]. After decoration, BPQDs@$PdTe_2$/Si heterojunction photodiode performed a high responsivity (300.2 $mA \cdot W^{-1}$) and specific detectivity (~10^{13} Jones). In addition, the response speed of 38/44 μs is faster than that of graphene/Si Schottky junction (93/110 μs [53]), comparable with that of MoS_2/Si heterojunction (30.5/71.6 μs [54]) in previous researches. Apart from this, the photocurrents are all enhanced by 1–2 folds under deep ultraviolet (DUV), near-infrared light (NIR) and mid-infrared light (MIR) illuminations compared with those without BPQDs decoration [Fig. 2(f)], which may result from the defects in the BPQDs.

The density of state (DOS) of metallic TMDs shows two main properties: (i) The Fermi level of the undoped material is always crossing a band with d-orbital character and (ii) the DOS at the Fermi level is usually quite high, which hints at a common explanation for the phase

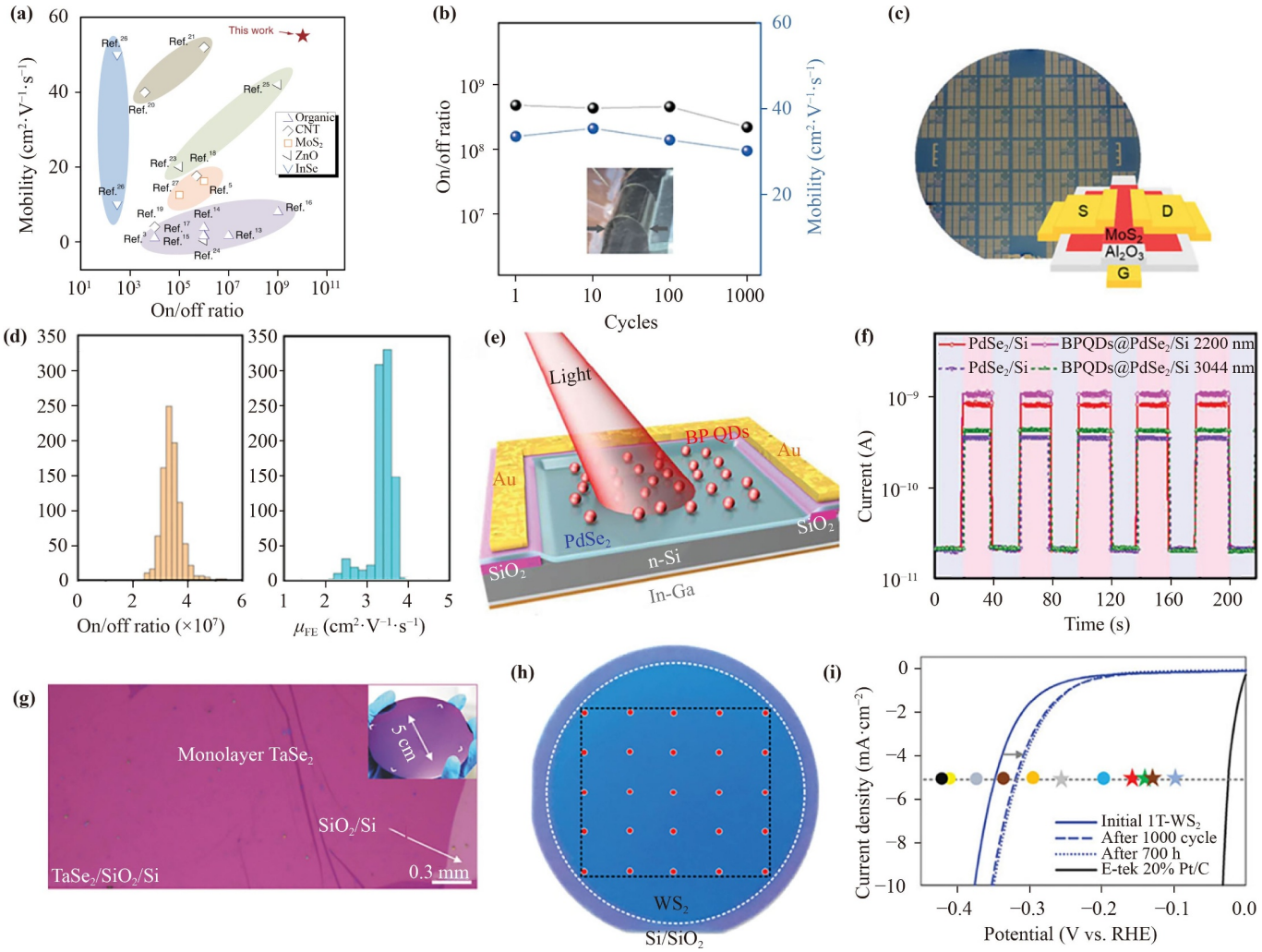

Fig. 2 2D devices based on wafer-scale TMDs. **(a)** The on/off ratio and mobility of FETs based on 4-inch monolayer MoS_2 compared with various large-area flexible transistors reported in the literature. **(b)** The on/off ratio and charge-carrier mobility of a device subjected to 10^3 cycled tests of bending and releasing. Inset: Photograph of flexible devices at 1% strain. **(c)** Photograph of the batch-fabricated MoS_2-based FETs on a 6-inch wafer. Inset: Schematic of the MoS_2-based FET. **(d)** Histograms showing the distribution of on/off ratio and μ_{FE} for the 900 FETs. **(e)** Schematic illustration of PdS_2/Si detector. **(f)** 2200 nm (150 mW·cm^{-2}), and 3044 nm (100 mW·cm^{-2}) light illumination at 0 V. **(g)** Large scale optical image of centimeter-size monolayer 2H-$TaSe_2$ film on SiO_2/Si substrates. **(h)** Photograph of wafer-scale 1T-WS_2 with the 25 points used for the Raman mapping image, indicated by the red circles. **(i)** Electrochemical HER performance before and after 1000 cycles at 100 mV·s^{-1} for 1T-WS_2 with a potential shift η from –0.39 to –0.32 V at 10 mA·cm^{-2}. The stars and circles indicate previously reported results. (a, b) Reproduced from Ref. [49]. Copyright © 2020, Springer Nature. (c, d) Reproduced from Ref. [50]. Copyright © 2020, Wiley-VCH. (e, f) Reproduced from Ref. [52]. Copyright © 2018, Wiley-VCH. (g) Reproduced from Ref. [56]. Copyright © 2018, Wiley-VCH. (h, i) Reproduced from Ref. [12]. Copyright © 2020, Wiley-VCH.

transitions [55]. However, charge-density-wave (CDW) order exists in 2D metallic TMDs due to the limit of scale and thickness. Shi *et al.* [56] directly synthesized wafer-scale uniform monolayer 2H-$TaTe_2$ films and thickness-tunable flakes on Au foils by atmospheric pressure CVD (APCVD) method [Fig. 2(g)]. Based on the thickness-tunable 2H-$TaSe_2$, the robust periodic lattice distortions which transferred from normal metallic to CDW orders were directly visualized by low-temperature transmission electron microscopy. With decreasing thickness from ~15 nm (about 20 layers) to ~0.8 nm (monolayer), the CDW phase transition temperature increased from ~90 to ~125 K, which was consistent with detailed DFT calculation and similar tendencies like $NbSe_2$ and $TiSe_2$ layers [57, 58]. It highlights the possibility to integrate wafer-scale TMDs material into the spintronic applications.

In addition to above applications, electrocatalysis for stable hydrogen evolution reaction (HER) is an assignable highlight based on wafer-scale 2D TMDs. The metallic 1T-WS_2 can be used as an efficient electrocatalyst for HER relying on its boost charge transfer between the

electron source and active edge sites. Kim *et al.* [12] synthesized wafer-scale 1T-WS_2 via a plasma-enhanced CVD (PECVD) system. Compared with CVD, the PECVD is low-temperature (150°C) and has faster deposition rate. 1T-WS_2 seed was deposited on a 4-inch wafer of SiO_2/Si or plastic substrate using an e-beam evaporator. Then the substrate was heated to 150°C in an Ar atmosphere, and the sulfurization of the W film was treated under H_2S and Ar plasma (10:10 sccm), chamber pressure (100 mTorr), and plasma power (550W) for 1.5h, resulting in a uniform 1T-WS_2 film [Fig. 2(h)]. As for the electrocatalytic behavior, the onset overpotential (η) and initial Tafel slope of the 1T-WS_2 film at 5 mA·cm^{-2} were 0.35 V and 95 mV·dec^{-1}. The Tafel slope suggests the HER can take place through the Volmer mechanism, which indicates the overall reaction occurs by the reduction of H_3O^+ ions and electrochemical adsorption of H on the surface [Fig. 2(i)].

On the whole, many challenges still need to be overcome in the CVD growth of wafer-scale 2D TMDs. Up to now, only graphene and h-BN have been reported for meter-scale single-crystal growth on metal or sapphire substrates with proper surface symmetry by CVD method [40, 59]. The gap of sub-meter single-crystal 2D TMDs growth still needs to be filled. And currently, the wafer-scale TMDs growth is largely about group VIB WS_2 and MoS_2. More other wafer-scale 2D TMDs like ferromagnetic and ferroelectric materials have not been reported for wafer-scale growth by CVD, and the wafer-scale alloy TMDs like $WSe_{2-x}S_x$ or "Janus" TMDs like Mo–S–Se [60] are also worthy studying. Different from graphene and h-BN, TMDs have various metastable phases, and it is very significant to control the single phase growth. Furthermore, it still awaits more investigation to lower the nucleation densities, increase the grain size and control the stitching of the grains in the wafer-scale TMDs growth. To solve above problems, we long for the combination of theoretical calculation and growth technologies. With the formation of a complete model of wafer-scale TMD growth by CVD, massive and high-end device applications will soon be realized in the near future.

2.2 Phase

The different phases of TMDs have attracted colossal interests in the past decade. On account of their enhanced physical properties through many-body interaction, direct bandgap and electron-photon coupling, phase transitions like polymorphic, ferroic and high-temperature diffusive phase changes can be applied into charge-density-waves (CDW), ferromagnetism, high-T_c superconductivity, the quantum spin Hall effect and the quantum anomalous Hall effect via CVD method.

The theory of 2D phase transition mainly comes from the exact solution of the 2D Ising spin model [61], the proposition of the Hohenberg–Mermin–Wagner theorem [62, 63] and the discovery of the Kosterlitz–Thouless transition [64, 65]. Most 2D phase transition TMDs are MX_2 structures, which have an X–M–X arrangement with three layers. Monolayer MX_2 has three structural polymorphs: 2H, 1T and 1T′ [66, 67] [Fig. 3(a)]. The 2H phase has a trigonal prismatic pattern and the sequence of 2H phase MX_2 is ABA (A represents chalcogen elements like S, Se, or Te, and B represents a transition metal). The 1T phase has an octahedral pattern and can be considered as a result of the horizontal shift from the initial position of one of the sulfur atomic layers in the 1H phase MX_2. Through the distortion of 1T phase MX_2, a 1T′ (1T″ and 1T‴) phase can be obtained. The phase transition of 2D TMDs can be considered to tune electron band structures in the Brillouin zone or change the density of electrons. The transition of TMDs from 2H phase to 1T or 1T′ phase can be induced by physical factors like temperature [68], strain [69], laser irradiation [70], electrostatic doping [71], plasma [72, 73] and electric fields [3] and chemical factors (intercalation of alkali metals [13]). Hou *et al.* [69] switched $MoTe_2$ between the 1T′-$MoTe_2$ (semimetal) phase and the 2H-$MoTe_2$ (semiconductor) phase reversibly with an electric-field-induced strain in field-effect transistor geometry [Fig. 3(b)]. Through the thin-film stress induced by the contacts, the non-conductive regions near the contacts were closed, showing a higher conductivity, which was measured via conductive atomic force microscopy (CAFM) [Fig. 3(c)]. The channel conductivity changed greatly (G_{on}/G_{off}~10^7 versus G_{on}/G_{off}~0.04 in the control device) due to non-volatile strain phase transition at room temperature. Zhu *et al.* [73] found that a weak Ar-plasma bombardment could locally induce 2H→1T phase transition in monolayer MoS_2 to form mosaic structures. Weak Ar-plasma wrenched the S–Mo bond to induce the lateral sliding of the top S-layer and transferred the 2H semiconducting phase to a 1T metallic phase [Fig. 3(d)]. Lin *et al.* [13] created butterfly-like single crystals with the 1T-WS_2 in one wing and the 2H-WS_2 in the other through the reduction of the energy barriers due to the adsorption of Na atoms on WS_2 [Fig. 3(e)]. The 1T structure was thermodynamically stable, which even persisted at a high temperature of above 800 °C, allowing for a stepwise edge epitaxy of lateral 1T heterostructures. It has been investigated that the mechanism of alkali metal inducing phase transition from 2H to 1T should be imputed to the electron transfer from the intercalated alkali metal ions leading to an increased electron count on the d-orbitals of TMDs [74].

2D TMD materials with phase transitions enable the construction of nanoscale flexible devices with potential usages in electronics, optoelectronics, ferroelectrics, ferromagnets and high-T_c superconductivity. Among emerging memory devices, phase-change material (PCM)-based random access memories (PRAMs) are considered

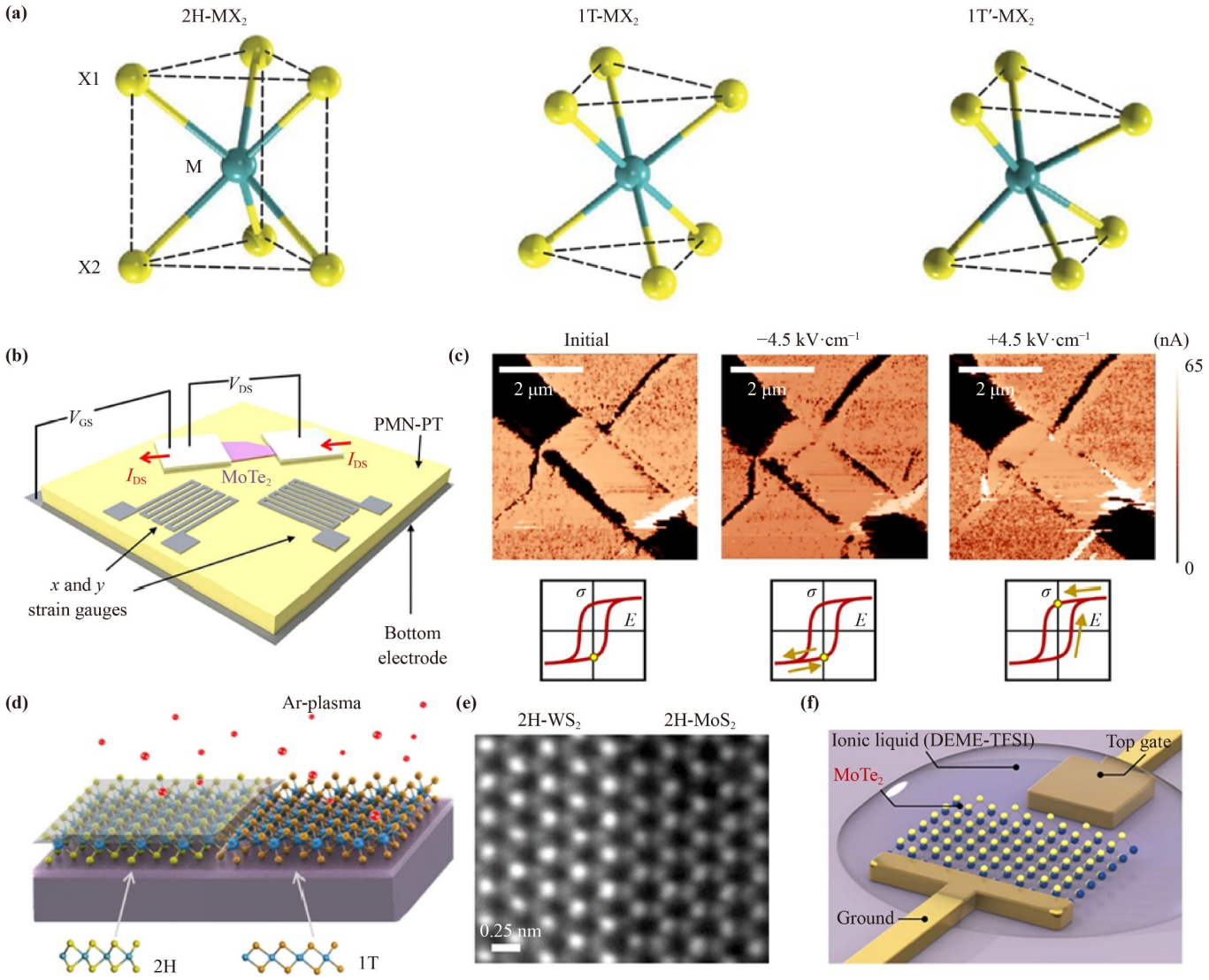

Fig. 3 Phase transition in 2D TMDs. **(a)** Three structural polymorphs (2H, 1T and 1T′ phases) of MX_2 monolayers. M represents (Mo, W) and X represents (S, Se, Te). **(b)** Schematic representation of the strain-based $MoTe_2$ ferroelectric phase change field-effect transistor. **(c)** CAFM images after a pulse sequence representing the initial condition (left), then a pulse in the same direction as polarization (middle) and finally a pulse in the opposite direction as polarization (right). **(d)** Schematic representation of the plasma-treated process for 1T-MoS_2. **(e)** High-resolution ADF image of the WS_2–MoS_2 lateral heterojunction in 2H phase. **(f)** Schematic diagram of an electrostatic-doping-driven structural phase transition in a $MoTe_2$ monolayer FET. (a) Reproduced from Ref. [67]. Copyright © 2021, Springer Nature. (b, c) Reproduced from Ref. [69]. Copyright © 2019, Springer Nature. (d) Reproduced from Ref. [73]. Copyright © 2017, American Chemical Society. (e) Reproduced from Ref. [13]. Copyright © 2018, American Chemical Society. (f) Reproduced from Ref. [71]. Copyright © 2017, Springer Nature.

as the most mature application. To store switching signals, PRAMs take advantage of the huge contrast between the electrical resistance of high-resistance amorphous phases (0) and low-resistance crystalline phases (1). Conventional PCMs like $Ge_2Sb_2Te_5$ (GST) and $Ag_4In_3Sb_{67}Te_{26}$ (AIST) can be rapidly and reversibly switched, which are originated from the applied voltage pulse via Joule heating. However, to obtain a high switching speed, conventional PCMs usually require a relative high programming current/voltage and relatively high temperature. The application of 2D TMDs in phase transition memories has given a sight to performance improvement and new phase change mechanisms. Different from traditional PCMs, the resistance switching of 2D TMD-based phase change random-access memories does not involve the melting or crystallization process. For example, Zhang *et al.* [71] demonstrated an electrostatic-doping-driven phase transition between the hexagonal and monoclinic phase of $MoTe_2$. As shown in Fig. 3(f), the $MoTe_2$ monolayer is covered by a drop of ionic liquid (DEME-TFSI), which can manipulate the electron population in $MoTe_2$, resulting in a structural transition

between the 2H and 1T′ phases. In addition, melting-free PCMs such as $GeTe/Sb_2Te_3$ superlattices [76] and MnTe [77] have been reported for low-energy and fast-switching memories, providing a possibility for the materialization of optically-driven, exceptional and fast nonvolatile memory based on 2D TMDs.

In summary, we reviewed three most popular structural phases of monolayer MX_2, the means of realizing phase transition including physical and chemical factors as well as related device applications based on phase transition. The CVD growth method is considered to be a versatile route of phase transition for its relatively low temperature and flat crystal surface. However, the polymorphic TMDs of metallic or semimetallic phases are usually in a metastable structure, so their phase transition is usually reversible. Meanwhile, for 2D ferromagnetic/antiferromagnetic materials, there are only a few reports in which the 2D forms are mainly obtained through chemical vapor transport (CVT) and mechanical exfoliation such as $Cr_2Ge_2Te_6$, Fe_3GeTe_2 and CrI_3. For practical applications, more abundant and higher-quality 2D phase transition materials via CVD are highly desired.

2.3 Doping

2D semiconductors exhibit a tunable electrical conductivity between those of insulators and conductors. Doping, a process of introducing charge carriers into semiconductors, is considered as an effective method to control electrical conductivity. For conventional 3D semiconductors like silicon, doping is widely and reliably achieved by introducing impurity atoms to create either free electrons or holes. However, it is intrinsically difficult to control the electronic properties of the 2D TMDs by incorporating impurity dopants due to the limited physical space in the atomically thin lattices [78]. At present, two main strategies are used for doping engineering and the functionalization of 2D TMDs, namely (i) substitutional doping in the growth process and (ii) carrier concentration control in the device fabrication process.

2.3.1 Substitutional doping

In 2D TMDs, both cationic and anionic elements can be substitutionally replaced by external atoms with similar sizes [79, 266–269]. N-type or p-type conductance depends on the number of valence electrons in the dopant atoms. The effect of valence electrons on whether the dopant atoms act as donors or acceptors is determined by the electron density of states (DOS). Taking MoS_2 as an example, the formation energy of S vacancy is more negative than that of Mo vacancy. When electronic states below the conduction band minimum are introduced by dopant elements with more valence electrons like Re, Ru and Rh, it results in n-type doping. Comparatively, when dopant elements are with fewer valence electrons like Y, Zr and Nb, it results in p-type doping. Therefore, it is significant to realize cationic and anionic substitutional doping. For cation substitutional doping, foreign metal elements are usually introduced by tuning the source composition and the growth environment. CVD growth is considered to be an effective method to realize dopant incorporation at cation sites. Zhang *et al.* [80] demonstrated the in situ Re doping of monolayer MoS_2 via CVD with a relatively high doping concentration (1 at%), resulting in nearly degenerate n-type doping [Fig. 4(a)]. R-plane sapphire was used to limit substrate film charge transfer. Gao *et al.* [14] doped atomically thin monolayer WS_2 and MoS_2 with Nb and Re through low-pressure chemical vapor deposition (LPCVD). By recording W and Nb atoms along the line in STEM images, the intensity profiles simulated based on W–Nb–W (red line) fit well with the experimental data, while they did not match with the simulated Cl intensity, confirming that Nb, rather than Cl (from the $NbCl_5$ precursor), was the dopant [Fig. 4(b)].

However, approaches for the substitutional doping of TMD cations often exhibit the loss of semiconductor characteristics, a low carrier concentration and instability. By contrast, anion substitutional doping can be more conveniently achieved [261]. Plasma treatment emerges as an effective doping technique for few-layer MoS_2 due to a wide level of doping, which can be obtained with modulation and selectivity. In 2016, Nipane *et al.* [81] reported a CMOS compatible, controllable and area-selective CMOS phosphorus plasma immersion ion implantation (PIII) process for the p-type doping of MoS_2, whose field effect hole mobility reached 8.4 and 137.7 $cm^2 \cdot V^{-1} \cdot s^{-1}$ respectively for degenerately- and non-degenerately-doped transistors after correcting contact resistance. In addition, the absolute rectification ratio of the diode reached 2×10^4 when combined with lithography patterning. However, plasma treatment may damage the semiconductor crystal structure of monolayer or few-layer TMDs due to the accompanying etching effect caused by the energetic ions. Tang *et al.* [82] developed a method for the effective and reliable p-type doping of monolayer and few-layer WS_2 FETs after N treatment by introducing a perpendicular electric field to restrain energetic ions [Fig. 4(c)]. As a result, the monolayer N-WS_2 FETs showed a hole mobility of 0.53 $cm^2 \cdot V^{-1} \cdot s^{-1}$ and a positive threshold voltage of 9 V without correcting the contact resistance [Fig. 4(d)].

The successful fabrication of Janus TMDs, a sandwich structure with chalcogenide anions of broken symmetry, such as MoSSe and WSSe, has showed novel properties like Rashba spin splitting, vertical piezoelectricity and a long exciton lifetime [83]. In 2017, a Janus TMD monolayer was fabricated through two different strategies. Lu *et al.* [84] stripped the top-layer S atoms through H plasma treatment first and switched off the plasma. Se powders

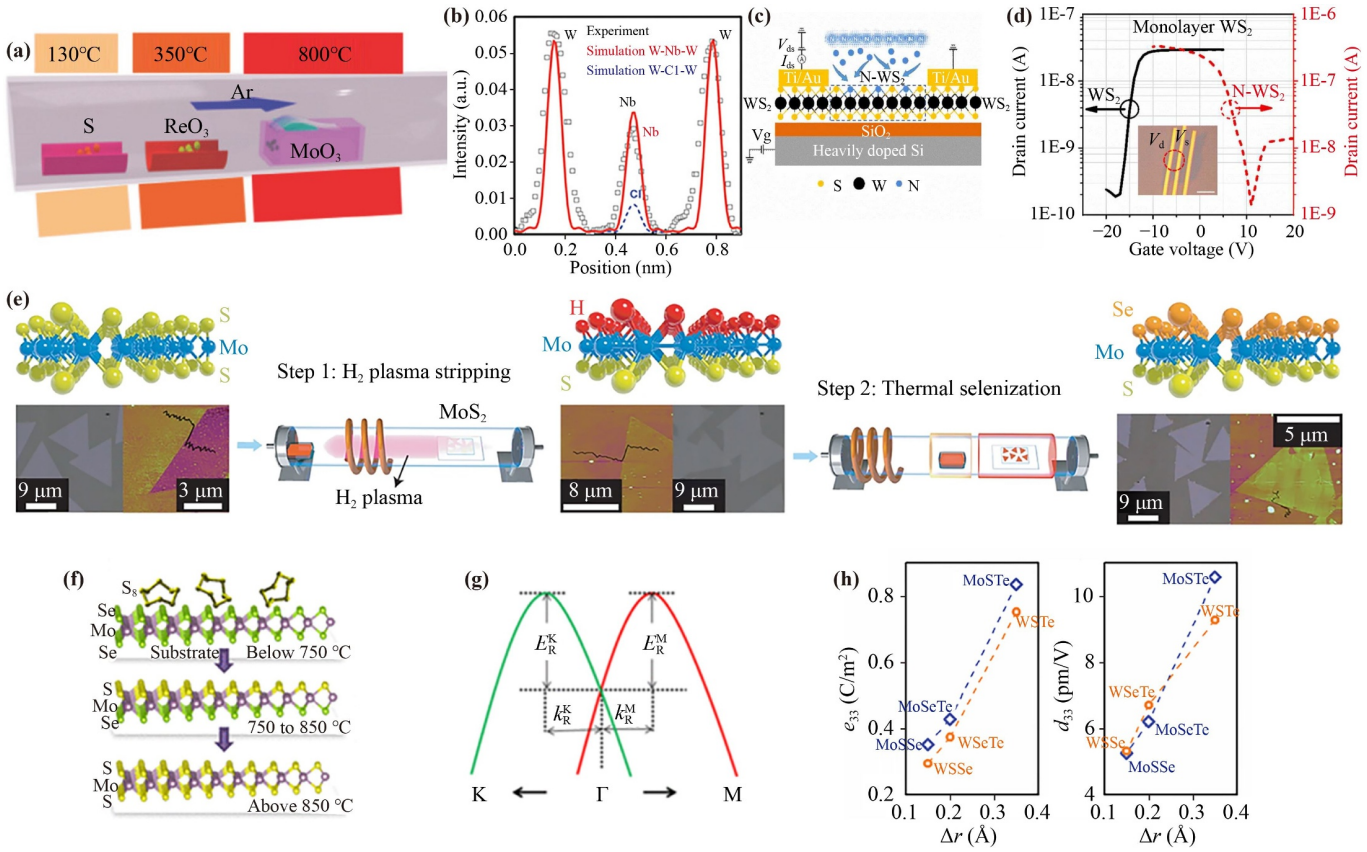

Fig. 4 Substantial doping engineering of 2D TMDs. **(a)** Schematic presentation for the monolayer Re-doped MoS_2 synthesis. **(b)** Intensity line profile of the Z-contrast image (black squares) recorded along the spectrum line shown in STEM image from monolayer Nb-doped WS_2. The simulated Z-contrast intensity profile based on W–Nb–W (red line) fit well with the experimental data, while the simulated Cl intensity (dashed blue line) does not match. **(c)** Cross-sectional view of bottom-gated monolayer and few-layer WS_2 FETs with Ti/Au contacts. **(d)** Drain current versus gate voltage transfer characteristics at a fixed drain voltage of 1 V for the pristine few-layer WS_2 FETs and N-WS_2 FETs with gate voltage sweep from OFF state to ON state. The inset is the optical image of an FL WS_2 FET with a channel width of 15.2 μm and length of 11.5 μm; scale bar is 10 μm. **(e)** Schematic diagram of two-step synthesis of the Janus MoSSe monolayer. **(f)** Proposed reaction mechanism for the sulfurization of monolayer $MoSe_2$ on a SiO_2/Si substrate at different temperatures. **(g)** Schematic view of the Rashba spin splitting around the Γ point in monolayer WSSe. **(h)** Correlation of e_{33} (left) and d_{33}(right) of multilayer MXY structure with Δr, X=Mo, W; Y=S, Se, Te. (a) Reproduced from Ref. [80]. Copyright © 2018, Wiley-VCH. (b) Reproduced from Ref. [14]. Copyright © 2016, Wiley-VCH. (c, d) Reproduced from Ref. [82]. Copyright © 2018, American Chemical Society. (e) Reproduced from Ref. [84]. Copyright © 2017, Springer Nature. (f) Reproduced from Ref. [85]. Copyright © 2017, American Chemical Society. (g) Reproduced from Ref. [86]. Copyright © 2018, American Physical Society. (h) Reproduced from Ref. [87]. Copyright © 2017, American Chemical Society.

were thermally vaporized to achieve the selenization without breaking the vacuum [Fig. 4(e)]. The other strategy was a one-step method based on monolayer $MoSe_2$ [85]. By strictly controlling the temperature and the atmospheric pressure, the top-layer selenium atoms were substituted by S atoms while the bottom layer was not sulfurized [Fig. 4(f)]. The obtained SMoSe layer obtained and its reverse configuration SeMoS exhibited a slightly strengthened hydrogen evolution reaction efficiency. Both synthetic approaches resulted in uniformly asymmetric structures and showed a vertical broken symmetry, which offered new opportunities for future application. For instance, in conventional TMD monolayers, a strong Rashba SOC would not arise due to the out-of-plane inversion symmetry. However, in Janus TMDs, the Rashba-type spin splitting can be observed without external electric fields [86] [Fig. 4(g)]. Another significant feature of Janus TMDs is their vertical piezoelectric polarization. Dong *et al.* [87] found a strong out-of-plane piezoelectric polarization in multilayer MoSTe by introducing a uniaxial strain in the basal plane, regardless of the stacking sequence. The out-of-plane coefficient d_{33} reached 13.5 pm/V, which was larger than that of AlN (d_{33} = 5.6 pm/V) [Fig. 4(h)], a commonly-used 3D piezoelectric material. The strong vertical piezoelectric effect of Janus TMDs may make them well suited for piezoelectric sensors and detecting devices. In summary, the specifically substitutional anion doping

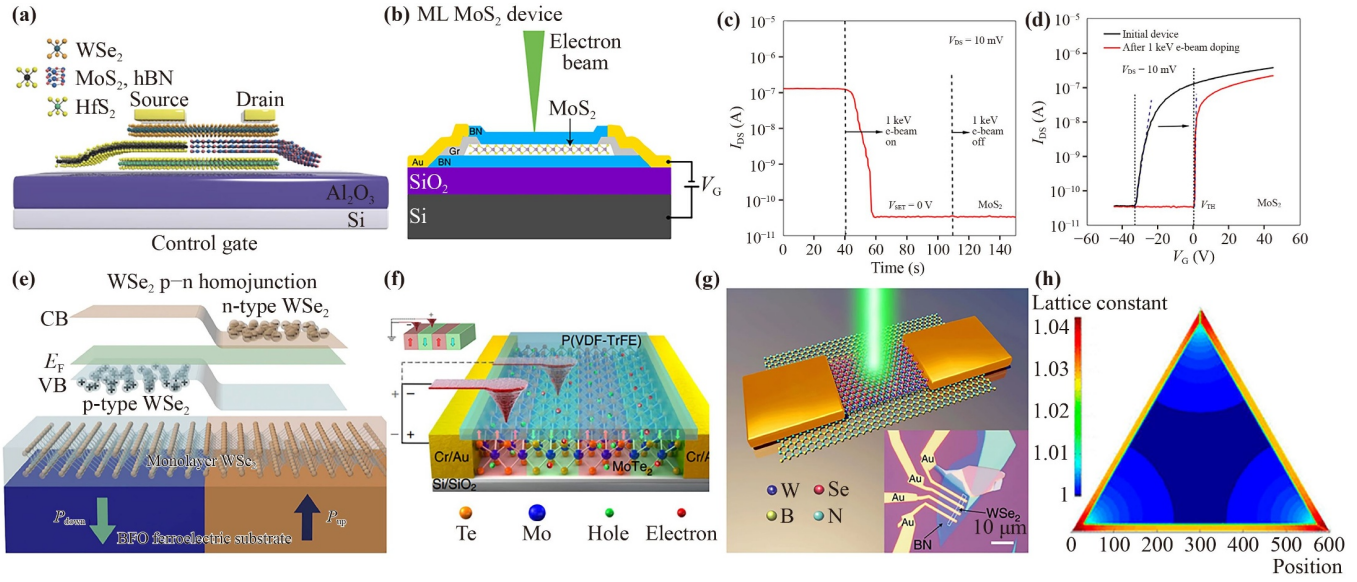

Fig. 5 Carrier concentration doping engineering of 2D TMDs. **(a)** Schematic structure of the 2D semi-floating gate memory. The 2D materials WSe_2, h-BN and HfS_2 serve as the channel, blocking layer and the floating gate. In addition, the inserted MoS_2 layer and the WSe_2 channel form the p–n–junction switch. **(b)** Cross-section view of the experimental scheme for electron-beam doping in BN-encapsulated ML MoS_2 transistor device with multilayer graphene contacts. **(c)** Source-drain current I_{DS} change in ML MoS_2 when a 1 keV electron beam is switched on and off with V_G set to 0 V. **(d)** $I_{DS}(V_G)$ of ML MoS_2 before and after electron beam exposure. **(e)** Schematic band diagram of a WSe_2 p–n homojunction derived from a ferroelectric-pattern-assisted BFO layer. **(f)** A schematic of the periodic $MoTe_2$ lateral p–n–p–n homojunction tuned using ferroelectric domains. Insert: Ferroelectric domains of P(VDF-TrFE) locally manipulated by the voltage applied to the probe. **(g)** A schematic illustration of the optoelectronic memory fabricated by transferring WSe_2 flake on BN flake. Insert: optical image of the WSe_2–BN heterostructure. **(h)** Lattice constant in different positions while the outermost S atoms are substituted by Se atoms (left). The relations between the occupation of the substituted Se atoms, lattice constant, and substitution barrier (right). (a) Reproduced from Ref. [88]. Copyright © 2018, Springer Nature. (b–d) Reproduced from Ref. [89]. Copyright © 2020, Springer Nature. (e) Reproduced from Ref. [90]. Copyright © 2018, Springer Nature. (f) Reproduced from Ref. [91]. Copyright © 2020, Springer Nature. (g) Reproduced from Ref. [93]. Copyright © 2018, Springer Nature. (h) Reproduced from Ref. [96]. Copyright © 2018, American Chemical Society.

reveals the potential of utilizing device applications with novel properties.

2.3.2 Carrier concentration control

In contrast to substitutional doping by introducing impurity atoms to create either free electrons or holes, the charge transfer interaction between host materials and any adjacent medium is made use of in carrier concentration control during the device fabrication process, which is considered to be more nondestructive and reversible. Popular alternative approaches comprise electrostatic doping, photo-induced doping and strain-induced doping. Electrostatic doing is usually achieved through the modulation of carrier concentration and by typing in different regions of the same materials via a floating gate or ferroelectric polarization. Based on the quantum tunneling effect of electrons, tunneling diodes with a metal–insulator–semiconductor structure provide possibility for the reversible electrostatic doping of 2D TMDs with a floating gate. If the drain voltage is larger than the gate voltage, the carrier would tunnel through the insulating layer to the gate. When electrons are trapped in the floating gate, the semiconductor channel is p-doped with the same number of holes. On the contrary, the trapped charges would be accumulated over the entire semiconductor channel, forming n-type doping. Therefore, the doping concentration and polarity can be tuned by biasing voltage. Liu *et al.* [88] fabricated a semi-floating gate transistor (MoS_2/hBN/HfS_2) and a WSe_2/MoS_2 was used as the p–n-junction switch, which demonstrated both tunable charge persistency and ultra-fast writing operation speed (10^6 times that of general memories based on 2D materials) [Fig. 5(a)]. The maximum carrier concentration is limited by dielectric breakdown or an insufficient spatial resolution during conventional electrostatic gating. To solve the problem, an electron beam irradiation approach can be used to tailor the carriers with a nanoscale spatial resolution [89]. Figure 5(b) illustrates the electron-beam-induced doping effect of monolayer MoS_2, which was initially electron-doped with threshold voltage $V_{TH} = -33$ V, and after a 1 keV electron-beam exposure, the threshold voltage shifted to 0 V [Figs. 5(c, d)] with a high mobility of

~130 $cm^2 \cdot V^{-1} \cdot s^{-1}$ at room temperature.

In floating gate modulation, the charge distribution and energy consumption are often inhomogeneous with an indispensable external electric field. However, due to the different local polarization of ferroelectric materials, carrier concentration in the semiconductor channel can be accumulated or deleted to achieve non-volatile doping. Chen *et al.* [90] fabricated a non-volatile WSe_2 p–n homojunction on a ferroelectric $BiFeO_3$ (BFO) substrate utilizing a locally-reversed ferroelectric polarization [Fig. 5(e)]. Through CVD growth and wet transfer method, monolayer crystalline WSe_2 sheets were deposited firmly to a BFO surface, forming a vdW interface which played a key role in the formation of the WSe_2 homojunctions. Through scanning with a metal probe to obtain a ferroelectric domain pattern, the polarization of ferroelectric polymers deposited on 2D TMDs can be controlled, achieving p-type and n-type doping. As presented in Fig. 5(f), the ferroelectric copolymers are alternately polarized up (P_{up} state) and down (P_{down} state), providing a lateral p–n–p–n junction in $MoTe_2$ [91]. The design of naked ferroelectric copolymers, rather than a ferroelectric substrate with unalterable polarization, allows the reprograming and refreshing of projected p–n homojunctions by rewriting the polarization configuration using the probe technique. The p–n homojunctions and corresponding rectification properties can be easily reversed, erased as well as rewritten, exhibiting a spectacular potential for their application in 2D functional optoelectronic and electronic devices.

Apart from substitutional and electrostatic doping, photodoping has been already realized in graphene/h-BN [92] and WSe_2/h-BN [93] heterostructures, which offers a convenient way to in situ and non-destructively modulate the carrier density of 2D TMDs using UV light with high photon energy. As presented in Fig. 5(g), the WSe_2/h-BN FET is illuminated by a light pulse (duration 0.5 s, wavelength 405 nm, intensity 210 $mW \cdot cm^{-2}$) under negative gate pulses, which results in a remarkable excitation of electrons from the mid-gap donor-like state of h-BN to its conduction band. The photon-excited electrons in BN conduction band are transferred to WSe_2 driven by the electric field, leaving the positive charges localized in the middle of the BN bandgap, which can be stored in BN even after removing the negative gate and switching off the light, thus proving an effective local gate and generating a non-volatile electron-storage effect in WSe_2. Photodoping [94] is implemented to generate and manipulate electron spins in magnetic semiconductor as well. Hot electrons, which are excited by absorbing a certain amount of energy from photons or external fields, play a significant role in semiconductor luminescence effect. Hot electrons in bulk semiconductors usually relax via electron-phonon scattering on a sub-picosecond timescale. Quantum-confined semiconductors such as quantum dots offer a unique platform to prolong hot electron lifetime through their size-tunable electronic structure. Wang *et al.* [95] studied hot electron relaxation in photochemically n-doped colloidal CdSe quantum dots and observed 300-picosecond-long hot electrons as a manifestation of the phonon bottleneck effect. For now, studies on photodoping are limited to few metal oxides so far, and the loss of photoexcited holes during photodoping process should be overcome to ensure device efficiency and stability in the future.

The strategy of introducing strains to 2D TMDs can be classified into lattice induction, local deformation, macroscopic regulation and so on. Lattice induction demonstrates that the microenvironment is affected by strains and that doping atoms can be introduced to 2D TMDs through atomic vacancies. Li *et al.* [96] studied strain-driven Se atom substitution doping in monolayer MoS_2. As presented in Fig. 5(h), the initial substitution process occurs at the periphery of a MoS_2 nanosheet due to lower adsorption energy and substitution barrier, which results in expanded MoS_2 lattices, and a tensile strain is produced to the edges and corners of the nanosheet. As a result of the strain field, a long-range size gradient is formed for the lattice constant of MoS_2, which means that the further out the position of a nanosheet is the larger the size of the lattices will be. In other words, the long-range strain fields are responsible for the self-promoted doping process of MoS_2 nanosheets.

To sum up, we provide a comprehensive summary of the strategies and related applications of the doping engineering and the functionalization of 2D TMDs. Different from traditional semiconductors like silicon, direct substitutional doping in the growth process can be slightly difficult due to their atomically thin nature and dangling-bond free interfaces. When the doping concentration rises to a level, the strain effect should be considered. At the same time, increase in the instability of the interface states results in the degradation of carrier mobility and influences the characteristics of devices. Therefore, more attention should be paid on more advanced doping techniques and device demonstrations with a high reliability and process repeatability in the future.

2.4 Alloying

The alloying of different 2D TMDs has emerged as an effective method to tune the physico-chemical properties because of the good thermodynamic stability, precise phase engineering via compositional control and possibility to achieve large-scale devices. In 2D alloyed TMDs, one of the elements in the TMDs is partially substituted by another element, with emerging more complex crystal structures such as crystal grain and crystal boundary [270–272]. Compared with that in doping engineering, the number of substitutions in alloyed TMDs can be of an arbitrary percentage. Generally speaking, isoelectronic

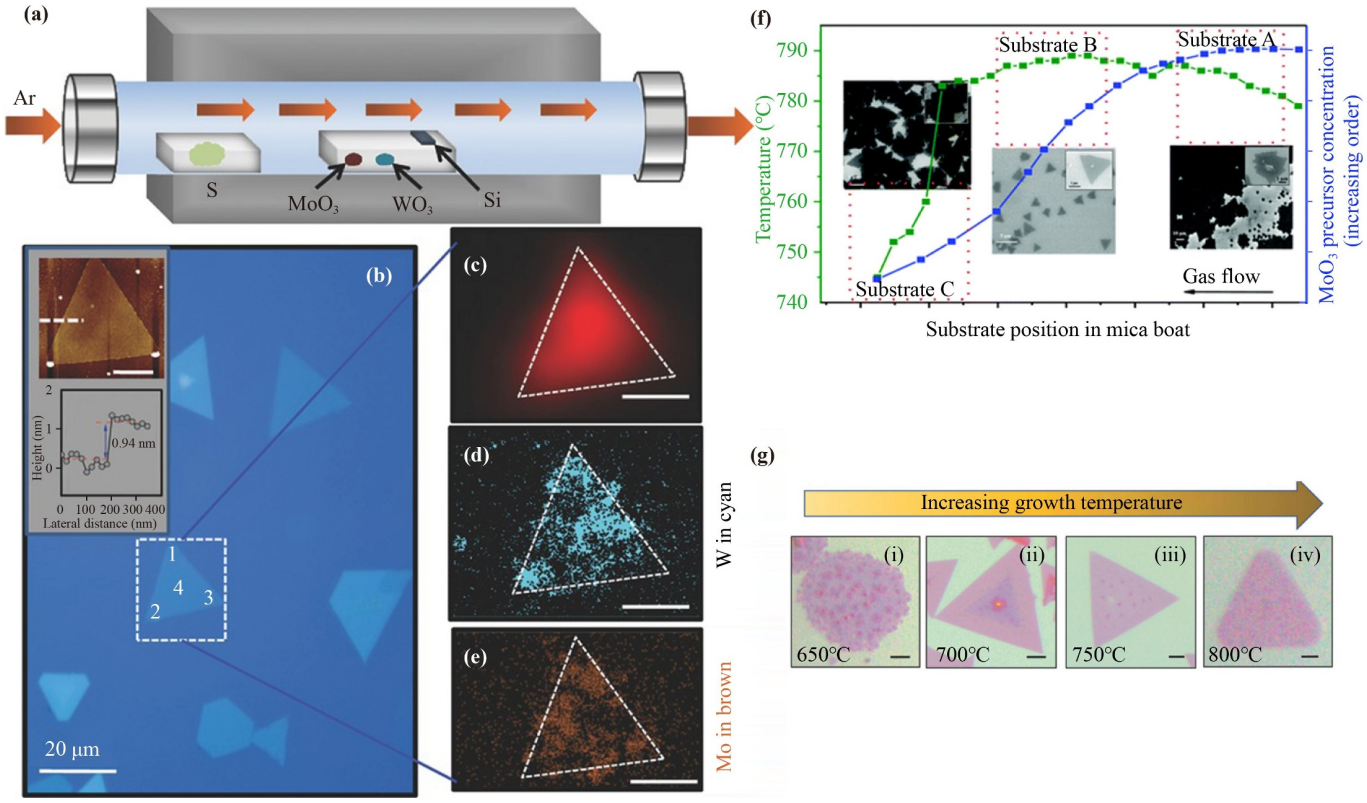

Fig. 6 Alloy engineering of 2D TMDs. **(a)** Illustration of experimental setup of CVD for $W_xMo_{1-x}S_2$ flake. **(b)** Optical image of triangular $W_xMo_{1-x}S_2$ flake (size ≈ 20 μm). The thickness of the as-grown $W_xMo_{1-x}S_2$ was measured by AFM to be ≈ 0.94 nm. **(c)** Raman intensity mapping at a frequency of ≈ 408 cm^{-1} (out-of-plane A_{1g} mode) for the flake. (d, e) EDX mapping of **(d)** W and **(e)** Mo elements. The scale bar in (c–e) is 10 μm. **(f)** SEM images of $MoSe_{2x}S_{2(1-x)}$ alloys grown at the same time but at different temperatures and MoO_3 precursor concentrations on substrates at different locations. **(g)** Optical images of monolayer quaternary alloys $Mo_xW_{1-x}S_{2y}Se_{2(1-y)}$ grown at (i) 650 °C, (ii) 700 °C, (iii) 750 °C, and (iv) 800 °C. Scale bars: (i–iii) 5 μm, (iv) 2 μm. (a–e) Reproduced from Ref. [97]. Copyright © 2017, Wiley-VCH. (f) Reproduced from Ref. [15]. Copyright © 2016, The Royal Society of Chemistry. (g) Reproduced from Ref. [105]. Copyright © 2017, Wiley-VCH.

alloys of 2D TMDs can be divided into three types according to the alloying sites: (1) $M_xM'_{1-x}X_2$ type (transition metal site), (2) $MX_{2x}X'_{2(1-x)}$ type (chalcogen-site), and (3) quaternary alloy $M_xM'_{1-x}X_{2y}X'_{2(1-y)}$ type (both transition metal and chalcogen-site).

2.4.1 $M_xM'_{1-x}X_2$ type

Since most 2D TMDs have the same crystal structure and similar lattice parameters, it's easy to demonstrate homogeneous alloys by partially substituting one of the transition metal elements with another one. Liu *et al.* [97] first demonstrated a triangle-shape monolayer $W_xMo_{1-x}S_2$-based field effect transistor through CVD method under an atmospheric pressure. The monolayer $W_xMo_{1-x}S_2$ was obtained through sulfuration of the mixture of MoO_3 and WO_3 powder in a CVD furnace under an atmospheric pressure at 850 °C for 10 minutes [Fig. 6(a)]. Figure 6(b) shows the optical image of a triangular $W_xMo_{1-x}S_2$ flake (size ≈ 20 μm) whose thickness was measured to be ≈ 0.94 nm using AFM, indicating the monolayer nature of the resultant triangular domain. As is presented in Figs. 6(c–e), the distribution of both Mo and W elements (element ratio W:Mo ≈ 2:1) was not uniform across the monolayer flake. The mobility of $W_xMo_{1-x}S_2$ FETs at 20 K was ≈ 54 $cm^2 \cdot V^{-1} \cdot s^{-1}$, reaching ≈ 30 $cm^2 \cdot V^{-1} \cdot s^{-1}$ at 300 K with a charge density of 5.05 × 10^{12} cm^{-2} . Similarity, Zhou *et al.* [98] demonstrated $Co_xMo_{1-x}S_2$ nanosheets with a Co concentration of 0.8%, 1.7%, and 2.5% through CVD method using MoO_3 and $CoCl_2$ as reaction metal precursors with sulfur powder as the chalcogen precursor.

2.4.2 $MX_{2x}X'_{2(1-x)}$ type

Besides $M_xM'_{1-x}X_2$ type alloys, $MX_{2x}X'_{2(1-x)}$-type alloyed nanosheets have also been prepared through CVD method. Particularly, most of the nanosheets synthesized via CVD method appears to form a triangular shape due to the energetically preferred edge, which merge into a

film by adjusting the synthesis parameters [99, 100]. For example, Umrao *et al.* [15] prepared large-area monolayer $MoSe_{2x}S_{2(1-x)}$ alloys with a controlled morphology using a low-pressure CVD method. By controlling the gaseous MoO_3 precursor on substrates placed in regions at different temperatures, the $MoSe_{2x}S_{2(1-x)}$ nanosheets with different morphologies could be observed [Fig. 6(f)]. The morphology of the alloys related to MoO_3 precursor concentration and temperature confirms that corresponding interface energy plays an effective role in nucleation and growth. Similar fabrication processes were also adopted to prepare $WS_{2x}Se_{2(1-x)}$ nanosheets by controlling the heating temperature of WSe_2 and WS_2 precursor [101]. As is known, most of the 1T- and 1T′-phase TMDs are (semi-) metallic, showing superior performance in (opto)electronics, energy storage, superconductivity and catalysis compared with 2H TMDs. However, only a very few thermodynamically stable 1T′-phase TMD alloys have been reported. Lai *et al.* [102] reported a facile and general synthetic method for preparing 1T′-phase group VIB TMD crystals including $WS_{2x}Se_{2(1-x)}$ and $MoS_{2x}Se_{2(1-x)}$. In addition to the aforementioned Mo/W-based alloys, other $MX_{2x}X'_{2(1-x)}$-type alloys with a tunable phase have also been demonstrated. Wen *et al.* [103] synthesized high-quality $ReS_{2(1-x)}Se_{2x}$ alloys with a distorted 1T structure through CVT method. The photoluminescence emission energy of $ReS_{2(1-x)}Se_{2x}$ monolayers (x from 0 to 1 with a step of 0.1) can be continuously tuned, ranging from 1.62 to 1.31 eV. In another example, large-area $HfS_{2(1-x)}Se_{2x}$ alloys with fully tunable chemical compositions and bandgaps were synthesized on sapphire through CVD method [104].

2.4.3 $M_xM'_{1-x}X_{2y}X'_{2(1-y)}$ type

The CVD growth method is also achievable for $M_xM'_{1-x}X_{2y}X'_{2(1-y)}$-type TMD alloys. Susarla *et al.* [105] presented reliable evidence for the formation of thermodynamically stable $Mo_xW_{1-x}S_{2y}Se_{2(1-y)}$ alloys grown via CVD method, whose composition was tunable as a function of the growth temperature [Fig. 6(g)]. The bandgap could be tuned, which varied from 1.61 to 1.85 eV. Later, they demonstrated a phase transition from metastable $Mo_xW_{1-x}S_{2y}Se_{2(1-y)}$ alloys to stable heterostructures via thermal annealing of the quaternary alloys [106]. The composition-dependent transformation was caused by the existence of miscibility gaps in the quaternary alloys. Furthermore, a reverse-flow CVD strategy was developed to synthesize the quaternary bilayer alloy $Mo_xW_{1-x}S_{2y}Se_{2(1-y)}$ with high yield, a large size and a high controllability [107]. The customized temperature profiles and reverse gas promoted the formation of the first layer without introducing new nucleation centers, leading to the near-defect-free epitaxial growth of the second layer from existing nucleation centers.

The latest research progress has promoted the preparation, characterization and application of 2D alloyed TMD nanosheets, whose diversity, quality and stability still remain a key challenge for practical application. However, benefited from unique properties with tunable bandgaps and a distinct charge-carrier polarity, 2D alloyed TMD nanosheets will play a vital role in the forthcoming breakthroughs of semiconductor technology nodes after overcoming the aforementioned challenges.

2.5 Vertical and lateral heterostructures

With dangling-bond-free surfaces and weak vdW interlayer interactions among the constituent 2D TMD nanosheets, random combinations of 2D materials can be chosen to manually stack in arbitrary sequences to form hybridized vdW heterostructures, which perform a better potential in electronics, optoelectronics, catalysts, spintronics, and so on. Generally speaking, 2D heterostructures can be in either the vertical or lateral direction or have either vdW or covalent interactions. CVD technique is considered to be an applicable method for the construction of 2D heterostructures with better interface coupling and a comparable higher quality.

2.5.1 Vertical heterostructures

For vertical heterostructures, the interlayer interactions are mainly generated by vdW forces. Because of this, there is no or little requirement for the lattice matching among different layers. The earlier works on CVD-based 2D heterostructures started with graphene and TMDs due to the advantage of both graphene with its high transparency, high conductivity and tunable work function and TMDs with wide band gaps. For example, though the lattice spacing of MoS_2 is ~28% larger than that of graphene, MoS_2 and graphene still match each other well in a vdW gap [108]. With the development of CVD growth and transfer technique, more complicated vertical heterostructures have been reported. Gong *et al.* [22] reported a one-step growth strategy for the creation of vertical and in-plane heterostructures from WS_2/MoS_2 monolayers. As is presented in Fig. 7(a), the vertical and in-plane heterostructures were synthesized through strictly controlling the growth temperature. Furthermore, other kinds of vertical heterostructures generated via one-step CVD method, such as SnS_2/SnS [109], NbS_2/MoS_2 [110], and CdS/MoS_2 [111], have been already reported. However, the interface sharpness of heterostructures may degrade due to the element substitution during CVD growth, and the size of the heterostructures can hardly be controlled. Therefore, the two-step growth process shows great advantages in controlling the interface structures of heterostructures. Ai *et al.* [112] reported the growth of CdI_2/MoS_2 (WS_2, WSe_2) vdW heterostructures using a two-step CVD method. The MoS_2, WS_2 and WSe_2 nanosheets were first

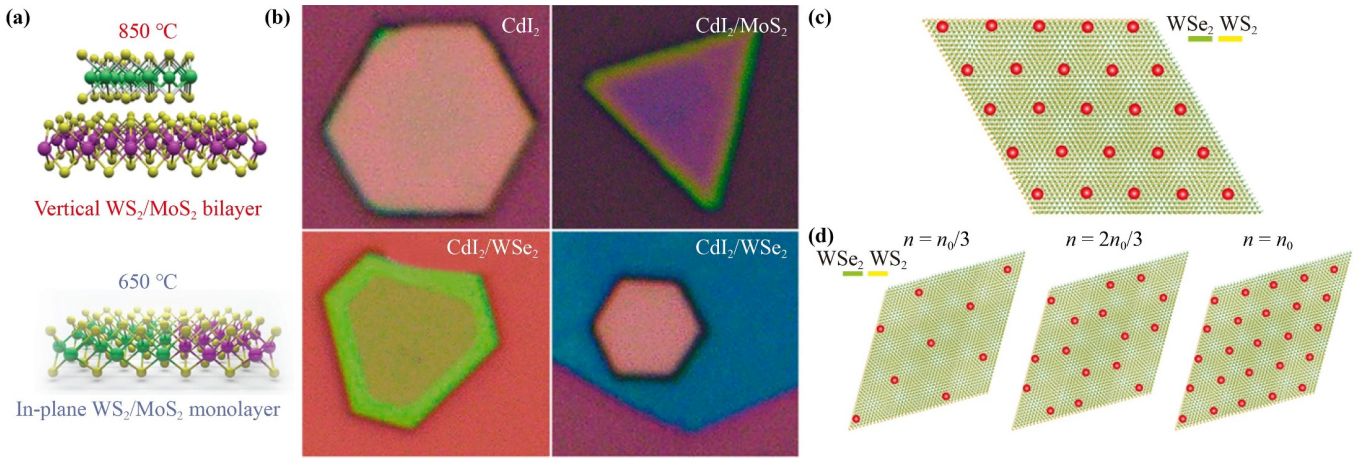

Fig. 7 Vertical heterostructures of 2D TMDs. **(a)** Schematic images of the vertically stacked and in-plane WS_2/MoS_2 heterostructures synthesized at different temperatures. **(b)** Optical microscope images of CdI_2 nanoplates and vertical heterostructures grown on other 2D TMDs (WS_2, WSe_2, MoS_2). **(c)** Illustration of a Mott insulator state in a WSe_2/WS_2 moiré superlattice (green and orange layers) with one hole (red holes) per superlattice unit cell. **(d)** Illustrations of generalized Wigner crystal ($n = n_0/3$, $n = 2n_0/3$) and Mott insulator stated ($n = n_0$) in a WSe_2/WS_2 moiré superlattice. (a) Reproduced from Ref. [22]. Copyright © 2014, Springer Nature. (b) Reproduced from Ref. [112]. Copyright © 2017, American Chemical Society. (c, d) Reproduced from Ref. [118]. Copyright © 2020, Springer Nature.

grown via physical vapor deposition (PVD) method, and then the as-grown MoS_2 (WS_2, WSe_2) nanosheets were used as the substrate for the vdW epitaxial growth of CdI_2 to obtain vertical heterostructures [Fig. 7(b)]. During the second growth step of the vertical heterostructures, it is significant to optimize growth conditions to suppress the formation of laterally stacked heterostructures or alloys.

Recently, the in-plane moiré superlattices formed by lattice mismatch have drawn great attention for their strongly-correlated electrons and hybrid excitons [113, 264–265]. Different from magic-angle twisted-bilayer graphene and ABC rhombohedral-stacked graphene/h-BN moiré superlattices [114–117], TMD moiré heterostructures provide another model system for studies on correlated quantum phenomena because of their strong light-matter interactions and large SOC. Regan *et al.* [118] reported an experimental optical detection of strongly-correlated phases in semiconducting WSe_2/WS_2 moiré superlattices. As illustrated in Fig. 7(c), the Mott insulating state exists in WSe_2/WS_2 moiré superlattices with one hole (red circles) per superlattice unit cell. The excited-state and non-equilibrium dynamics of the correlated phases are confined in the triangular lattice. Meanwhile, W, a heavy transition metal element, imposes substantial SOC onto low-energy degrees of freedom, which can induce topological properties in turn. As illustrated in Fig. 7(d), with the increase of the hole doping level of $n = n_0/3$, $n = 2n_0/3$ and $n = n_0$, the insulating states of WSe_2/WS_2 moiré superlattices exhibit a unique interaction-driven Wigner crystal state or a charge-transfer insulator, which are completely absent in large-twist-angle WSe_2/WS_2 heterostructures. In addition, correlated quantum spin Hall insulators [119], moiré excitons [113, 120] and Hubbard model physics [121, 122] have been reported in moiré vertical heterostructures, yielding an abundant and exciting development.

2.5.2 Lateral heterostructures

For lateral heterostructures, isolated atomic-layer components are seamlessly stitched in a plane to form an atomically sharp interface via strong covalent bonding, which leads to strict lattice matching. Therefore, atomically thin lateral heterostructures can only be fabricated through bottom-up approaches like CVD method. In agreement with vertical heterostructures, lateral heterostructures can be synthesized through either one-step or two-step synthetic process. In a direct one-step synthesis process, two or more metal precursors need to be first simultaneously presented in a reaction chamber. Then the material with the higher nucleation rate at a high evaporation temperature tends to deposit at the core of the heterostructures. Finally, the second material grows along the edge of the core material, forming lateral heterostructures. For instance, Zhang *et al.* [123] achieved a direct synthesis of the lateral heterostructures of monolayer MoS_2/WS_2 and $MoSe_2/WSe_2$ using APCVD with aromatic molecules as seeding promoters. The schematic illustration of the experimental setup and detailed parameters are shown in Fig. 8(a). In the high-temperature zone, the WO_3 powders were filled in a homemade quartz reactor with a transfer tube in tunable length at a high evaporation temperature to enable a stable vapor flow of the WO_{3-x}, which was the reactant evaporated from the high-temperature zone to react with S or Se on substrate surfaces at each specific

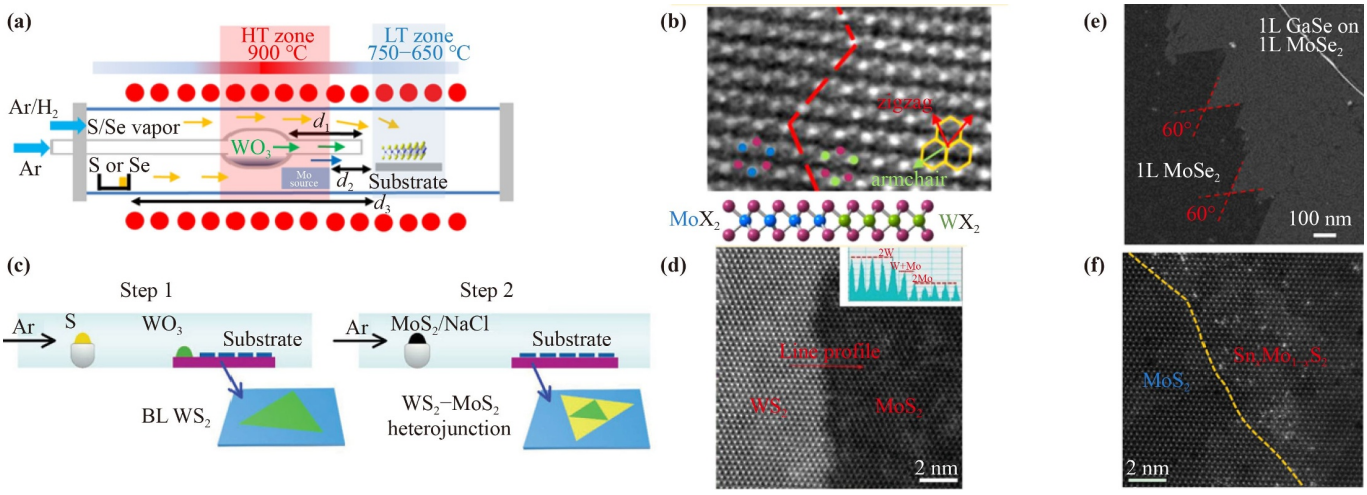

Fig. 8 Lateral heterostructures of 2D TMDs. **(a)** Schematic illustration of experimental one-step APCVD setup of lateral heterostructure of MoX_2/WX_2 (X = S, Se). **(b)** High resolution STEM HAADF image of hetero-interface of the MoX_2/WX_2 lateral heterostructure (X = S, Se). **(c)** Schematic illustration of experimental two-step CVD setup of lateral heterostructure of WS_2/MoS_2 heterostructures. **(d)** Atomic scale HADDF image of the interface in the triangular bilayer WS_2/MoS_2 heterostructure. The inset shows the intensity profile along the arrow line crossing the interface. **(e)** Low-magnification ADF-STEM image showing the edge area of the monolayer $GaSe/MoSe_2$ lateral heterostructures. **(f)** Atomic resolution STEM image taken from the epitaxial $Sn_xMo_{1-x}S_2/MoS_2$ heterostructure at the interface. (a, b) Reproduced from Ref. [123]. Copyright © 2015, American Chemical Society. (c, d) Reproduced from Ref. [128]. Copyright © 2019, Wiley-VCH. (e) Reproduced from Ref. [133]. Copyright © 2016, The American Association for the Advancement of Science. (f) Reproduced from Ref. [126]. Copyright © 2020, Wiley-VCH.

temperature and distance. The growth of W-based monolayers was initiated from the edges of as-grown Mo-based monolayers, which followed the domain shape for the following lateral growth. As labeled in Fig. 8(b), the 1D heterointerfaces prefer to be aligned in the zigzag direction due to the broken inversion symmetry of bilayer TMDs. Other lateral heterostructures, including 1H-MoS_2/1T′-$MoTe_2$ [124], WS_2/WSe_2 [125], $Sn_xMo_{1-x}S_2$ /MoS_2 [126] and 2H/1T′-$MoTe_2$ [127], have also been prepared. Compared with that of vertical heterostructures, for the two-step of growth of lateral heterostructures, the parameters also need to be strictly controlled during the formation of lateral junctions. Ye *et al.* [128] synthesized large-scale lateral bilayer WS_2/MoS_2 heterostructures through a two-step CVD route. As indicated in Fig. 8(c), the WS_2 bilayer crystals are first prepared on a Si/SiO_2 substrate with WO_3 and sulfur powders as precursors. Then by heating the precursor of mixed MoS_2 and NaCl, the MoS_2 is grown along the edge of the WS_2 bilayer crystals to form lateral heterostructures. According to existent findings, the carrier gas [129], growth temperature [130, 131] and the thickness of the first core nanosheet [132] can influence the composition of the lateral heterostructures. It is worth mentioning that there is usually an atomically sharp connection among the lateral heterostructures obtained from the two-step synthesis method at the boundary regions [Fig. 8(d)], which is different from those alloy-like structures through the one-step synthesis method. Similar sharp edges can be also found in $GaSe/MoSe_2$ [133] and $Sn_xMo_{1-x}S_2/MoS_2$ [134] heterostructures [Figs. 8(e, f)]. Controlling the interface morphology of lateral heterostructures has drawn enormous attention since it provides a good way to tune the photoexcited carrier transport property of optoelectronic devices meanwhile rendering devices with novel functions [135, 136]. The differences in relative formation energy contribute to the band alignment in the lateral heterostructures [137].

In summary, we briefly introduced controllable CVD growth methods for demonstrating vertical and lateral heterostructures with either vdW or covalent interactions. Vertical heterostructures represent strong correlated quantum phenomena in the in-plane moiré superlattices, boosting a better electrochemical activity especially for energy storage and conversions; while lateral heterostructures possess a better stability, presenting excellent current rectification behavior and photocurrent generation characteristics. Therefore, fabricating high-quality 2D TMD heterostructures with a controllable morphology based on CVD growth method will be instructive in further works.

3 Applications based on 2D TMDs

Establishing high-end 2D TMDs may lead to intriguing properties, particularly in the application of electronic, optoelectronic, ferromagnetic, ferroelectric, spintronic

and valleytronic devices. In this section, we will focus on the recent developments in the application of above-mentioned areas.

3.1 Electronics

3.1.1 Field-effect transistors

Field-effect transistors (FETs) are the most fundamental and important building blocks in electronics. According to the well-known Moore's law, the number of transistors in an integrated circuit (IC) doubles roughly every 18 months, which requires smaller transistors and higher integration levels. Unfortunately, as silicon-based transistors enter the sub-10 nm technology nodes, two main technical problems become noteworthy obstacles. One is short channel effect, which results in a weak tunability of channel current flow when the channel length drops below 10 nm. In particular, carrier mobility theoretically scales with the sixth power of the thickness of the semiconductor body due to thickness-fluctuation-induced scattering when the body thickness is below 5 nm, causing a critical limit to the continued transistor scaling [138]. Another obstacle is the heat dissipation. Hot electrons containing enough energy to overcome the potential barriers between Si and SiO_2 will partly fall into the electron traps of SiO_2 and accumulate over time. The accumulated heat may result in the downgrade of carrier mobility and the reduction of device life. In addition, future electronic devices are required to be more flexible, with a lower power consumption and higher performance as well as be more multifunctional. 2D TMDs feature an excellent mechanical flexibility and dangling-bond-free surfaces, which exhibit a superior carrier mobility and on/off ratio in TMD-based FETs. In the following paragraphs, we highlight recent research progresses in TMD-based FETs via CVD growth method and discuss on current challenges as well as potential opportunities.

Recently, the theoretical studies based on density functional perturbation theory and Wannier interpolation of the electron-phonon matrix show that for most MX_2, a high carrier mobility is desirable for high-quality FETs. while for MoS_2 and WS_2, the carrier mobility is limited by the extrinsic longitudinal acoustic phonon scattering rather than its intrinsic band structure [139]. Yu *et al.* [24] fabricated highly-uniform enhancement-mode FETs with a relatively high mobility (80 $cm^2 \cdot V^{-1} \cdot s^{-1}$ at room-temperature) and a low subthreshold swing using CVD-grown MoS_2. Similarly, p-type Nb-doped WSe_2 [140] was used as the active layer of the FETs, yielding a maximum field effect mobility of 116 $cm^2 \cdot V^{-1} \cdot s^{-1}$ with an on/off ratio of 10^6. The off current of the doped device is higher than that of the intrinsic device, indicating the increased screening of Coulomb scattering centers as a result of a higher carrier concentration. Recently, other emerging 2D semiconductors like $PtSe_2$ [141], $PdSe_2$ [142], Bi_2O_2Se [143] and InSe [144] exhibit strong interlayer coupling and a much higher carrier mobility than conventional TMDs. For example, the theoretically calculated carrier mobility of h-BN/γ-InSe/h-BN van der Waals heterostructures can reach 4340 $cm^2 \cdot V^{-1} \cdot s^{-1}$ at room temperature, which could easily go over 10^4 $cm^2 \cdot V^{-1} \cdot s^{-1}$ at low temperatures. However, the lack of high-quality of 2D crystals grown through CVD approach limits the research on their exotic properties and practical application. Experimentally, Gu *et al.* [142] fabricated few-layer CVD-grown $PdSe_2$ FETs, revealing a tunable ambipolar charge carrier conduction with an electron mobility up to ≈ 294 $cm^2 \cdot V^{-1} \cdot s^{-1}$. As presented in Fig. 9(a), the device is fabricated with 8 electrodes and the transistor channels are along the edges as well as diagonals of the square flake. The field-effect mobility is extracted from the linear region of the transfer curve in each direction, which is plotted in Fig. 9(b), exhibiting strong in-plane anisotropic optical properties.

Short gate lengths become another research hotspot in the studies on FETs based on 2D TMDs channels, especially those down to the sub-10 nm region while avoiding the degradation of device performance. MoS_2 is first used to fabricate FETs with a sub-10 nm gate or channel length [1, 145–149] for its dangling-free smooth surface and atomic thickness. Desai et al. demonstrated MoS_2 transistors with a gate length of 1 nm, in which a single-walled carbon nanotube (SWCNT) served as the gate electrode. The device structure [Fig. 9(c)] consisted of a MoS_2 channel, a ZrO_2 gate dielectric, and a SWCNT gate grown via CVD on a 50 nm SiO_2/Si substrate with a gate length of ~1 nm. The transistors showed excellent switching characteristics with an extremely low subthreshold swing of ~65 mV/dec and a large on/off current ratio of ~10^6, indicating an ideal suppression of short channel effect. It is very hard to further scale down gate lengths below 1 nm. Very recently, side-wall MoS_2 transistors with an atomically thin channel and a physical gate length of sub-1 nm were demonstrated using the edge of a graphene layer as the gate electrode [149]. The effective channel length approached 0.34 nm in ON state and 4.54 nm in OFF state. As shown in Fig. 9(d), the CVD monolayer graphene is transferred to the substrate and an Al screening layer is deposited on the graphene after the EBL process. The final device has five electrical terminals, namely the source, drain, an Al screening layer, a 0.34 nm graphene edge gate and the fixed back-gated Si. By applying a negative voltage to the edge to locally deplete the vertical MoS_2 channel, the transistor can be completely turned off. The devices showed an ON/OFF ratio of up to 1.02 × 10^5 and a subthreshold swing value down to 117 mV/dec [Fig. 9(e)]. The side-wall structure provides a new thought for scaling down transistors to approach the physical limit. Besides MoS_2, Schottky barrier FETs based on in-plane phase transition TMDs have shown great electric perfor-

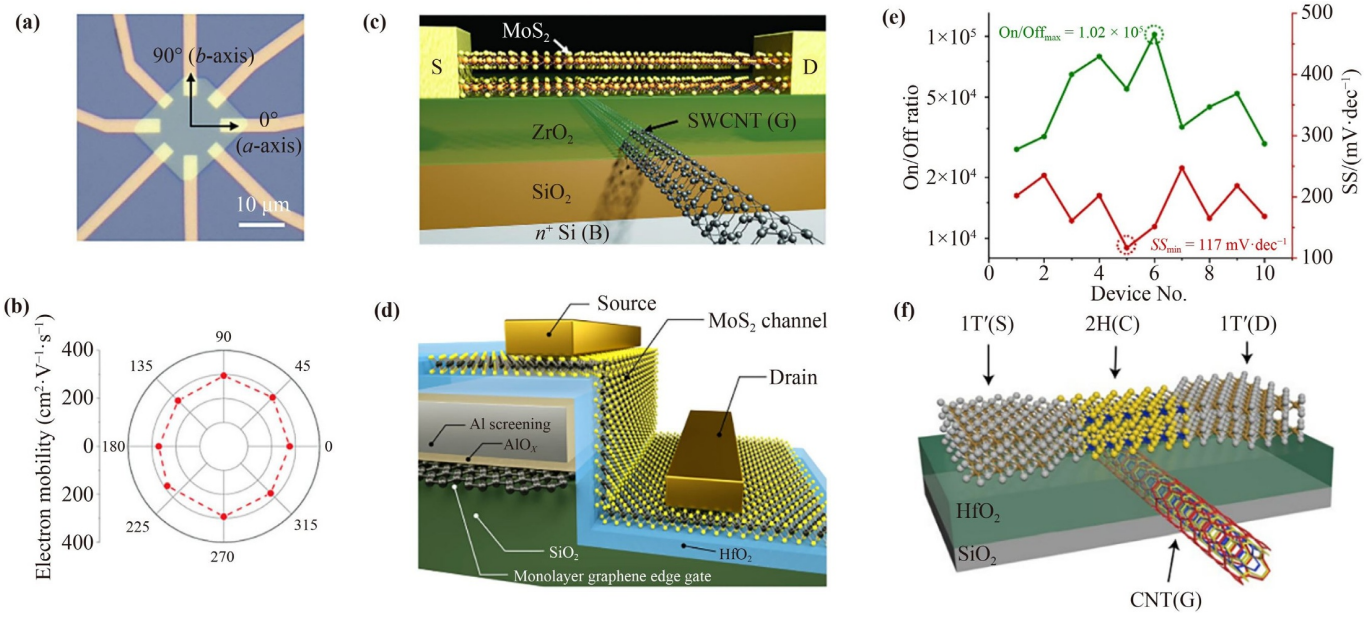

Fig. 9 2D TMDs for field-effect transistors. **(a)** Optical image of a 9 nm CVD $PdSe_2$ device with 8 electrodes. **(b)** Electron mobility of the device in (a) along 8 directions evenly spaced plotted in polar coordinates after the third annealing at 450 K. **(c)** Schematic of 1D2D-FET with a MoS_2 channel and SWCNT gate. **(d)** Schematic of side-wall gate structure with a monolayer MoS_2 channel and 0.34 nm monolayer graphene edge gate. **(e)** The maximum On/Off ratio and minimum SS value extracted from the 10 typical devices. **(f)** Schematic of a chemically synthesized 1T′/2H-$MoTe_2$ FET with a CNT gate. (a, b) Reproduced from Ref. [142]. Copyright © 2020, Wiley-VCH. (c) Reproduced from Ref. [1]. Copyright © 2016, The American Association for the Advancement of Science. (d, e) Reproduced from Ref. [149]. Copyright © 2022, Springer Nature. (f) Reproduced from Ref. [151]. Copyright © 2019, Springer Nature.

mance, such as $MoSe_2$ [150], $MoTe_2$ [151, 262], WSe_2 [150] and WTe_2 [152]. For instance, Zhang *et al.* [151] constructed high-performance FETs with ultrashort gate lengths (4 nm) using CVD-grown $MoTe_2$ as the active material by tuning its structure to the 2H or 1T′ phase. As shown in Fig. 9(f), the FETs are fabricated based on the phase engineering of 2H-1T′ interface using 2H-$MoTe_2$ as the channel, 1T′-$MoTe_2$ as the electrode and a 4-nm-diameter-CNT as the gate. The 4-nm-gate FETs exhibit a low subthreshold swing of ~73 mV/dec and a high ON/OFF current ratio of ~10^5.

Overall, despite tremendous progress available in high-end 2D TMD FETs, there are still many challenges from concept genesis to industrial maturity like immature growth technologies, instability, relatively low on-state current densities and low integration into circuits. Fortunately, there seems to be no fundamental blockade to the wafer-scale processing of 2D TMD FETs or a large-scale integration at a circuit level. With the development of related theories and technologies, we believe that fabrication of high-quality FETs based on 2D TMDs would soon be ready for mainstream applications and bring measurable benefits to our life.

3.1.2 Electronic memory devices

With an atomic thickness and tunable bandgaps, 2D TMDs exhibit great flexibility when fabricating memories with a low power consumption and high performance. Generally, electronic memory devices can be divided into volatile-memory and nonvolatile-memory devices according to the characteristics of their storage medium. Volatile memory technologies include static/dynamic random-access memory (SRAM/DRAM), which features fast operation and is widely applied in internal memories. However, volatile memories need to be written and read repeatedly due to the discharge characteristics of capacitors, leading to a low integration and a high power consumption. Compared with volatile memory technologies, nonvolatile memories can save data without continuous power supply. Currently, mainstream nonvolatile memories include flash memory, electrically erasable programmable read-only memory (EEPROM), phase change memory (PCM), resistive random-access memory (RRAM), ferroelectric random-access memory (FeRAM) and magneto resistive random-access memory (MRAM). Here in, we present the recent progress of electronic memory devices based on 2D TMDs.

For volatile memory technologies, SRAM is the dominant on-chip cache for its short access time and static characteristic. A typical SRAM cell comprises six MOSFETs including two pull-up PMOSFETs (P1, P2), two pull-down (N1, N2) and two access NMOSFETs (A1, A2). Thanks to both n-type and p-type in 2D

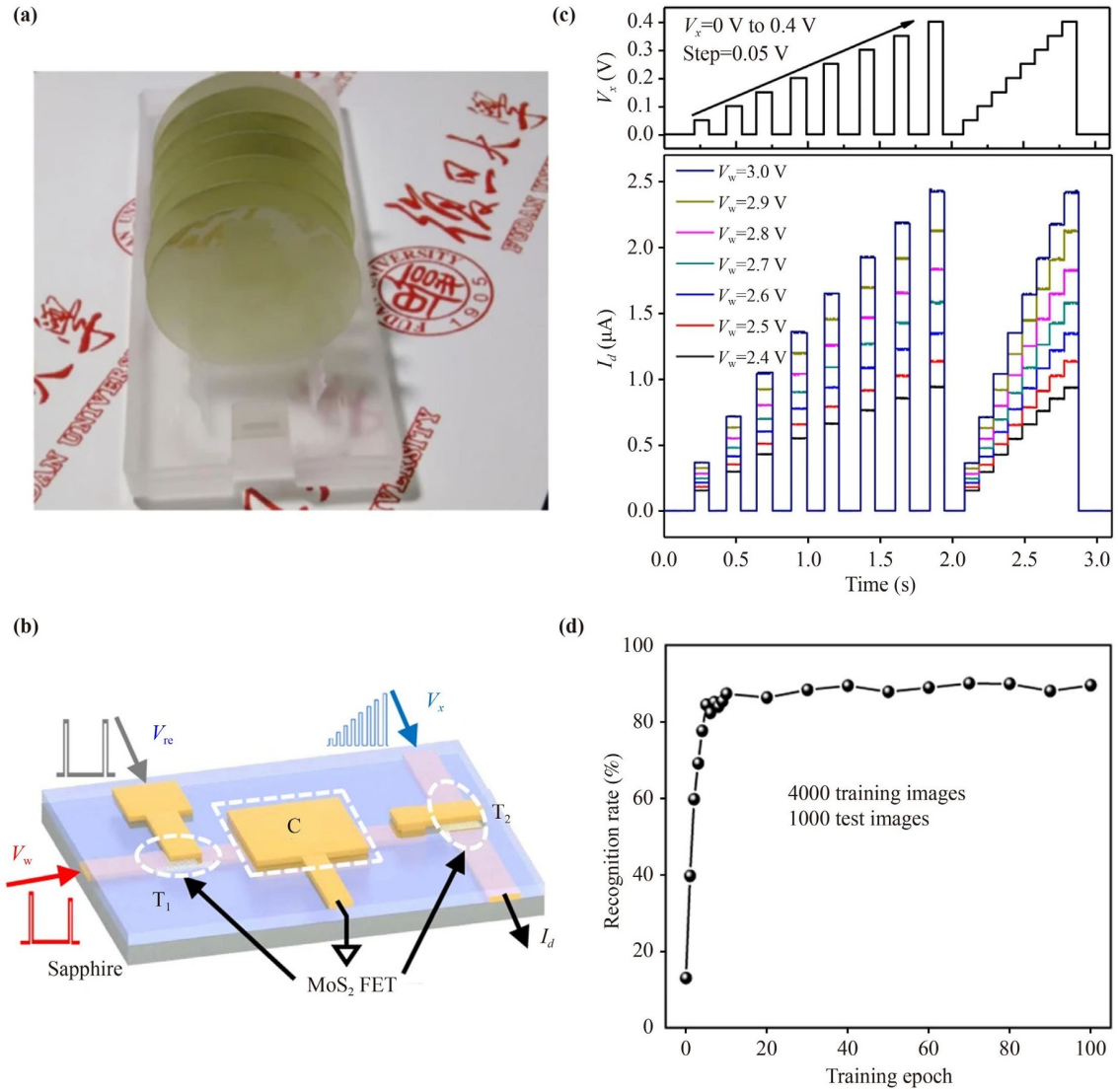

Fig. 10 2D TMDs for volatile electronic memory devices. **(a)** Wafer-scale MoS_2 continuous films are batch-synthesized by a CVD method. **(b)** 3D schematic illustration of a 2T-1C cell containing two MoS_2 FETs and one capacitor. **(c)** Demonstration of multi-step V_x (top) and I_d (bottom) operation using two 2T-1C cells. **(d)** Recognition rate in fully connected neural network simulation as a function of training epoch (0–100), using 4000 images for training and 1000 images for testing. (a–d) Reproduced from Ref. [159]. Copyright © 2021, Springer Nature.

TMDs [153], reliable SRAM arrays have been realized based on 2D TMDs with MoS_2 and WSe_2 chosen as the n-channel and p-channel for the CMOS units. For instance, Hu *et al.* [154] demonstrated a multi-tier monolithic 3D SRAM based on back-gated 2D MoS_2 FETs to release the impact of metal line resistance. Compared with the design of the one-tier back-gated (BG) SRAM cell, the monolithic three-tier BG SRAM cell shows a reduction of 44.3% in cell area, together with an improvement of 28.4% in read access time, 21.3% in dynamic energy and 43.6% in energy-delay product. Furthermore, higher improvement is achieved in read access time and energy-delay products by adjusting the number of stacked MoS_2 nanosheet FETs [155]. Pang *et al.* [156] demonstrated a CMOS SRAM using WSe_2 MOSFETs with p-FETs being chemically doped and n-FETs being electrostatically doped for the first time. An O_2-plasma treatment is performed to form a WO_{3-x} layer on the top of the exposed WSe_2 portion, which serves as a strong p-type dopant due to its high electron affinity. After a plasma treatment, the device displays p-type unipolar characteristics with an improved ON-state, an *SS* of 90 mV/dec and a small hysteresis of 30 mV. Compared with traditional a-IGZO or organic technologies, the WSe_2-based SRAM shows a shorter read/write time and a lower power consumption.

Despite the tremendous progress in 2D TMD-based SRAM, the high cost and low integration limit the

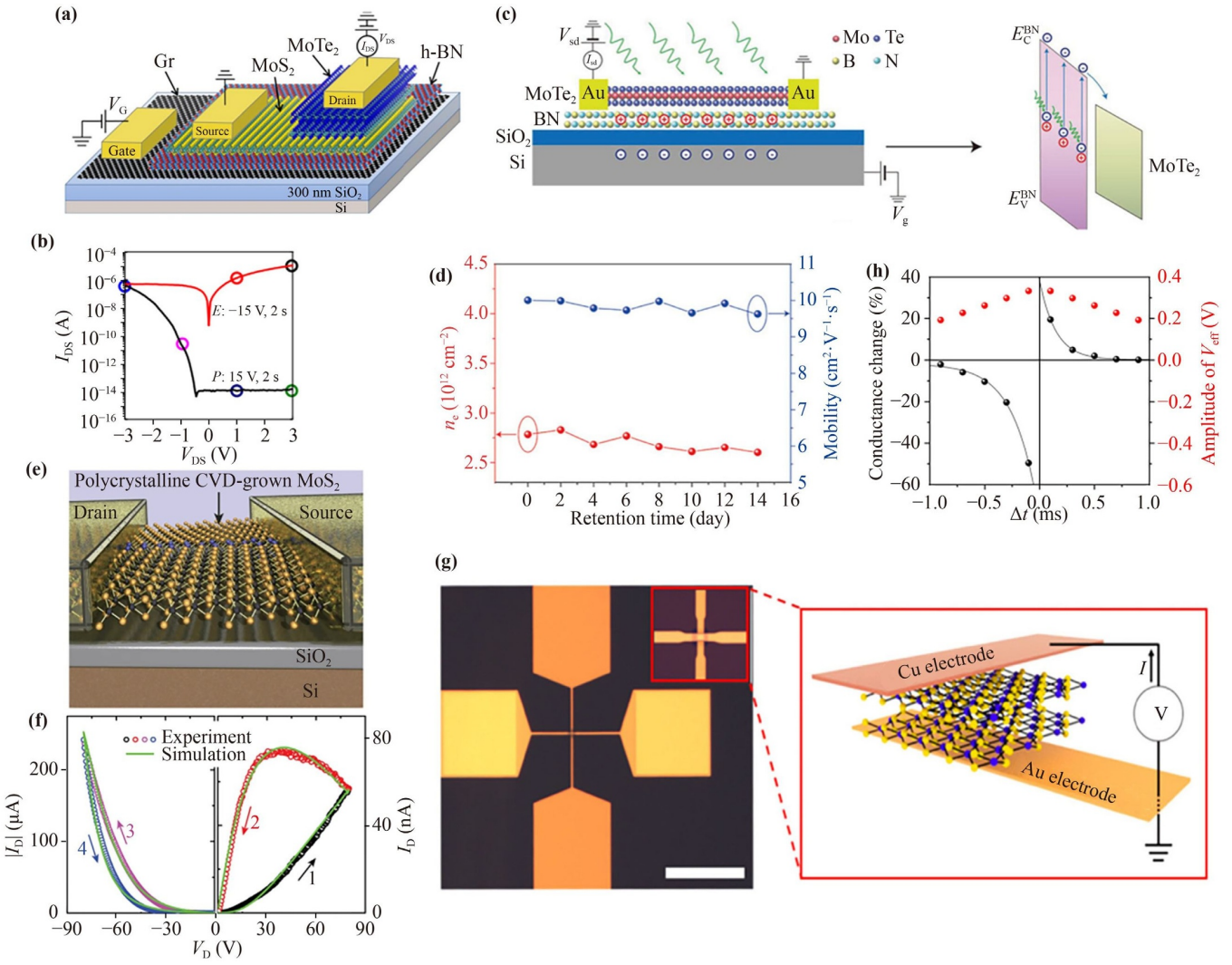

Fig. 11 2D TMDs for nonvolatile electronic memory devices. **(a)** Schematic structure of the device with a $MoS_2/MoTe_2$ heterojunction as a channel at the top, h-BN as a dielectric layer in the middle, and grapheme (Gr) as a gate electrode at the bottom. The source electrode (the contact connected to MoS_2) is grounded. **(b)** The program (P, black curve) and erase (E, red) states of the device after applying a ±15 V back-gate pulse with 2 s duration. **(c)** Schematic of the device structure and corresponding energy band diagram of the $MoTe_2$/BN heterostructure under photodoping. The red and blue circles represent the positive charges and electrons. E_C^{BN} and E_V^{BN} represent the minimum energy of conduction band and the maximum energy of valance band of BN. **(d)** Plot of electron concentration and mobility with respect to the retention time. **(e)** Schematic of a MoS_2 memtransistor device built on 300-nm-thick thermal SiO_2 on doped Si (gate). **(f)** I_D–V_D curve of a MoS_2 memtransistor (L = 5 μm, W = 100 μm) at gate bias V_G = 10 V. **(g)** Optical image of Cu/MoS_2 double-layer/Au memristor with the scale bar of 100 μm (left) and schematic illustration (right). The memristor's crossbar area is 2 × 2 μm^2. **(h)** Measured conductance change (black) and amplitude of V_{eff} (red) as functions of Δt. (a, b) Reproduced from Ref. [25]. Copyright 2018, Springer Nature. (c, d) Reproduced from Ref. [164]. Copyright © 2018, Wiley-VCH. (e, f) Reproduced from Ref. [167]. Copyright © 2018, Springer Nature. (g, h) Reproduced from Ref. [168]. Copyright © 2019, American Chemical Society.

application of SRAM in wearable electronic devices. Different from SRAM, a DRAM cell only comprises a capacitor and a transistor. The information in DRAM cells is read by sensing the voltage changes in the capacitors [157]. Theoretically, DRAM devices possess an ultra-high programming speed and a superior endurance (>10^{16} [158]). But periodic charging is required due to the short retention time of DRAM devices, leading to a large power dissipation. Recently, Wang *et al.* [159] designed a 2T-1C configuration with a similar memory portion as 1T-1C DRAM based on wafer-scale monolayer MoS_2 via CVD growth [Figs. 10(a, b)]. The 2T-1C unit cell is shown in Fig. 10(b) to provide charge storage and analog computation. The ultralow leakage current of the MoS_2 transistor enables the storage of multi-level voltages on the capacitor with a long retention time [Fig. 10(c)]. What's more, a fully connected neural network simulation based on experimental data indicates an accuracy of 90.3%

for image recognition in the devices [Fig. 10(d)], offering a promising approach for training neural networks. However, the capacitive preparation process limits the read-write time and application in CPU chip manufacturing [160]. To store information with a single transistor at different current levels, a large-scale DRAM integration will be realized with high performance and low power dissipation based on 2D TMDs [161].

Flash memory is the most widely used nonvolatile memory in the field of industrial storage, through which not only information like EEPROM can be erase and program, but data can also be read. According to the storage layer material, flash memory can be divided into floating-gate transistor and charge-trap transistors. Benefited from tunable bandgaps of 2D TMDs, floating-gate transistors based on a TMD channel exhibit high ON/OFF ratios and a low power consumption. Cheng *et al.* [25] fabricated an asymmetric floating-gate transistor with $MoS_2/MoTe_2$ heterostructures serving as channels [Fig. 11(a)]. The charge-carrier injection can be switched between tunneling and thermal activation under both positive and negative bias conditions. As a matter of fact, floating-gate FETs exhibit an ultrahigh rectification ratio exceeding 2×10^7 [displayed as the black curve in Fig. 11(b)]. In addition, to realize a universal logic gate by employing an innovative way based on logic-in-memory, a programmable logic circuit can be demonstrated with MoS_2 as an active channel without applying additional terminals for programming [88, 162]. Different from free moving charges in floating-gate FETs, charges are bound to the defects on the storage layer of charge-trap transistors and are transferred via gate voltages or light. For example, Antonio *et al.* [163] observed hysteresis in the transfer characteristics of back-gated FETs with a MoS_2 channel via water-facilitated charge trapping at a MoS_2/SiO_2 interface. By introducing detective h-BN substrates, the electrons within the mid-gap trap state of h-BN could transfer into semiconductor channels via a negative gate voltage and light pulse. Meanwhile, the positive charges are still bound to the defects of substrates, resulting in current polarization. Based on such a storage mechanism, Liu *et al.* [164] realized the photoinduced nonvolatile and programmable electron doping of multilayer $MoTe_2$/h-BN heterostructures [Fig. 11(c)]. As presented in Fig. 11(d), the electron concentration and mobility retain nearly unchanged for over 14d, illustrating an outstanding nonvolatile property.

RRAMs (also called memristors) record the changes and the amount of flowing charge to store information under applied voltage biases according to their resistance states [165]. With a higher processing speed, a larger storage capacity and a longer durability than flash memory, RRAMs show a great potential of in-memory computing, speech recognition, automatic drive and neuromorphic computing [166], etc. Recently, emerging 2D TMDs provide opportunities for realizing high-performance RRAMs. For instance, Sangwan *et al.* [167] demonstrated multi-terminal hybrid memristors and transistors using polycrystalline CVD-grown MoS_2 through a scalable fabrication process [Fig. 11(e)]. The memtransistors exhibit gate tunability in individual resistance state by 10^4, together with high switching ratios, a high cycling endurance and a long-term retention of states [Fig. 11(f)]. Furthermore, six-terminal MoS_2 memtransistors show gate-tunable heterosynaptic functionality, which is not achievable for two-terminal memristors and neuromorphic computing may be realized by mimicking biological neurons with multiple synapses. Additionally, Xu *et al.* [168] designed a vertical memristor in which a bilayer MoS_2 was sandwiched between a copper top electrode and a silver bottom electrode [Fig. 11(g)]. With consistent bipolar and analogue switching at low-voltage regions, the memristor exhibits the synapse-like learning behavior such as spike-timing dependent plasticity (STDP). As illustrated in Fig. 11(h), the changes in each given Δt on either the positive or negative side can be fit with an exponential decay at low switching voltages of 0.1–0.2 V, providing an opportunity for the application of neuromorphic circuits.

Electronic memory devices have been widely used in modern information technologies, which have changed the way of obtaining and manipulating information. Nowadays, with the geometric growth of data, a high capacity, a fast writing and reading speed, a long retention time, a high scalability and a low power consumption are required for electronic memory devices. 2D TMDs have shown an atomic thickness and tunable bandgaps, which have been demonstrated as one of the most promising archetypes to overcome the limitations of traditional von Neumann architectures. Nonetheless, current work on 2D TMD-based electronic memories is still in its infancy. Low stability, low integration, small scales and difficulties in modulating device electronic properties make the devices far from meeting the practical requirements. It is clear that wafer-scale growth, novel circuit designs, hybrid architectures and compatibility with CMOS circuits will be hot research issues in the future.

3.2 Optoelectronics

3.2.1 Photodetectors

Photodetectors are utilized for light detection by converting optical signals into electrical signals. There are various kinds of operation mechanisms by which optical signals absorbed are transferred into electrical signals via 2D material detectors, such as photoconductive effect, photogating effect, photovoltaic effect, photothermoelectric effect and electromagnetic-wave-induced wells. Under the driving force of the applied biases, free charges transport across the active layers followed by a collection of electrodes, which finally form photocurrent. On the basis of spectral range, the detection wavelength

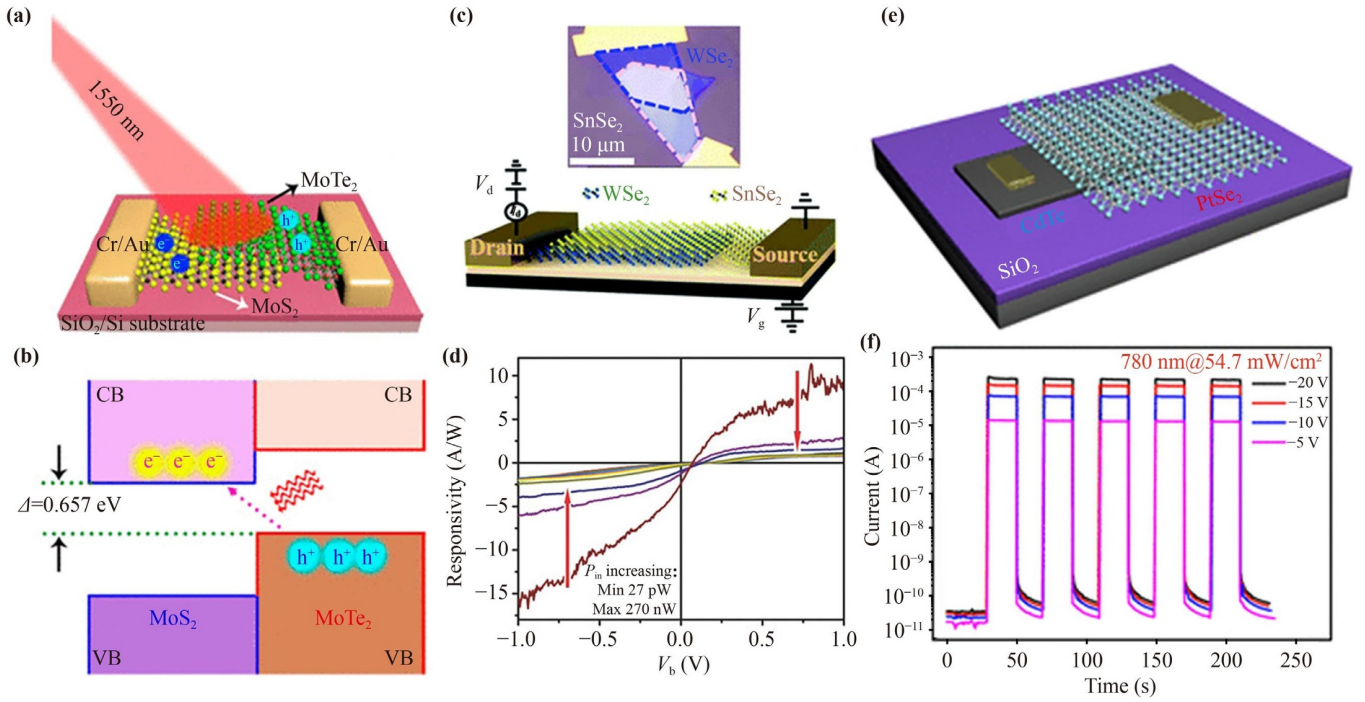

Fig. 12 2D TMDs for photodetectors. **(a)** Schematic diagram of a $MoTe_2/MoS_2$ vdW heterostructure device under infrared light excitation. **(b)** Schematic illustrations of type-II interband excitation processes in $MoTe_2/MoS_2$ vdW heterostructures. The value of interband gap (Δ) is obtained by theoretical calculation. **(c)** Optical Microscopy image (upper panel) and schematic illustration (bottom panel) of the $WSe_2/SnSe_2$ heterojunction device. **(d)** The calculated responsivity on the light power. **(e)** Schematic diagram of device structure based on $CdTe/PtSe_2$ heterostructures. **(f)** Time-dependent photoresponse of the $CdTe/PtSe_2$ heterojunction photodetector under different bias voltages. (a, b) Reproduced from Ref. [170]. Copyright © 2016, American Chemical Society. (c) Reproduced from Ref. [171]. Copyright © 2019, The Royal Society of Chemistry. (d) Reproduced from Ref. [172]. Copyright © 2018, Wiley-VCH. (e, f) Reproduced from Ref. [173]. Copyright © 2018, American Chemical Society.

range can be divided into ultraviolet (UV) (10–400 nm), visible light (400–750 nm), infrared (IR) (750 nm–30 μm) and terahertz (30 μm–3 mm) band. Generally speaking, the key principle for photodetectors is the photoresponsivity, quantum efficiency and detectivity. 2D heterostructures are preferred for high-end photodetectors by virtue of enhanced optical absorption, promoted carrier separation and low dark current [278, 279]. Among different types of 2D heterostructures, TMDs with a type-II or type-III band alignment are promising for high-performance photodetectors. For type-II or type-III heterostructures, the dominating carrier relaxation method is the interlayer charge transfer mechanism rather than the interlayer energy mechanism [169, 257–260], resulting in a high dissociation efficiency of electron–hole pairs due to the strong built-in electric field. Zhang *et al.* [170] demonstrated a staggered type-II band alignment of $MoTe_2/MoS_2$ vdW heterostructures [Fig. 12(a)]. As shown in Fig. 12(b), the interlayer gap between MoS_2 and $MoTe_2$ is 0.657 eV (~1880 nm), which allows a transition from the valence band maximum of $MoTe_2$ to the conduction band minimum of MoS_2 under infrared light with a wavelength of longer than 1200 nm. The device performance can also be enhanced by tuning band alignment. For example, Xue *et al.* [171] fabricated a high-photoresponsivity and broadband photodetector based on a $WSe_2/SnSe_2$ vertical heterostructure. The band structure could be engineered from type-II to type-III band alignment by applying a large negative gate and a reverse bias voltage on the source-drain electrodes [Fig. 12(c)]. Due to the enhanced tunneling current density, the heterostructure photodetector showed a high photoresponsivity up to 588 A/W with a wavelength of 532 nm and 80 A/W with a wavelength of 1550 nm, while the photodetectivity of visible and telecommunication wavelengths reached 4.4×10^6 Jones and 1.4×10^{10} Jones.

Self-powered infrared photodetectors are highly preferred for their low dark current and power consumption. A built-in electric field is formed by asymmetric Schottky junctions because of the different work functions of 2D semiconductors and metals, which enables self-powered light detectors. For instance, Zhou *et al.* [172] constructed a self-powered metal-semiconductor-metal WSe_2 photodetector with an asymmetric contact geometry. A high responsivity of 2.31 A/W was obtained under zero bias [Fig. 12(d)]. The external quantum efficiency (EQE) was about 22% when the light power was

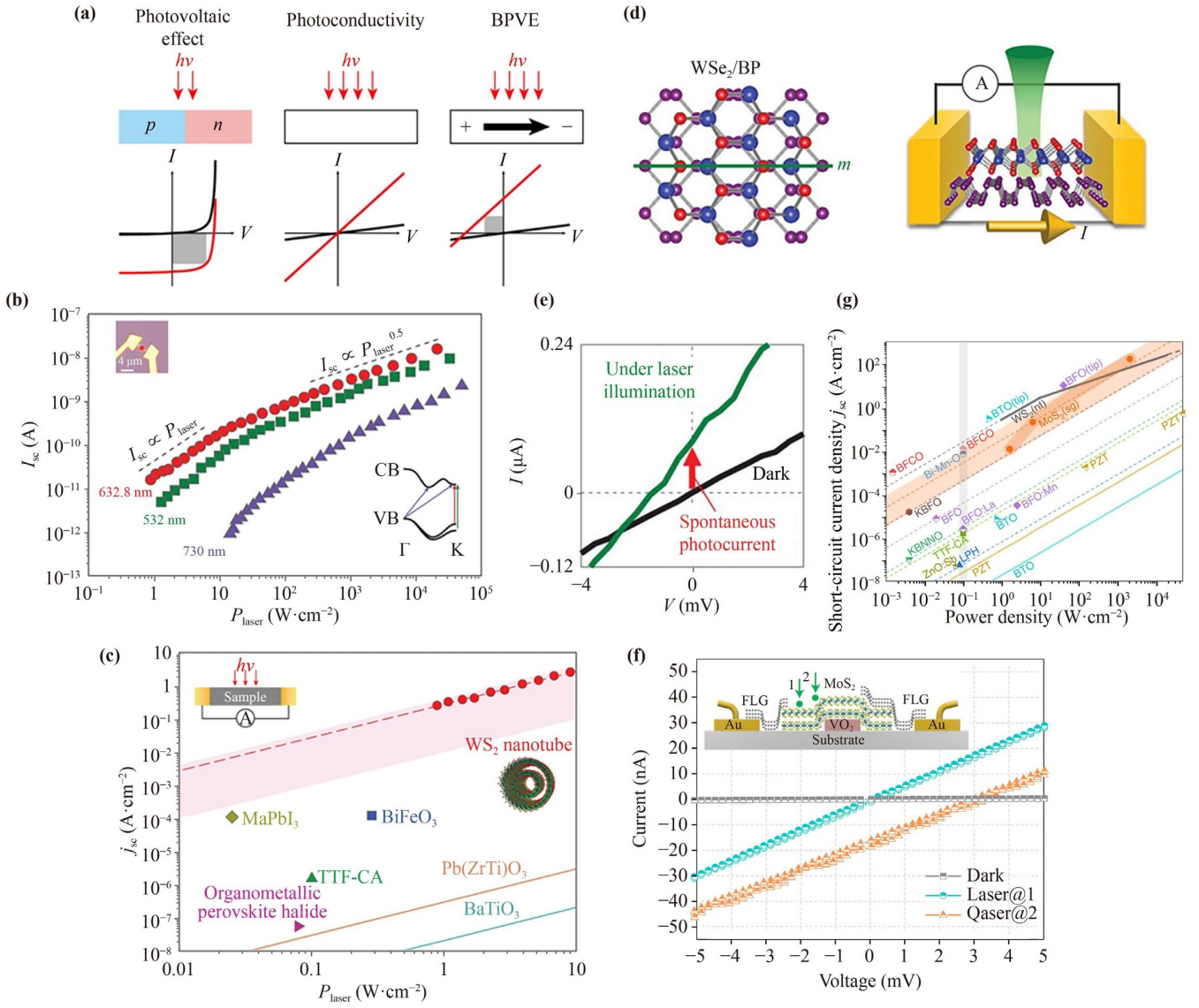

Fig. 13 2D TMDs for bulk photovoltaic effect (BPVE). **(a)** Schematic illustrations of photovoltaic effect in traditional p–n junction and BPVE in non-centrosymmetric monolayer crystals. **(b)** Dependence of I_{sc} on P_{laser} for three different wavelengths. The black dashed lines are guides to the eye. The bottom right inset illustrates possible excitation paths from the valence band (VB) to the conduction band (CB) for each wavelength, using the same colour scheme as the data points. Inset, optical micrograph of the device. **(c)** The BPVE in various materials. **(d)** Schematic illustrations of heterointerface of WSe_2/BP (left) and the experiment device (right). **(e)** I–V characteristic of the WSe_2/BP device. **(f)** I–V characteristic of the MoS_2-based device under laser (532 nm) illumination at spot 1 (Laser@1) and 2 (Laser@2) and without illumination (Dark). Inset: A schematic of the cross-sectional view of the device. **(g)** Short-circuit current density j_{sc} versus incident power density in reported non-centrosymmetric materials. (a–c) Reproduced from Ref. [178]. Copyright © 2019, Springer Nature. (d, e) Reproduced from Ref. [179]. Copyright © 2021, The American Association for the Advancement of Science. (f, g) Reproduced from Ref. [180]. Copyright © 2021, Springer Nature.

27 nW at zero bias, which increased to 65.6% when the light power was 27 nW. The higher EQE with lower light power suggested the existence of the photoconductivity gain effect in the WSe_2. Noble metal dichalcogenides like $PtSe_2$ can be applied to the fabrication of self-powered photodetectors for their widely tunable bandgaps, large electrical conductivity and high air stability. Yuan *et al.* [173] demonstrated wafer-scale PtS_2/$PtSe_2$ photodetectors with zero-bias photoresponse under laser illumination of different wavelengths (405–2200 nm). Based on this foundation, Wu *et al.* [174] replaced PtS_2 with CdTe and the photodetectors showed a broader detection coverage range of 200–2000 nm with a higher specific detectivity of 4.2×10^{11} Jones as well as a faster response speed of 8.1/43.6 μs at room temperature [Figs. 12(e, f)].

Recently, photovoltaic effect driven by ferroelectrics, especially the bulk photovoltaic effect (BPVE), has come to the foreground. The bulk photovoltaic effect only exists in crystals with broken inversion symmetry, which can lead to a significant electronic polarization [175]. Typically, a strong zero-bias photocurrent (or shift current) can be observed in non-centrosymmetric crystals when irradiated with light above the energy bandgap [176, 177]. As presented in Fig. 13(a), in traditional p–n junctions, external light sources induce the creation of electron–hole pairs and their subsequent separation, generating a light current, which is known as the photovoltaic effect, whose efficiency has been increased dramatically, almost reaching the theoretical limit. However, in non-centrosymmetric monolayer crystals, BPVE, which converts solar power into electric power without the supply of p–n junctions, can be present provided that the incident light is linearly polarized along specific directions, whereas circularly polarized light is not allowed to do so. When threefold rotationality and mirror symmetry of the 2D sheets are destructed by curvature or strain, light can induce BPVE irrespective of its polarization characteristics. Experimentally, mirror and rotational symmetry is broken in WSe_2 nanotubes because of the curvature [178]. The short-circuit current (I_{sc}) under laser illumination is related to the laser wavelength. With the same laser power (P_{laser}), I_{sc} (632.8 nm) is greater than I_{sc} (532 nm) and I_{sc} (730 nm) [Fig. 13(b)], which can be explained that the light with a wavelength of 632.8 nm (1.96 eV) is nearly resonance with an A-exciton (a specific bound state of an electron and a hole) of WSe_2 and therefore the strongest signal is produced. Compared with that for other ferroelectric bulk materials, the short-circuit current density (j_{sc}) of WSe_2 nanotubes is orders of a larger order of magnitude with the same P_{laser} [Fig. 13(c)]. Moreover, the diameter of the nanotubes (~100 nm) is much smaller than that of the laser spots (1–2 μm), indicating higher actual deviations in the efficiency of WSe_2 nanotubes. Akamatsu *et al.* [179] noticed the lattice mismatch between WSe_2 and BP interface, which reflected both the trigonal symmetry of WSe_2 and the anisotropic potential of BP that induced the in-plane polarity of the interface [Fig. 13(d)]. As shown in Fig. 13(e), a typical short-circuit current under zero bias, or a spontaneous photocurrent is observed after laser illumination but not under dark conditions. A spontaneous photocurrent is observed along the polar direction and is absent in the direction perpendicular to it, which could be explained by a quantum-mechanical shift current that reflects the geometrical and topological electronic nature of the emergent interface. Very recently, Jang *et al.* [180] demonstrated the bulk photovoltaic effect of MoS_2 using a strain-gradient engineering approach based on the structural inhomogeneity and phase transition of a hybrid system consisting of MoS_2 and VO_2. As shown in Fig. 13(f), the current-voltage curves are measured at regions with small (Spot 1) and large (Spot 2) strain gradients as well as (Laser@1 and Laser@2) and without illumination (dark) for comparison. A large short-circuit photocurrent is observed at Spot 2, proving that there is a positive correlation between the intensity of BPVE and the strain gradient. The strain gradient of MoS_2 can be tuned by the temperature-induced structural phase transition of the VO_2 microbeam. Meanwhile, the short-circuit current density (j_{sc}) of MoS_2 is of an order of magnitude higher than that of most reported non-centrosymmetric materials [Fig. 13(g)], which enriches new concepts and materials for the potential application of BPVE.

In summary, we have reviewed the recent progress in photodetectors based on 2D TMDs, pointing out the key principles for photodetectors to convert optical signals into electrical signals and research findings about self-powered infrared photodetectors. What's more, we also discussed the development of recent bulk photovoltaic effect on 2D TMDs, which highlighted the potential of 2D ferroelectrics for high-end photodetectors and other photoelectric devices.

3.2.2 Optoelectronic memory devices

Compared with general electronic memory devices, nonvolatile optoelectronic memory devices are integrated with the advantages including the high speed of optical recording and large differences of electrical readout signals. Among different wavelength spectra, infrared illumination has been mostly used in optical recording due to its low energy dissipation. For example, Wang *et al.* [181] exploited an infrared optoelectronic memory device using few-layer MoS_2/PbS heterostructures [Fig. 14(a)], whose infrared pulse (808, 1340, 1550 and 1940 nm) intrigued a persistent resistance that lasted for more than 10^4 s and a reconfigurable switch of 2000 stable cycles. However, the storage performance disappeared above 200 K, which can be improved by inserting a buffer layer. Similarly, Yin *et al.* [182] demonstrated a $MoS_{2x}Se_{2(1-x)}$ optoelectronic memory by tuning sulphur vacancies and isoelectronic selenium atoms via synergistic effect [Fig. 14(b)]. With the aid of charge trapping effect, the devices possessed a high programing/erasing ratio (~10^8) and a short switching time. As illustrated in Fig. 14(c), the response time of electro- (photo-) excitation is about 0.3 (0.9) ms. Figure 14(d) presents two memory states after electrically programing and optically erasing with a negligibly-changed current over 5×10^3 s, indicating superb charge retention characteristics.

To achieve high-performance optoelectronic memory devices, it is necessary to obtain the rapid recombination of electron–hole pairs, and a high external quantum efficiency (EQE). However, the lifetime of photocarriers tends to be shortened due to the rapid recombination of

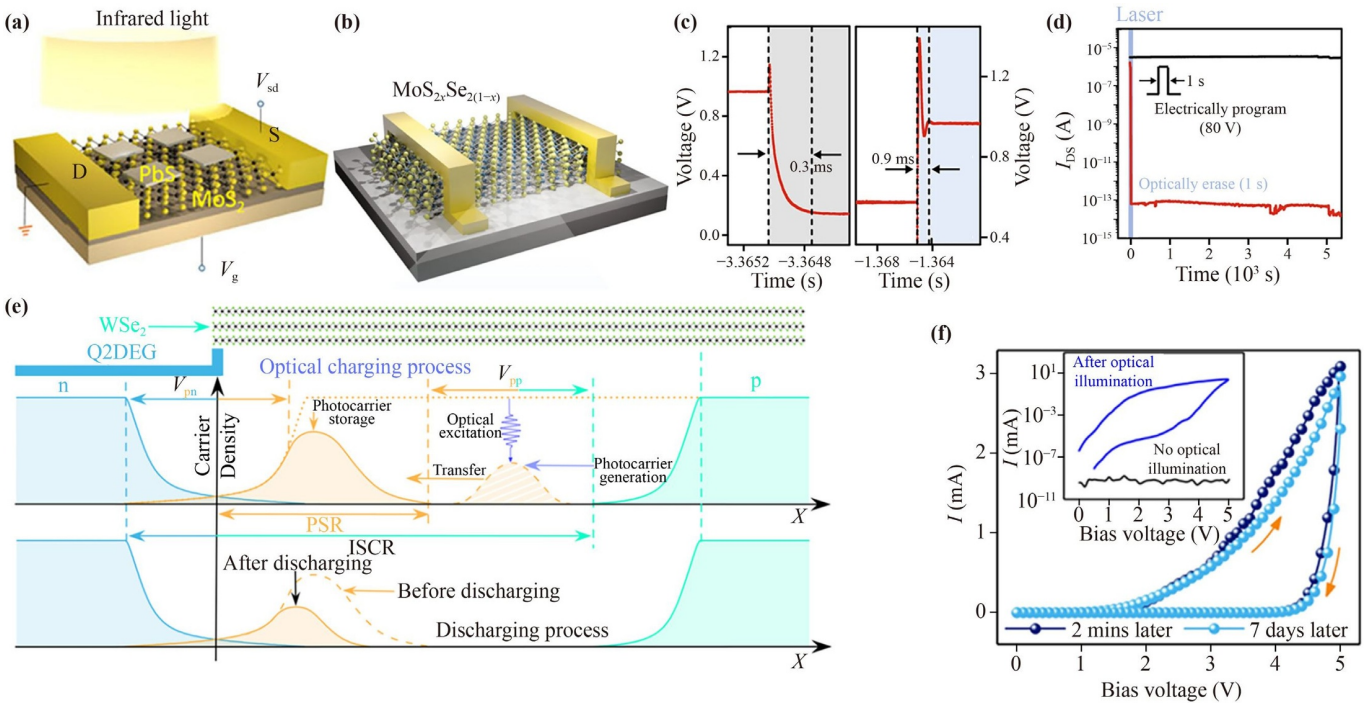

Fig. 14 2D TMDs for optoelectronic memory devices. **(a)** Schematic of infrared memory device based on few-layer MoS_2/PbS nanoplates heterostructure as channel. **(b)** Schematic structure of the device based on $MoS_{2x}Se_{2(1-x)}$ alloys. **(c)** Photoresponse time of the electro-(left panel) and photo-excitation (right panel) process. The laser wavelength is 1550 nm. **(d)** Retention performance of two memory states after electrically programming and optically erasing. **(e)** Schematic showing the generation, storage, and release of photocarriers stored in the ISCR in the WSe_2-Q2DEG vdW heterostructure for the optical charging and discharging. **(f)** *I*–*V* loops measured in darkness 2min later and 7 days later. Inset: *I*–*V* curves without and after optical illumination. (a) Reproduced from Ref. [181]. Copyright © 2018, The American Association for the Advancement of Science. (b–d) Reproduced from Ref. [182]. Copyright © 2019, Springer Nature. (e, f) Reproduced from Ref. [184]. Copyright © 2021, American Physics Society.

electron–hole pairs , limiting the EQE [183]. In addition to previously-mentioned charge trapping methods, Jiang *et al.* [184] recently focused on extending the lifetime of photocarriers by constructing a vdW junction between a WSe_2 layer and quasi-2D electron gas (Q2DEG). As shown in Fig. 14(e), after optical excitation, infinite-lifetime photocarriers are generated in the intrinsic space charge region (ISCR) and are stored in the photogenerated hole storage region (PSR). During discharging, the bias voltage applied causes the release of the photogenerated holes stored in the ISCR. Due to the infinite lifetime of the photocarriers stored in ISCR, the photons scattered in the environment can be randomly gathered and accumulated so as to generate a large photocurrent. As presented in Fig. 14(f), after being kept in darkness for 2 min or 7 days, a large photocurrent of about 2.9 mA can be observed with a bias voltage increased to 5 V in darkness. Moreover, the device can maintain the same level of photocurrent even after 1000 cycles, exhibiting a fine repeatability.

As a whole, current optoelectronic memory devices based on 2D TMDs have exhibited huge advantages with a high storage density, a high repeatability (a long retention time and an excellent switching endurance), ease of processing and a flexible size. However, the read-in gate voltage and power dissipation of 2D TMD photoelectronic memory devices still need to be lowered to decrease thermal noise, and multivalued memory devices possessing more than two distinct current states are required to achieve a multi-system logic input and a higher storage density for future application.

3.3 Ferroelectrics

3.3.1 Ferroelectric field effect transistors (FeFETs)

Ferroelectrics are typically insulators exhibiting a spontaneous electric polarization arising from ordered arrangement of electric dipoles [250, 277], which can be controlled by external electric and stress fields within a certain temperature range. According to the Lyddane–Sachs–Teller relationship, when the temperature is lower than the critical temperature, the long-range force (dipole interaction) is equal to the short-range force (such as Pauli repulsion), resulting in zero frequency of the corresponding phonon branch, which indicates that the phonon mode is frozen. The specific surface area of ultrathin films increases rapidly and the depolarization

field is significantly enhanced, which suppresses the ferroelectric polarization. Among traditional perovskite ferroelectrics, the ferroelectricity has been shown to disappear with a film thickness of below 24 Å in $BaTiO_3$ [185] and with that of below 12 Å in $PbTiO_3$ [186], which is not conductive to the subsequent fabrication of ultrathin ferroelectric devices. 2D TMDs, especially for those with a 1T-type structure, have exhibited great potential in the application of ferroelectrics. Shirodkar *et al.* [187] theoretically predicted the emergence of ferroelectricity in a monolayer 1T-MoS_2 using a combination of Landau theoretical analysis and first-principles calculations, in which $MoSe_2$, WS_2 and WSe_2 are applied equally well. The two sulphur lattice planes are staggered so that each Mo site becomes the center of inversion, which makes 1T-MoS_2 exhibit ferroelectricity. Experimentally, ferroelectricity has been proved to exist in 1T-phase or 1T′-phase 2D TMDs down to the atomic monolayer limit [188, 189], which inspires exciting studies on the application of ferroelectric devices.

Generally speaking, the ferroelectric materials integrated into the FET gate stack can be divided into three popular device types: metal/ ferroelectric/ semiconductor (MFS), metal/ ferroelectric/ insulator/ semiconductor (MFIS) and metal/ ferroelectric/ metal/ insulator/ semiconductor (MFMIS) device structure. MFS structure is the simplest FET device structure. Compared with traditional FET structures, ferroelectric materials replace traditional MOSFET gate oxides as the dielectric layer. Through tuning electron transport in the electric field, the channel conductivity can be tuned to achieve a nonvolatile ferroelectric memory. In the MFIS structure, an insulator layer is clamped between the ferroelectric and semiconductor layer to prevent interdiffusion and interface reactions. Moreover, the insulator layer provides a potential barrier for charge injection between the ferroelectric and semiconductor substrate, stabilizing the ferroelectric properties in the negative-capacitance region. Based on the MFIS structure, a bottom electrode is added between the ferroelectric film and the insulating layer to form an MFMIS structure. Compared to MFIS structures, the floating gate inserted in MFMIS structures leads to the normalization of polarization charge density and interface potential in independent ferroelectric domains, resulting in capacitance mismatch and obvious hysteresis. Therefore, an MFIS structure is more popular for the fabrication of FeFETs. For instance, Huang *et al.* [190] fabricated dual-gated 2D FeFETs using a Cr-Au/ $CuInP_2S_6$(CIPS)/h-BN/MoS_2 structure [Fig. 15(a)]. Through the configuration of an inserted h-BN insulator layer and a dual-gated coupling device, ferroelectric CIPS can be substantially stabilized and polarized. Through structural improvements, the device exhibits a large memory window, a high ON/OFF ratio of 10^7, an ultralow programming state current of 10^{-13} A under P-state and a long-time endurance of 10^4 s as a nonvolatile memory, as presented in Fig. 15(b). Similarly, Zhang *et al.* [191] recently proposed multilevel nonvolatile memory devices (FeFET) adopting the structure of $MoS_2/Al_2O_3/Bi_{0.85}La_{0.15}Fe_{0.92}Mn_{0.08}O_3$(BLFMO)/$n^+$-Si, where n^+-Si was selected to serve as the substrate for conducting a back gate [Fig. 15(c)]. With the tunable conductivity of the MoS_2 channel by applying gate voltage pulses of different amplitudes, the FeFETs exhibited memory windows of 25 V, a high ON/OFF ratio of 10^5 and a remarkable programing/erasing ratio of 10^4 [Fig. 15(d)].

Despite the capacitance mismatch in the MFMIS structures, the floating metal serves as an internal gate electrode to estimate the voltage amplification. Moreover, the metal electrode provides potential to achieve a sub-60 mV/dec subthreshold swing (*SS*) in an NC-FET [192]. For example, Liu *et al.* [193] demonstrated MoS_2 NC-FETs with an *SS* value down to 42.5 mV/dec, which was below the physics limit. As the schematic of MoS_2 NC-FETs shows [Fig. 15(e)], the inserted HfO_2 layer prevents the ferroelectric P(VDF-TrFE) polymer film from fatigue with a robust stability. As a result, the NC-FETs possess superior performance with a transconductance of 45.5 $\mu S \cdot \mu m^{-1}$ and an on/off ratio of 4×10^6 with channel length less than 100 nm. At the same time, the *SS* values exhibit a nonlinear dependence with temperature due to the implementation of a ferroelectric gate back [Fig. 15(f)]. Based on this, Wang *et al.* [194] demonstrated a sub-5 nm gate-length sub-thermionic FET using a 4.3nm metallic carbon nanotude as the gate terminal and obtained sub-thermionic switching behavior with a minimum *SS* of 6.1 mV/dec at room temperature. Moreover, Wang *et al.* [195] demonstrated MoS_2 NC-FETs with an ultralow *SS* of 4.97 mV/dec. Apart from NC-FETs, Dirac-source (DC) FETs, replacing traditional sources with a Dirac source (usually graphene) whose density of states is negatively correlated with energy, show a great potential to break through the thermionic limit of *SS*, which is 60 mV/dec [196].

In the reported 2D FeFETs, most 2D TMDs serve as semiconducting channels. But as is mentioned before, ferroelectricity emerges in some TMDs like *d*1T-$MoTe_2$ [188] and WTe_2 [189] experimentally. Very recently, Weston *et al.* [197] demonstrated proof-of-principle FETs using marginally-twisted mono- or few-layer MoS_2 with interfacial ferroelectricity at room temperature. The broken inversion symmetry and the asymmetry of atomic arrangement at the interface enable ferroelectric domains with an alternating out-of-plane polarization. As shown in Figs. 15(g) and (h), a pronounced hysteresis of the conductivity governed by the pinning of ferroelectric domain walls is observed for twisted 1L and 3L MoS_2 ($\theta = 0°$). The observations provide possibilities towards the design of new FeFETs using 2D ferroelectric TMDs.

As a whole, FeFETs based on 2D TMDs show a great potential with tunable polarization switching and a low

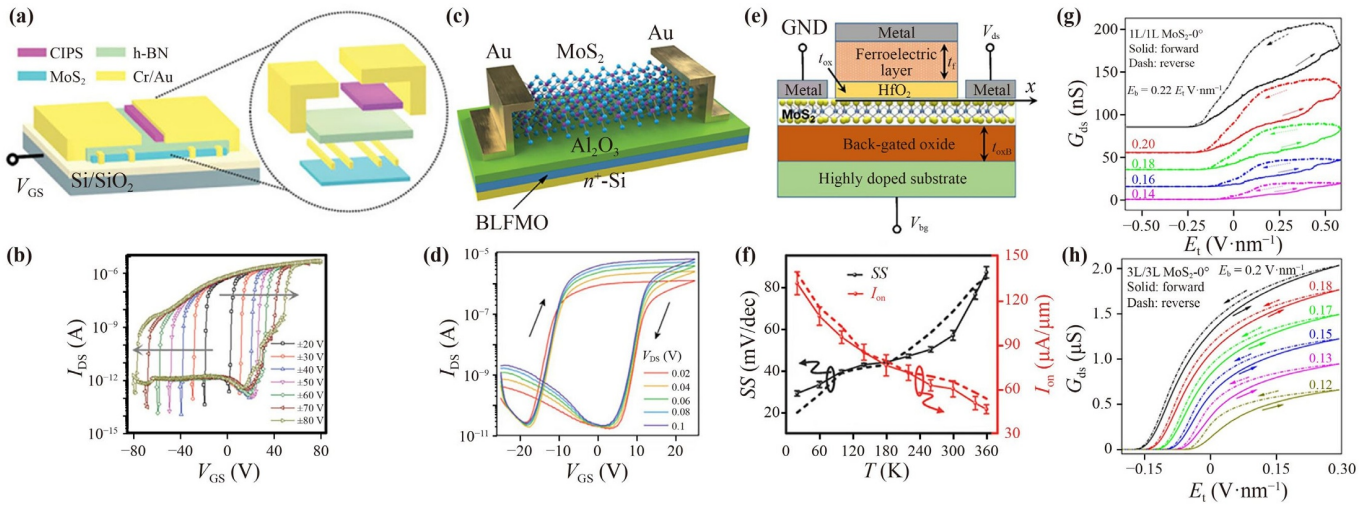

Fig. 15 2D TMDs for FeFETs. **(a)** 3D schematic diagram of the ferroelectric vdWHs device with MoS_2 as channel material, h-BN as insulating layer, and CIPS as ferroelectric dielectric layer. **(b)** The transfer characteristic curves of the ferroelectric vdWHs device under different back gate voltage ranges, ±20 to ±80V, step: 10 V; V_{DS} = 50 mV. **(c)** Schematic diagram of the MoS_2-based FeFET configuration. **(d)** Transfer characteristic curves of the FeFETs at various V_{DS} from 0.02 to 0.1 V. **(e)** Schematic of MoS_2 NC-FETs. **(f)** SS values plot extracted from experimental data and simulated results to show the dependence with temperature. The error bars are the statistical analyses for 10 MoS_2 NC-FETs with the same device geometry. **(g, h)** Hysteretic behavior of electrical conductivity G_{DS} of marginally twisted MoS_2 as a function of top-gate electric field E_t for different back-gate electric fields (E_b). The shown curves are for 1L MoS_2 on top of 1 L MoS_2 at 350 K (f) and 3L/3L MoS_2 at room temperature (g) twisted by 0° to achieve the 3R interface. (a, b) Reproduced from Ref. [190]. Copyright © 2020, Wiley-VCH. (c, d) Reproduced from Ref. [191]. Copyright © 2021, Wiley-VCH. (e, f) Reproduced from Ref. [193]. Copyright © 2018, Wiley-VCH. (g, h) Reproduced from Ref. [197]. Copyright © 2022, Springer Nature.

SS below the theoretical limit for next-generation nonvolatile memories with a low power consumption.

3.3.2 Ferroelectric tunnel junctions (FTJs)

FTJ is a tri-layer metal-ferroelectric-metal (MFM) structure consisting of two metal electrodes and a ferroelectric tunnel barrier. The reversal of the polarization via external electric fields would change the potential energy barriers and switch the tunneling resistance, which is known as the tunneling electroresistance (TER) effect. ON and OFF states are formed in the FTJs with a reversible tunnel current through the TER effect. Generally speaking, the TER ratio ($\frac{J_{ON}-J_{OFF}}{J_{OFF}}\times100\%$) is one of the standards to judge the quality of FTJs (higher the better). It has been revealed that the TER effect would be greatly improved by replacing one of the metal electrodes with a heavily-doped semiconductor with the reversibly accumulated and depleted majority carriers as the semiconductor interface [198]. For example, Li *et al.* [199] demonstrated hybrid $MoS_2/BaTiO_3/SrRuO_3$ FTJs with a high OFF/ON resistance ratio of 10^4, a 50-fold increase in comparison with the same type of FTJs with metal electrodes. Figure 16(a) illustrates the polarization-induced changes in the band structure of the MoS_2/BTO/SRO junction, where the application of negative biases to MoS_2 pushes the Fermi level down to attract sufficient electrons injected from the tip to be accumulated and trapped at the interface, stabilizing the polarization. As a result, the OFF/ON resistance ratio exceeds 10^4 at a read voltage of 0.1 V when the entire area of BTO films underneath the MoS_2 flake is uniformly poled [Figs. 16(b, c)]. Recently, Chaudhary *et al.* [200] fabricated $MoS_2/Hf_{0.5}Zr_{0.5}O_2$ (HZO)/W FTJs. Compared with traditional perovskite ferroelectric films, HfO_2-based films with different dopants show a higher scalability and compatibility through complementary metal oxide semiconductor (CMOS) technology [201, 202]. Polarization switchability was initially tested via piezoresponse force microscopy (PFM) on a bare HZO surface [Fig. 16(d)]. A similar butterfly-type PFM hysteresis loop was observed in FTJs, indicating the switchability of HZO underneath MoS_2 [Fig. 16(e)]. Respectively, the enhanced ratio of ~10^3 observed in MoS_2/HZO/W is at least an order of magnitude larger than those of HZO-based FTJs with metallic (Pt, TiN, and Au) or heavily-doped Si semiconductor electrodes [203–205].

2D TMDs like MoS_2 have proved to enhance the TER effect with reversibly accumulated and depleted majority carriers as the semiconductor interface. The superiority suggests a great potential of the FTJs for neuromorphic computation, the electromagnetic multistate memories and a potential compatibility with CMOS process. However, more works are still required to push FTJ devices into real applications.

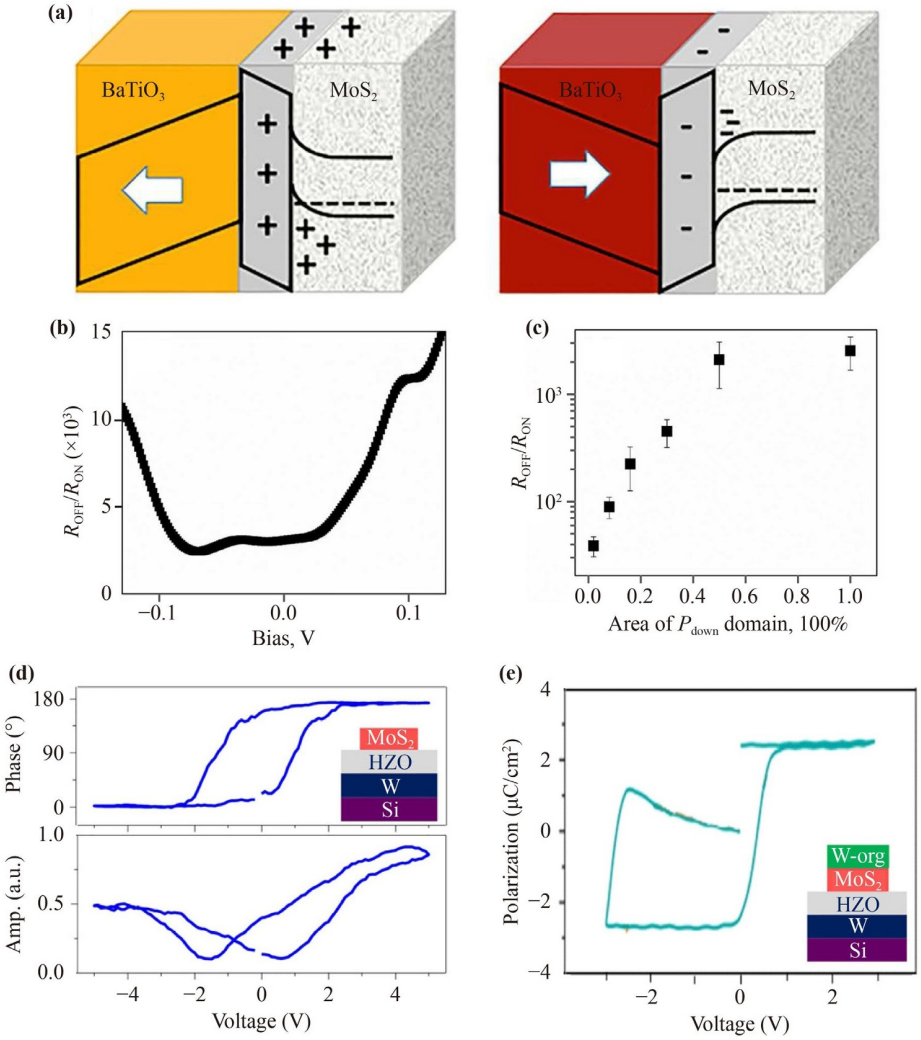

Fig. 16 2D TMDs for FTJs. **(a)** Schematic illustration of polarized-induced changes in the band structure of the MoS_2-BTO-SRO heterojunction. **(b)** The reading bias dependence of the R_{OFF}-to-R_{ON} ratio, where R_{ON} and R_{OFF} resistances correspond to the polarization states completely switched with the downward and upward direction. **(c)** Dependence of the R_{OFF}-to-R_{ON} ratio on the area of domains with the downward polarization(ON state) normalized to the total area of the MoS_2 flake. **(d)** Local PFM phase and amplitude hysteresis loops acquired on the MoS_2/HZO/W heterojunction. **(e)** A remanent P–V loop measured in a W-org/MoS_2/HZO/W device. (a–c) Reproduced from Ref. [199]. Copyright © 2017, American Chemical Society. (d, e) Reproduced from Ref. [200]. Copyright © 2021, AIP Publishing.

Based on the polarization direction of 2D ferroelectrics as is discussed above, several nonvolatile random-access memory structures have been fabricated, exhibiting an outstanding switching speed, a low subthreshold swing that is below theoretical limit as well as a superior scalability and reliability. Apart from traditional ferroelectric materials, several 2D vdW materials have been confirmed to show sliding ferroelectricity where the vertical electric polarization is switched due to in-plane interlayer sliding [206, 207], broadening 2D ferroelectrics from very few material candidates to most of the known 2D TMDs. Moreover, without significant vertical ion displacements in the clean vdW interfaces, the vertical polarization can be switched through in-plane interlayer sliding with a very low barrier, which can be utilized for high-end data writing with an ultralow energy dissipation. However, due to the weak charge transfer in the vdW interfaces, the polarization is still very low. For example, the polarization obtained in WTe_2 bilayer is below 0.4 pC/m [206], which is almost three orders of magnitude lower than the bulk polarization of $BiFeO_3$, a traditional ferroelectric material. More follow-up works are required to achieve high-performance ferroelectric and optical devices with a high mobility and a low energy dissipation.

3.4 Ferromagnetics and spintronics

3.4.1 Spin field-effect transistors (sFETs)

A sFET is a three-terminal device with the same structure

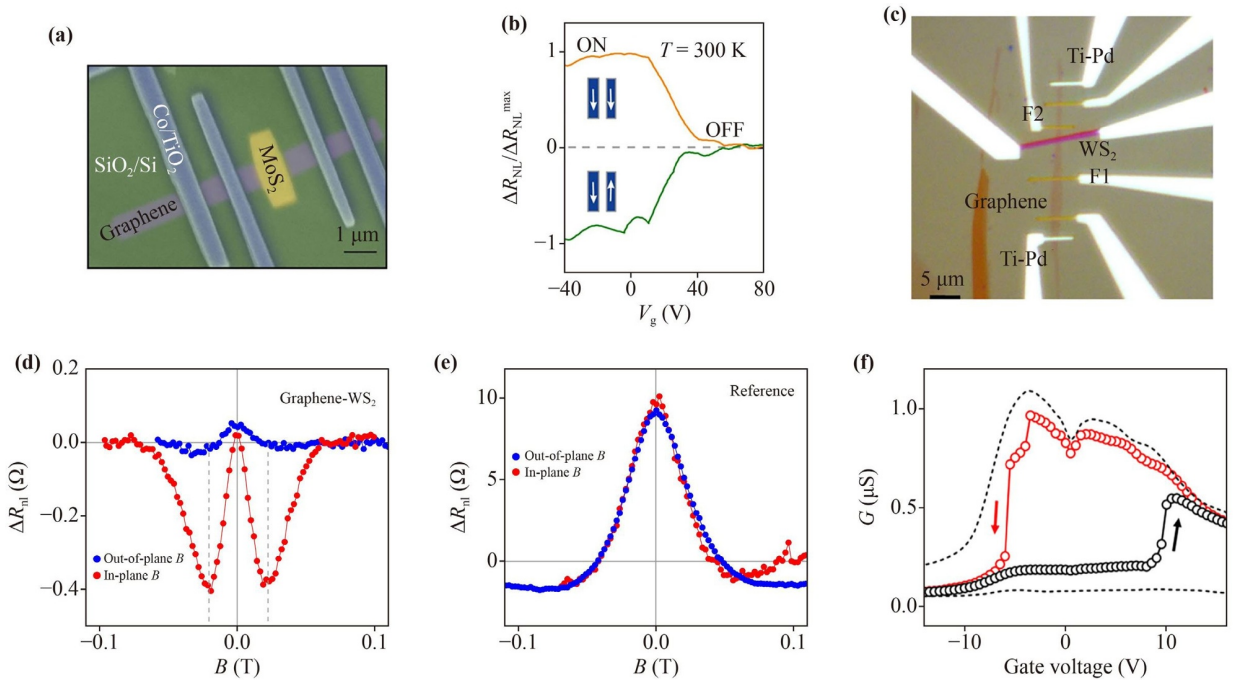

Fig. 17 2D TMDs for sFETs. **(a)** Colored scanning electron microscope image of a fabricated device with a CVD graphene/MoS_2 heterostructure channel, Si/SiO_2 substrate as a gate electrode for control of the spin polarization in the channel, and multiple FM tunnel contacts of TiO_2(1 nm)/Co(80 nm). **(b)** Modulation of spin-valve signal magnitude ΔR_{NL} with gate voltage V_g, showing ON/OFF states at 300 K. **(c)** Enhanced-contrast optical image comprising one graphene/WS_2 heterostructure device and two reference graphene devices enclosing it. **(d, e)** ΔR_{nl} versus B for a graphene/WS_2 heterostructure device and a reference device (without WS_2). **(f)** Tunnel conductance of a TFET with a four-layer CrI_3 tunnel barrier under a constant magnetic bias of 1.77 T. A change of ~400% is seen in the tunnel conductance. (a, b) Reproduced from Ref. [31]. Copyright © 2017, Springer Nature. (c–e) Reproduced from Ref. [211]. Copyright © 2018, Springer Nature. (f) Reproduced from Ref. [215]. Copyright © 2019, Springer Nature.

as ordinary electric FETs. The difference is that the spin polarized current between the ferromagnetic source and the drain is used in sFETs through a 2D electron gas channel [208]. A vertical electric field can modulate the polarization and magnetoresistance by tuning the spin precession arisen from spin-orbit coupling in 2D electron gas channels. In a zero magnetic field, spin-orbit interaction (the Rashba term of effective mass Hamiltonian H_R) leads to spin splitting in the 2D electron gas of wide-bandgap semiconductors. The source performs as a spin polarizer for the spin of carriers injected into it and the drain performs as a spin filter allowing electrons with the same polarization direction to pass through while rejecting all other electrons with a different polarization [209]. With a complete electric field regulation in a very small volume within very short time, sFETs provide the potential for high-speed digital integrated circuits based on spin polarization.

Experimentally, Dankert *et al.* [210] demonstrated the electric gate control of the spin current and spin lifetime at room temperature by combining graphene with MoS_2 in a vdW heterostructure [Fig. 17(a)]. Graphene is an excellent material for spin transport due to its low spin-orbit coupling (SOC) and high electron mobility, while MoS_2 possesses a high SOC and a wide bandgap. Therefore, the spin lifetime and diffusion length can be controlled by electrical gate in such 2D heterostructures at room temperature. As shown in Fig. 17(b), the non-local (NL) resistance normalized to the maximum value is controlled by gate voltage, demonstrating transistor-like ON/OFF states. Benitez *et al.* [211] unambiguously demonstrated the anisotropic spin dynamics of bilayer heterostructures comprising graphene and WS_2 or MoS_2. As is presented in Fig. 17(c), a multilayer TMDC flake was placed over graphene between two ferromagnetic injector (F1) and detector (F2) electrodes. The non-local spin resistance $R_{nl} = V_{nl}/I$ can be determined by the voltage V_{nl} at the Detector F1 and the current I at the Detector F2. In an isotropic system, the $R^{\pm}_{nl,iso}$ is in the form of $R^{\pm}_{nl,iso} = [\pm g(B)\cos^2\gamma + \sin^2\gamma]R_{nl,0}$ for initially parallel (+) and anti-parallel (–) magnetization configurations, with $g(B)$ as the function that captures the precession response [212–214]. By defining $\Delta R_{nl} = R^{+}_{nl} - R^{-}_{nl}$, the influence of Orientation B orientation can be eliminated from this spin isotropic system with a small tilting angle γ. As shown in Figs. 17(d) and (e), the ΔR_{nl} obtained for B in (red) and out of (blue) plane can be very different for the graphene–WS_2 and the reference

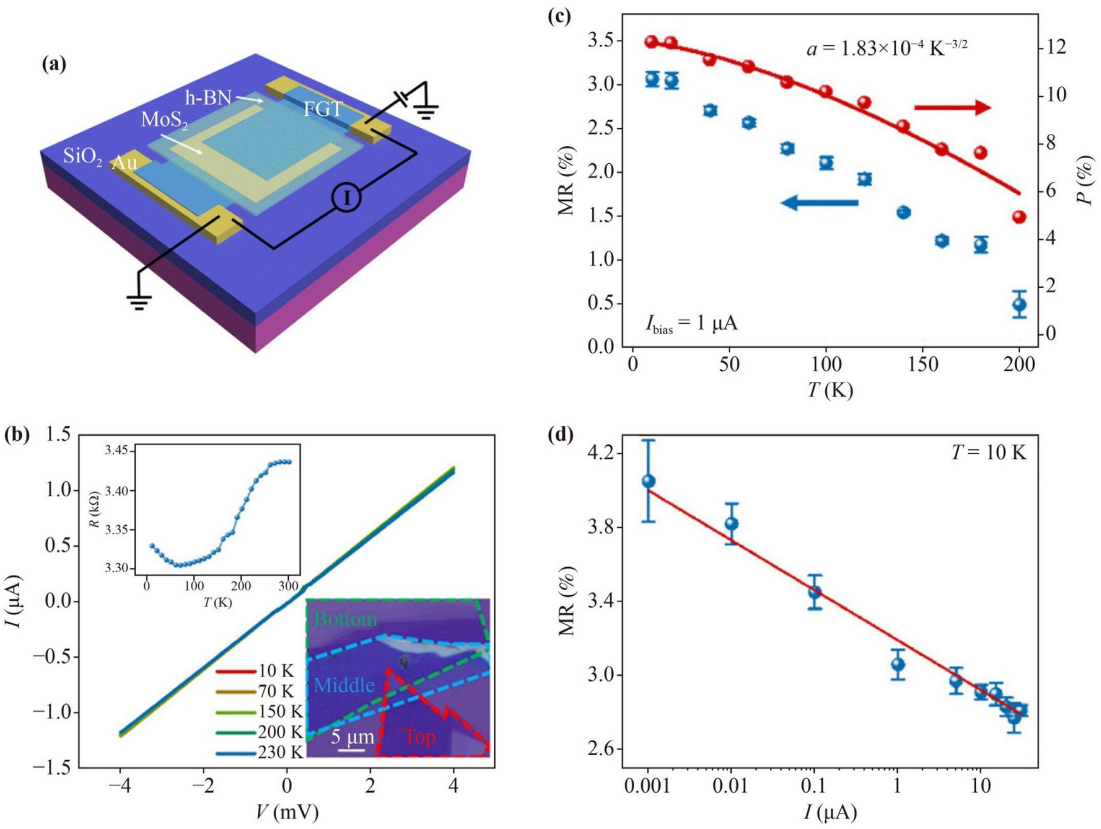

Fig. 18 2D TMDs for MTJs. **(a)** Schematic diagram of the FGT/MoS_2/FGT spin valve encapsulated by a top h-BN capping layer (~50 nm thick). **(b)** I–V curves of the FGT/MoS_2/FGT heterojunction at some representative temperatures. The R–T curve and optical image are displayed in the upper-left and bottom-right corner, respectively. **(c)** MR and spin polarization P as a function of temperature. The curve presents the fitting result according to Bloch's law. **(d)** MR versus bias current. The red line is not the fitting but guides the eye. (a–d) Reproduced from Ref. [216]. Copyright © 2020, American Chemical Society.

device without WS_2. The disparity of the curves in Fig. 17(d) demonstrates the highly anisotropic nature of spin transport in graphene–WS_2. Moreover, the lifetime of spin varies depending on its spin orientation over one order of magnitude, indicating a strong anisotropic spin relaxation in graphene–WS_2 heterostructures.

However, the strong spin relaxation and low spin injection efficiency in channels make it difficult to achieve a large high-low magnetoresistance ratio using traditional 2D sFET devices. To solve this problem, Jiang *et al.* [215] fabricated spin tunnel FETs based on dual-gated graphene/CrI_3/graphene tunnel junctions. A bilayer CrI_3 barrier exhibits two magnetization configurations controlled by the gate voltage: two antiferromagnetically-coupled monolayers, so the high-low tunnel conductance can approach 400% with a four-layer CrI_3 barrier [Fig. 17(f)]. The device provides a new approach for exploring non-volatile and reconfigurable spin polarization memories and logic applications.

3.4.2 Magnetic tunnel junctions (MTJs)

A 2D magnetic tunnel junction (MTJ) is composed of two ferromagnetic layers as electrodes and a thin insulating layer based on tunneling magnetoresistance (TMR) effect. The magnetization direction of one ferromagnetic layer can be reversed by applying a small external magnetic field due to the weak or zero interlayer coupling between the two ferromagnetic layers, resulting in a huge high-low tunneling resistance. For traditional 3D FTJs, the effect of the interface between the ferromagnetic and insulating layer is very hard to control. However, the interface interaction of 2D layered materials like graphene and MoS_2, is connected by vdW force without chemical bonds. Moreover, due to the large spin splitting caused by spin–orbit interaction, the spin polarization can be maintained in the out-of-plane direction of TMDs.

For instance, Lin *et al.* [216] fabricated a spin valve device based on Fe_3GeTe_2/MoS_2/Fe_3GeTe_2 heterostructures, where two FGT thin flakes served as the ferromagnetic electrodes and the semiconducting MoS_2 served as the barrier layer [Fig. 18(a)]. As presented in Fig. 18(b), the linear I–V curves illustrate good Ohmic contacts at the FGT/MoS_2 interfaces. Meanwhile, the resistance decreases initially and then increases slightly

with a decreasing temperature due to the strong hybridization between the interface of S atoms and Fe/Te/Ge atoms as well as Kondo effect. By performing magnetotransport measurements with a two-terminal setup, the magnitude of the MR can reach 4.1% under a bias current of 1 nA at 10 K [Figs. 18(c,d)], which is around 10 times larger than that in conventional NiFe/MoS_2/NiFe. The two phases of TMDs provide unprecedented opportunities to design vdW heterostructures with a unique magnetic transfer structure. Yang *et al.* [217] designed two types of MTJs by inserting 2H-WTe_2 or 2H-$MoTe_2$ as a tunneling barrier with 1T-$MoTe_2$ as the electrode. Thanks to the large spin polarization of the devices, the total conductance for a parallel orientation is two orders of magnitude larger than that for an antiparallel orientation of 1T devices and is three orders of magnitude larger than that for the 2H devices, which results in a TMR of 5.6×10^3% and 1.7×10^5% for the 1T and 2H MTJs. In addition, by inserting vdW heavy materials with strong intrinsic spin-orbit coupling (SOC), the spin polarization of MTJs can be tunable and switchable. Klaus *et al.* [218] predicted graphene sandwiched among semiconducting monolayers of ferromagnet $Cr_2Ge_2Te_6$, and WS_2 will exhibit a spin-orbit torque (SOT) driven by an unpolarized charge current. The ratio of filed-like and damping-like components of SOT can be tuned by more than an order of magnitude via combined top and back gates, which is different from conventional metallic ferromagnets in contact with 3D SOC materials.

3.4.3 Spin-polarized light-emitting diodes

In addition to spin field-effect transistors and magnetic tunnel junctions, spin-polarized light-emitting diodes are another potential semiconductor spintronic device, which transfer spin polarization into circularly-polarized light. Compared with traditional electronic LEDs, spin-polarized carriers in spin LEDs are injected into activated areas to produce circularly-polarized light through radiative recombination with holes or electrons. The very earliest spin-polarized LEDs are fabricated using III–V heterostructures based on GaAs [219]. However, due to the low Curie temperature of magnetic semiconductors and the mismatch of electric conductance, the spin injection efficiency is of these devices not high.

Most TMD monolayers like WS_2 and MoS_2 are nonmagnetic semiconductors with inversion symmetry breaking, resulting in a strong SOC and the splitting of the valence bands into spin-up and spin-down states [Fig. 19(a)], which can be useful for the circular polarization of light emitted due to spin injection. Ye *et al.* [220] fabricated n-WS_2 /p-(Ga,Mn)As heterostructures and observed valley-polarized light emission from the spin-valley locking in WS_2 monolayers [Fig. 19(b)]. The electroluminescence helicity, ρ , can be tuned applying magnetic field with different directions. As shown in Fig. 19(c), when injecting spin-up holes with a magnetic field outward towards the sample, the K valley is populated, resulting in right-circularly popularized light emission. The electroluminescence helicity, ρ , can reach 16.2%, indicating a strong valley polarization in the heterostructures. When applying an inward magnetic field, an opposite ρ of ~14.8% can be observed due to the injection of the opposite spin-down holes and the population of the opposite valley, K′ [Fig. 19(d)]. Similarly, Sanchez *et al.* [32] also achieved spin LEDs by spin injection from Ni/Fe electrodes into a vertical heterojunction based on monolayers of WSe_2 and MoS_2 as well as the lateral transport of spin-polarized holes within the WSe_2 layer.

Atomically thin CrI_3 exhibits layer-dependent ferromagnetism where adjacent ferromagnetic monolayers are antiferromagnetically coupled. Zhong *et al.* [221] demonstrated a circular polarization-resolved photoluminescence in heterostructures formed by monolayer WSe_2 and bi/trilayer CrI_3 at zero magnetic field. By performing a co-circular polarized excitation, the time reversal symmetry of WSe_2 is broken because of the magnetic proximity effect. When the photoexcited electron spin in WSe_2 has the same orientation as the CrI_3 magnetization, the charge transfer is allowed. Otherwise, it is suppressed [Fig. 19(e)]. The spin-dependent charge transfer from WSe_2 to CrI_3 gives rise to a strongly circularly-polarized photoluminescence [Fig. 19(f)].

External magnetic fields or contact with ferromagnetic semiconductors are used in those mentioned above to create a circularly-polarized electroluminescence and photoluminescence. However, the use of such substrates/electrodes and the strict need for external magnetic fields limit the applicability in terms of device integration, operation ability and electrical reliability [222]. In this regard, another approach is to control circularly-polarized electroluminescent by applying asymmetrical lateral electric fields. Zhang *et al.* [223] reported an electrically-switchable chiral light-emitting transistor based on WSe_2 thin flakes. As presented in Fig. 19(g), the electric double-layer transistor (EDLT) enables a simultaneous accumulation of both electrons and holes inside the channel, leading to light emission from the heterostructures. The circular polarization is reversed when the source-drain bias is exchanged, as is shown in Fig. 19(h). However, ionic liquid freezes in such devices at 100 K while the source and drain biases are exchanged when it is at least 220 K, which is not convenient for the application of industrial devices. Therefore, spin-polarized LEDs using asymmetrical electric fields that can stably operate at room temperature are greatly acquired.

Recently, the pure electrical generation of valley magnetization by breaking the three-fold rotational symmetry of TMDs via external strain has been proposed [224, 225]. The out-of-plane magnetization is independent of in-plane magnetic fields, which is linearly proportional to the in-plane current density and is optimized when the current is orthogonal to the strain-

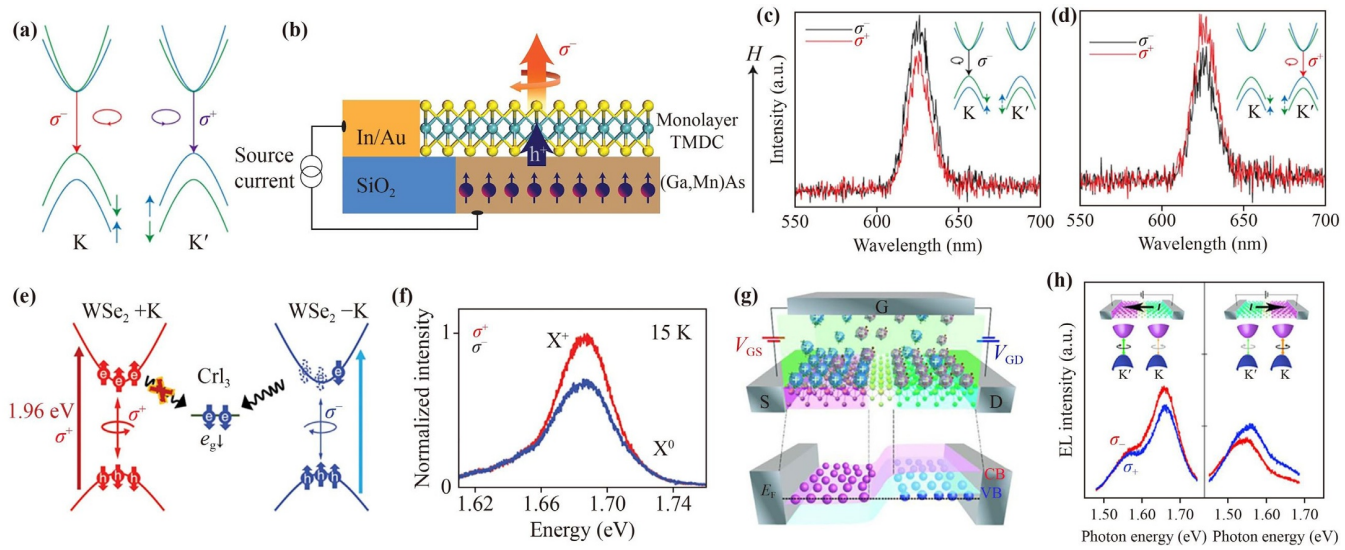

Fig. 19 2D TMDs for spin-polarized LEDs. **(a)** Schematic of electronic structure at the K and K′ valleys of monolayer TMD and valley polarization via spin injection. **(b)** Schematic of the monolayer TMD/(Ga, Mn)As heterojunction for electrical valley polarization devices. (Ga, Mn)As was used as a pin aligner under an external magnetic field. **(c, d)** Spectra of σ^- and σ^+ resolved electroluminescence polarized under an outward (c) or inward (d) magnetic field of 400 Oe perpendicular to the surface with a current of 15 μA. Inset: Schematic representation of electrical excitation and emission processes. **(e)** Schematic depicting spin-dependent charge transfer in monolayer WSe2 and trilayer CrI_3 vdW heterostructure. **(f)** Polarization-resolved photoluminescence of a WSe2/trilayer CrI_3 vdW heterostructure at 15 K and zero magnetic field, showing spontaneously σ^+ polarized photoluminescence. **(g)** Schematic structure of TMD EDLT under ambipolar charge accumulation (top) and band structure of EDLT-induced p–i–n junction under equilibrium (bottom). **(h)** Top: Circularly polarized EL spectra for two opposite current directions. Bottom: Illustrations of EL intensity contributed from two valleys. (a–d) Reproduced from Ref. [220]. Copyright © 2016, Springer Nature. (e, f) Reproduced from Ref. [221]. Copyright © 2020, Springer Nature. (g, h) Reproduced from Ref. [223]. Copyright © 2014, The American Association for the Advancement of Science.

induced piezoelectric field. Based on this model, relevant spin LEDs have been fabricated with strained TMD monolayers, even at room temperature [226, 227].

As a whole, to achieve room-temperature spin-polarized LEDs, further research and optimization of spin injection and active regions are required towards the application of novel spintronic devices such as optical transmission and quantum cryptography.

3.5 Valleytronics

3.5.1 Valleytronic transistors

In a crystalline solid, the local minimum of its conduction band or the local maximum of its valence band is commonly known as "valley". In addition to charge and spin, valley degree of freedom (DoF) is also considered to be used to distinguish electrons due to its long lifetime. Similar to the spin-up and spin-down states of spintronics, valley polarization, or valley pseudospin, provides the potential to store and carry information without traditional electron flow [228]. The earliest theoretical work reporting valley polarization is inverted by the local application of a gate voltage to the point contact regions in graphene [229]. Later, in TMDs with a similar broken reversal symmetry like graphene, the electronic properties at the band edge are dominated by merging energy, but inequivalent valleys which occur at the +K and –K point at the edges of the Brillouin zone. In systems with a strong SOC, the carrier concentration between each pair of valleys is significantly different, resulting in valley pseudospin. In general, there are two types of valley polarization: excitonic valley polarization by circularly polarized light excitation and free carrier (electron or hole) valley polarization via strong spin-valley coupling. Both types of valley polarization can be controlled by the gate voltage [6, 230–232]. Jin *et al.* [231] demonstrated the efficient generation of a pure and locked spin-valley diffusion current in WS_2/WSe_2 heterostructures without applying any driving electric field [Fig. 20(a)]. By adjusting the valley-polarized hole concentration with gate voltage, the diffusion constant can be tuned, so as to control the spin-valley lifetime and diffusion time [Figs. 20(b,c)]. Therefore, the valley information can be output in the form of electrical signals and can be tuned by electrostatic gates, which provides necessary conditions for fabricating valleytronic transistors.

For example, Li *et al.* [233] demonstrated a room-temperature valley transistor based on monolayer MoS_2, which enabled a full sequence of generating, propagating, detecting and manipulating valley information. As illus-

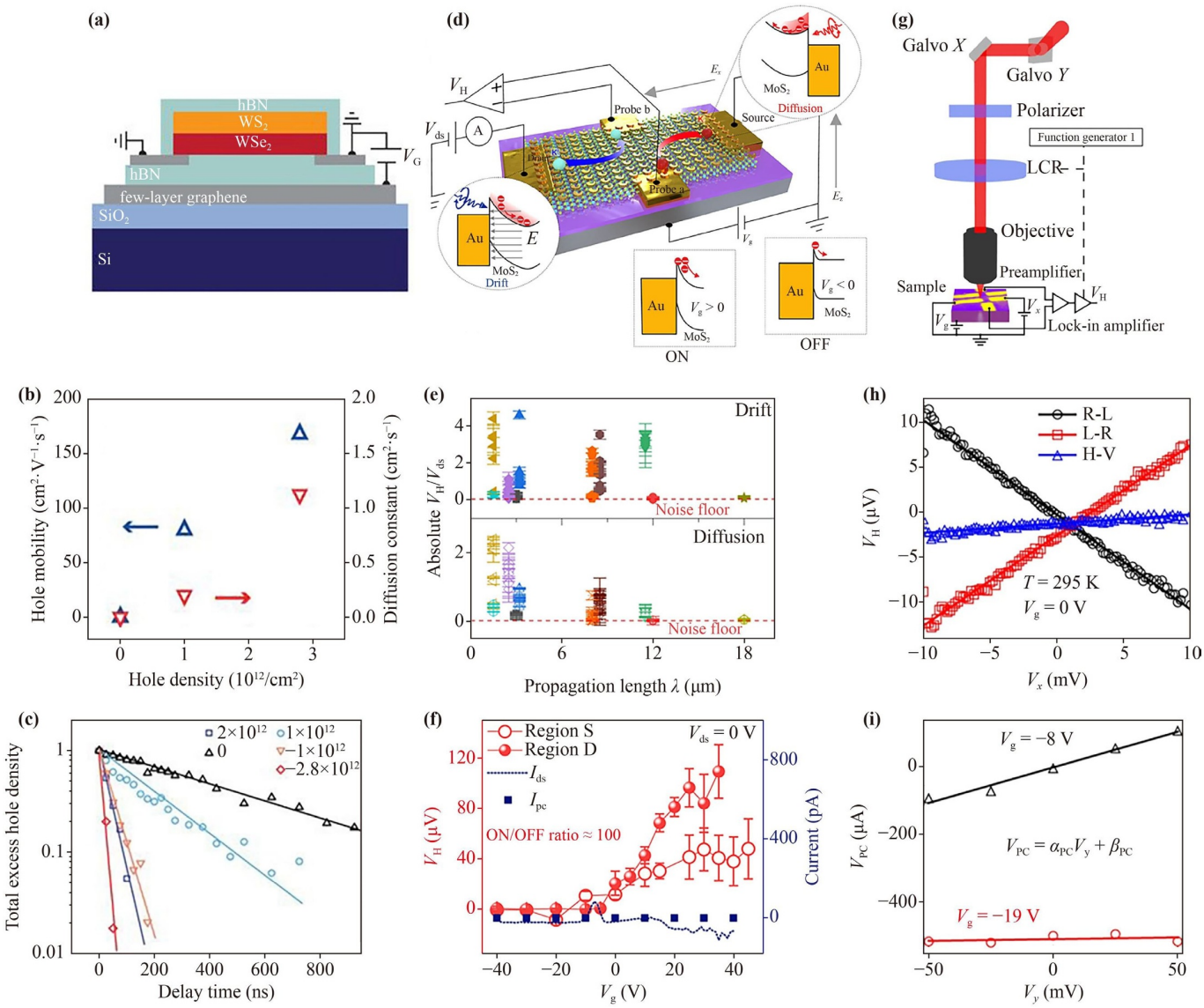

Fig. 20 2D TMDs for valleytronic transistors. **(a)** Side-view illustration of the WSe_2/WS_2 heterostructure device. **(b)** Extracted hole diffusion constant (red) and mobility (blue) show a strong dependence on the initial hole concentration. **(c)** Decay dynamics of the total excess hole density at different initial carrier concentrations. The decay lifetime is longest near charge neutrality and decreases with both electron doping (positive carrier concentration) and hole doping (negative carrier concentration). **(d)** Schematics and operation mechanism of the valleytronic device. The device comprises a standard MoS_2 transistor, two lateral Hall probes and a purposely aligned chiral plasmonic antennae array. **(e)** Statistics of the measured valley Hall voltage in ten devices for drift (top panel) and diffusive (bottom panel) transport. **(f)** Hall voltage as a function of gate voltage V_g at $V_{ds} = 0$ V. **(g)** Experimental setup of the Hall measurement in MoS_2/WSe_2 heterostructure. **(h)** Observation of VHE at room temperature. The black, red and blue symbols are the measured difference between the Hall voltage under right- and left-circular polarization (R–L), under left- and right-circular polarization (L–R) and under horizontal and vertical polarization (H–V), respectively. The lines are linear fits. **(i)** Linear fitting of V_{PC} versus $V_y = -8$ V (black line) and $V_g = -19$ V (red line) at 240 K. (a–c) Reproduced from Ref. [231]. Copyright © 2018, The American Association for the Advancement of Science. (d–f) Reproduced from Ref. [233]. Copyright © 2020, Springer Nature. (g–i) Reproduced from Ref. [234]. Copyright © 2021, Springer Nature.

trated in Fig. 20(d), a 1550 nm infrared laser is focused on the contact to realize an artificial valley-selective charge injection in a MoS_2 channel by means of a helicity-conserved hot carrier injection. Similar to the charge current, the valley-polarized current can be transferred in the form of diffusion or drift and characterized by valley Hall effect. The locked spin-valley polarization of carriers leads to a very long valley lifetime and results in long propagation length of valley-polarized electrons [8 μm for diffusion and 18 μm for drift, shown in Fig.

20(e)]. Moreover, the valley information can be modulated through electrostatic gating like a charge transistor. As presented in Fig. 20(f), the Hall voltage from diffusive transport can be controlled by a gate voltage under zero V_{ds} and the ON/OFF current ratio reaches about 100.

Apart from monolayer MoS_2, the valley Hall effect has also been reported in TMD heterostructures. Recently, Jiang *et al.* [234] created a gate-tunable bipolar valleytronic transistor based on MoS_2/WSe_2 heterostructures [Fig. 20(g)]. A set of galvo mirrors were used to scan the laser beams across the samples for an optical excitation and the Hall voltage could be measured under the circularly-polarized light. As shown in Fig. 20(h), the Hall voltage V_H shows a linear dependence on the bias voltage V_x for circular polarization modulation (R-L and L-R), while the V_x -dependence of V_H for linear polarization modulation (H-V) is negligible. Besides, the photocurrent can be modulated by an electrostatic gate under an unpolarized excitation. As presented in Fig. 20(i), the value of V_{PC} is fitted with the function $V_{PC} = \alpha_{PC}V_y+\beta_{PC}$, confirming the gate tunability of VHE polarity. The full gate tunability can be used to improve the ON/OFF ratio of the valleytronic transistors and to create more compact valleytronic logic circuits.

To conclude, valley-controlled polarization was realized at the zero external electric field V_{ds} via valleytronic transistors [235, 236], and the power consumption of devices could be lower due to the independence of charge flow. However, the main factors limiting the realization of device application include: (i) The current valley polarization injection method is mainly composed of the introduction of circularly-polarized light and asymmetric magnetic fields, which can be very complicated [237]. (ii) The lifetime of valleytronic transistors is much shorter than that of traditional electric transistors [238] and most work temperatures are below room temperature. (iii) The detection methods of valley polarization are very complex at present. Despite various challenges, it is clear that valleytronic transistors are expected to pave a way towards more than Moore integrated photonic chips based on CMOS structure technology.

3.5.2 Valley-photodetectors

As is mentioned above, circularly-polarized light excitation can induce excitonic valley polarization, which may lead to the realization of novel valley optoelectronic devices like valley-photodetectors. Compared with conventional photodetectors, valley-photodetectors convert optical signals into electric signals due to the circular photogalvanic effect. Monolayer MoS_2 and other semiconducting TMDs exhibit valley Hall effect induced by a strong SOC and the valley optical selection rule can be used to generate spin-polarized photoexcitation. For example, Luo *et al.* [239] demonstrated lateral an opto-valleytronic spin injection across a monolayer MoS_2/few-layer graphene interface with circularly-polarized light at room temperature [Fig. 21(a)]. The electrical spin detection can be identified as an antisymmetric Hanle curve through voltage signals on a ferromagnetic (FM) electrode. As illustrated in Fig. 21(b), the voltage signal V_{NL} varies approximately linearly with B_y because the spin precession angle varies linearly with the field, while V_{NL} eventually reaches the maximum and decreases as the average precession angle exceeds ~90°, confirming that V_{NL} comes from the valley-locked spins from MoS_2. Similarly, a valley-locked spin photocurrent can be detected in WS_2/graphene/Bi_2Se_3 heterostructures [240] [Fig. 21(c)]. In comparison with FM electrodes, the topological insulator Bi_2Se_3 possesses only an in-plane spin texture and the measured polarity of the valley-locked spin photocurrent naturally reflects the valley-polarized carriers. Inversion-symmetry breaking plays a major role in generating the valley-polarized DoFs with spin DoF textures partially governed by Rashba spin splitting [241], respectively. As shown in Figs. 21(d) and (e), by measuring local and non-local photocurrents, the two coupled DoFs can be distinguished. The optically-generated polarization degree P shows a marked difference between local and non-local structures, as is presented in Fig. 21(f). The non-local P exhibits a quadratic gate voltage V_g dependence because the Rashba spin splitting also includes the V_g-dependent terms. It is noteworthy that the valley-photocurrent can be controlled using an in-plane field and back gating. Rasmita and coworkers [242] observed a geometrically-dependent photocurrent in MoS_2/WSe_2 heterostructures, where light with a different circular polarization generated photocurrents in opposite directions. A liquid crystal modulator was used to modulate the optical polarization. Both the circular photocurrent I_{CPGE} and polarization-independent photocurrent $\bar{I}_{SD}$ approach to zero as the back-gate voltage goes to a more negative value. After replacing the liquid crystal modulator with a quarter-wave plate (QWP), all photocurrents still approach to zero as the back-gate voltage is reduced, indicating that the in-plane electric field affects both the magnitude and polarity of the circular photocurrent while the polarity of circular photocurrents is not changed by the back gating.

Since valley DoFs have been considered as a novel method to distinguish electrons, the valley polarization of valleytronic devices can be generated, transferred, detected and controlled as electronic devices do. Despite the rapid progress in the study of valleytronic devices based on 2D TMDs, like the room-temperature valleytronic transistors and photodetectors mentioned above, much more work is still required to lengthen the spin-valley lifetime and simplify the detection procedure. Recently, TMD superlattices exhibit an enhanced valley polarization via strain or moiré twisting [243–247], shedding light on designing intriguing valleytronic devices

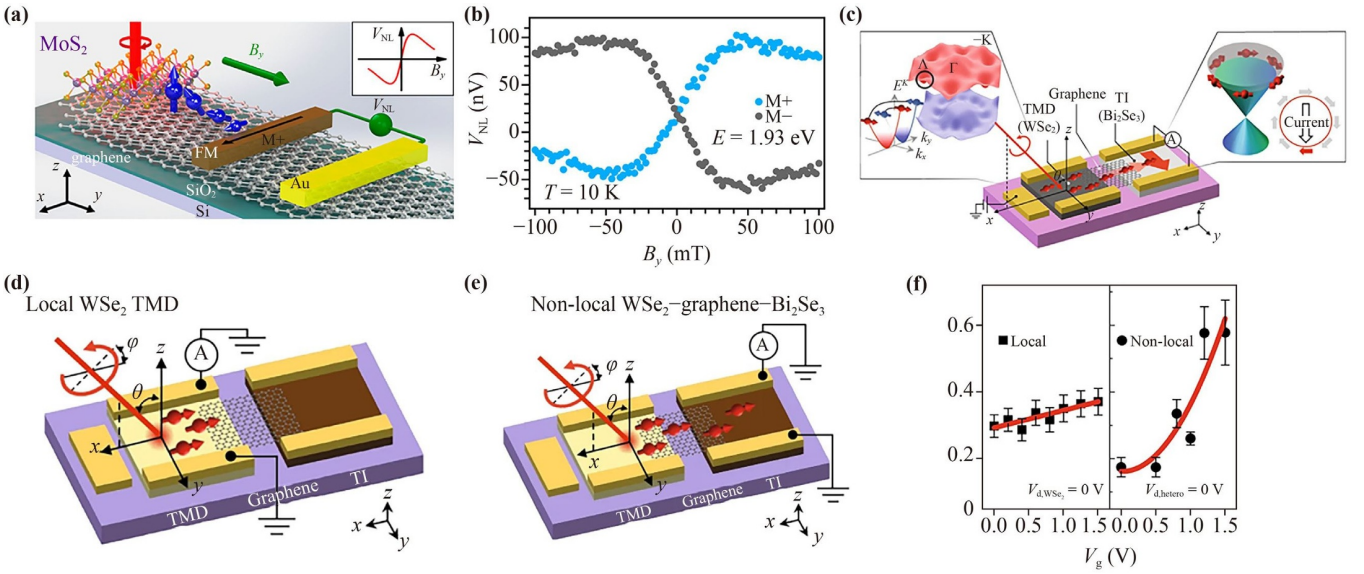

Fig. 21 2D TMDs for valley-photodetectors. **(a)** Illustration of optical spin injection, lateral spin transport, and electrical spin detection in a monolayer MoS_2/few-layer graphene hybrid spin valve structure. Inset: Expected signal V_{NL} as a function of applied magnetic field B_y. **(b)** Electrical spin signal V_{NL} as a function of B_y exhibits clear antisymmetric Hanle spin precession signals which flip polarity with the Co magnetization direction (M^+ vs. M^-). **(c)** Schematic representation of the non-local measurement in WSe_2/graphene/Bi_2Se_3 heterostructures. **(d, e)** Schematic diagrams of the local helicity-dependent photocurrent in WSe_2 (a) and non-local helicity-dependent photocurrent in WSe_2/graphene/Bi_2Se_3 heterostructures. **(f)** Optically generated polarization degree P as a function of V_g for the local and non-local CPGE measurement at $V_d = 0$ V. (a–c) Reproduced from Ref. [239]. Copyright © 2017, American Chemical Society. (d–f) Reproduced from Ref. [240]. Copyright © 2018, Springer Nature.

such as high-speed integrated-frequency converters, broadband autocorrelators for ultrashort pulse characterization and tunable nanoscale holograms [248, 249].

3.6 Physico-chemical applications

In addition to the aforementioned physical applications, some other physico-chemical applications such as batteries, catalysts and gas sensors based on 2D TMDs have been highlighted in recent years. Owing to abundant adsorption sites for metal-ion insertion process and tunable phases, 2D TMDs show great potential in energy storage devices. Limited by energy and power densities, the mainstream Li-ion batteries cannot meet the rapidly growing demand for sustainable and clean energy applications, including electric vehicle and smart grid storage. Li-S batteries, with a high theoretical capacity of 1672 mAh·g^{-1} based on the reaction of $16Li + S_8 \leftrightarrow 8Li_2S$, have been regarded as the anodes of choice for the next-generation rechargeable Li-metal batteries [251]. Cha *et al.* [252] coated a 10-nm-thick MoS_2 protective barrier between metallic Li and electrolyte via deposition and dissolution process. The MoS_2 layer shows tight adhesion to the surface of Li metal and facilitates uniform flow of Li^+ into and out of bulk Li metal, improving the Li^+ transport and conductivity between metallic Li and electrolyte. As shown in Fig. 22(a), the capacity of the Li-MoS_2/CNT-S cell stabilizes at ~940 mAh·g^{-1} after 1200 cycles, corresponding to a Coulombic efficiency of ~98%. In addition, the full-cell demonstrates high specific energy and power densities of 589 Wh·kg^{-1} and 295 W·kg^{-1}, exhibiting a high capacity retention of 84% for up to 1200 cycles. The various activate sites and large specific surface area in 2D TMDs have also attracted great attention for catalysis such as hydrogen evolution reaction (HER). In recent years, doping atoms and defects have been introduced as active sites in 2D TMDs to improve HER activity. For example, Yang *et al.* [253] demonstrated 2H $Nb_{1+x}S_2$ (x~0.35) as an HER catalyst with current densities of >5000 mA·cm^{-2} at ~420 mV versus a reversible electrode [Fig. 22(b)]. Via elimination of van der Waals gaps between $Nb_{1+x}S_2$ layers, the conductivity is improved compared with other multiple layers of metallic TMDs. Apart from doping, grain boundaries have been predicted to be highly electrocatalytically active in both Heyrovsky and Tafel mechanisms [254]. Liu *et al.* [255] synthesized wafer-scale atom-thin MoS_2 and WS_2 films with a high density of grain boundaries up to ~10^{12} cm^{-1} by means of Au-quantum-dots-assisted CVD growth. The Au quantum dots play an important role in forming grain boundaries. As shown in Fig. 22(c), in the climbing stage, the Au quantum dots melt and tend to climb onto the MoS_2 monolayer from the SiO_2 substrate due to the surface tension difference. Subsequently, the second

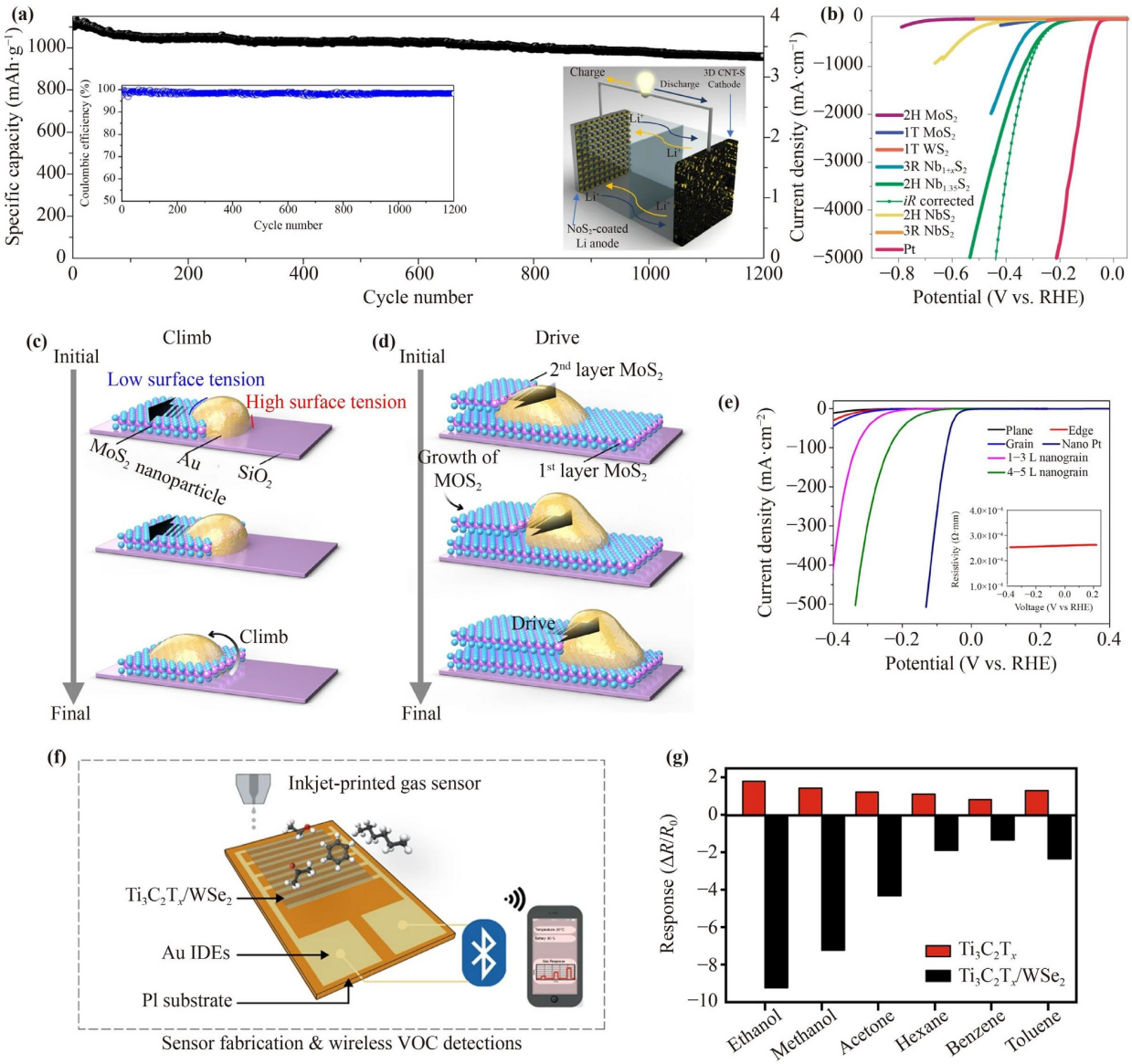

Fig. 22 2D TMDs for physico-chemical applications. **(a)** Long-term cycling performance of Li-S battery with the 3D CNT-S cathode (~33 wt% S content) and the MoS_2-coated Li anode measured at 0.5 C for 1200 cycles. **(b)** HER catalytic activities for different TMDs and Pt measured in 0.5 M H_2SO_4 with a scan rate of 5 $mV \cdot s^{-1}$. **(c, d)** Schematic of self-limiting climb (c) and drive (d) stage growth mechanism of MoS_2 nanograin films. **(e)** Polarization curves of the current density of the MoS_2 devices. The window size is ~80 μm^2 for each device. **(f)** Schematic illustration of inkjet-printed $Ti_3C_2T_x/WSe_2$ gas sensors in detection of volatile organic compounds with a wireless monitoring system. **(g)** Selectivity sensing test of the pristine $Ti_3C_2T_x$ and $Ti_3C_2T_x/WSe_2$ sensors upon exposure to various volatile organic compounds at 40 ppm. (a) Reproduced from Ref. [252]. Copyright © 2018, Springer Nature. (b) Reproduced from Ref. [253]. Copyright © 2019, Springer Nature. (c–e) Reproduced from Ref. [255]. Copyright © 2020, Springer Nature. (f, g) Reproduced from Ref. [256]. Copyright © 2020, Springer Nature.

MoS_2 layer tends to push the Au quantum dots along the growth direction, which will be stabilized at the grain boundaries in order to minimize their surface energy [Fig. 22(d)]. With higher hydrogen adsorption free energies, the single-GB device delivers a better current injection performance than the single-edge device [Fig. 22(e)]. Similarly, numerous 2D TMDs have been applied in gas sensor field where they serve as loading platform for other sensing materials to help contact with gas molecules and improve electron transport efficiency [280]. With outstanding transport properties, 2D TMDs can be easily designed into array arrangement and achieve simultaneous recognition toward multiple gas compounds. For example, Chen *et al.* [256] hybridized WSe_2 with pristine $Ti_3C_2T_x$ and implemented toward detection of various volatile organic compounds [Fig. 22(f)]. In the $Ti_3C_2T_x/WSe_2$ nanohybrids, a large number of electrons released back to the channel are

captured and thus significantly improve sensing response and selectivity in detection of oxygen-containing volatile organic compounds. As presented in Fig. 22(g), compared with pristine $Ti_3C_2T_x$, the nanohybrids show much higher response value in the detection of various oxygen-containing volatile organic compounds, exhibiting better sensing behavior.

4 Conclusion and prospects

In this review, we have summarized the recent progress in modulating properties of 2D TMDs via CVD method and the application of multi-functional devices based on 2D TMDs. As shown in Fig. 23, we focus on a crystal growth mechanism via CVD method, together with modulation and construction techniques developed for 2D TMD-based heterostructures, such as wafer-scale synthesis, phase transition, doping, alloy engineering and stacking direction of heterostructures. Compared with other growth mechanisms, CVD is regarded as the most promising technique for the wafer-scale and high-quality single-crystalline synthesis of 2D TMDs. To obtain high-end wafer-scale TMDs, nucleation at different sites and the interface between domains and surfaces are vital. Currently, a film coverage of 100% cannot be made sure in most studies. In addition, the transfer process from a substrate without damaging as-grown TMDs or introducing contamination [273] still remain a challenge. The phase transition of TMDs can be induced by both physical (temperature, strain, laser irradiation, electrostatic doping, plasma and electric fields) and chemical (intercalation of alkali metals) factors to exhibit novel characteristics for the potential usage of devices. For the doping and alloy engineering of TMDs, traditional strategies applied to silicon can be inappropriate for the atomically thin nature and dangling-bond free interfaces of TMDs. CVD has emerged as an effective method to tune physical and chemical properties via direct composition substitution and indirect electrostatic doping of TMDs. For the stacking direction of heterostructures, CVD is also considered as an applicable method to form hybridized vdW heterostructures with comparably better interface coupling and a higher quality.

Apart from this, recent development of various functional device applications are reviewed and discussed, including electronics, optoelectronics, ferroelectronics, ferromagnetics, spintronics and valleytronics. Although vdW heterostructures based on 2D TMDs have exhibited many unique properties to form high-end next-generation device applications, the integration at a circuit level is still at an early exploration stage, where many challenges remain. For electronic devices, the limited physical spaces of dangling-bond-free interfaces result in inapplicably conventional tuning strategies. Meanwhile, the electric contact with a metal-semiconductor interface

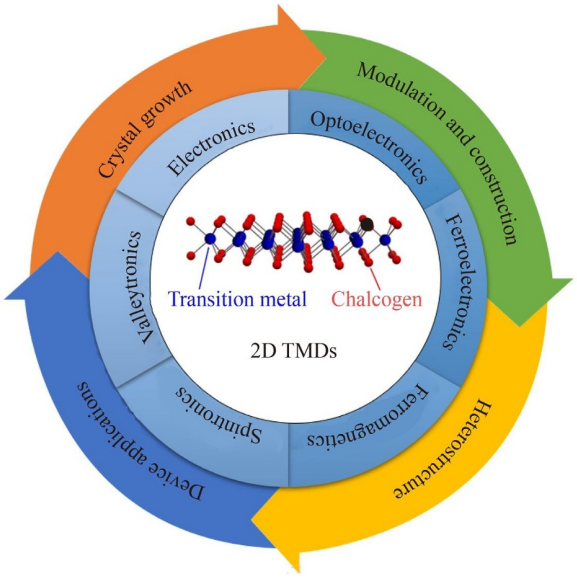

Fig. 23 Schematic representation summarizing the review contents (from crystal growth via CVD method to modulation and construction, and further to 2D TMD based heterostructures, as well as their device applications in various fields).

plays an imperative role in memory performance [274–276], where more efforts should be invested. For optoelectronic devices, a relative slow recombination of electron–hole pairs limits the speed of optical recording and electrical reading-out. Moreover, current photodetectors based on 2D TMDs are mainly concentrated in the near-infrared band, while there are relatively fewer mid- and far-infrared photodetectors. For ferroelectric devices, a low subthreshold swing is achieved for nonvolatile memories with a low power consumption using FeFETs based on 2D TMDTMs. However, the stability of ferroelectric materials in the air is a problem in practical application. For ferromagnetic and spintronic devices, compared with the bulk state, it is hard to achieve 2D ferromagnetic TMDs with an ambient Curie temperature. At the same time, the strong spin relaxation and low spin injection efficiency of channels make it difficult to achieve a large high-low magnetoresistance ratio for spin FETs. For valleytronic devices, the combination of circularly-polarized light injection and traditional silicon-based luminous emission is an attractive field and more efforts need to be made to prolong the lifetime as well as improve work temperature.

Challenges also provide opportunities. Through continued relative theory learning, new properties for further experiment process are predicted and provided. Besides, benign lab-to-fab cooperation is giving impetus to practical device application based on 2D TMDs. Considering many appealing characteristics, 2D TMDs may provide a promising route for future technology advances.

Acknowledgements This work was supported by the National Key R&D Program of China (No. 2018YFA0703700, J.H.), the National Natural Science Foundation of China (Nos. 91964203, J.H., 62004142, Y.W., 62134001, 62104171, R.C., 62104172, L.Y., 62174122, Y.G. and 11774269, S.Y.), the Strategic Priority Research Program of Chinese Academy of Sciences (No. XDB44000000, J.H.), the Natural Science Foundation of Hubei Province, China (Nos. 2021CFB037, R.C. and 2020CFA041, S.Y.), the Fundamental Research Funds for the Central Universities (No. 2042021kf0067, R.C.), and the Special Fund of Hubei Luojia Laboratory.

References

1. S. B. Desai, S. R. Madhvapathy, A. B. Sachid, J. P. Llinas, Q. Wang, G. H. Ahn, G. Pitner, M. J. Kim, J. Bokor, C. Hu, H. S. P. Wong, and A. Javey, MoS_2 transistors with 1-nanometer gate lengths, *Science* 354(6308), 99 (2016)
2. J. S. Ross, P. Klement, A. M. Jones, N. J. Ghimire, J. Yan, D. Mandrus, T. Taniguchi, K. Watanabe, K. Kitamura, W. Yao, D. H. Cobden, and X. Xu, Electrically tunable excitonic light-emitting diodes based on monolayer WSe_2 p–n junctions, *Nat. Nanotechnol.* 9(4), 268 (2014)
3. F. Zhang, H. Zhang, S. Krylyuk, C. A. Milligan, Y. Zhu, D. Y. Zemlyanov, L. A. Bendersky, B. P. Burton, A. V. Davydov, and J. Appenzeller, Electric-field induced structural transition in vertical $MoTe_2$- and $Mo_{1-x}W_xTe_2$-based resistive memories, *Nat. Mater.* 18(1), 55 (2019)
4. T. Akamatsu, T. Ideue, L. Zhou, Y. Dong, S. Kitamura, M. Yoshii, D. Yang, M. Onga, Y. Nakagawa, K. Watanabe, T. Taniguchi, J. Laurienzo, J. Huang, Z. Ye, T. Morimoto, H. Yuan, and Y. Iwasa, A van der Waals interface that creates in-plane polarization and a spontaneous photovoltaic effect, *Science* 372(6537), 68 (2021)
5. L. A. Benítez, J. F. Sierra, W. Savero Torres, A. Arrighi, F. Bonell, M. V. Costache, and S. O. Valenzuela, Strongly anisotropic spin relaxation in graphene–transition metal dichalcogenide heterostructures at room temperature, *Nat. Phys.* 14(3), 303 (2018)
6. K. F. Mak, K. L. McGill, J. Park, and P. L. McEuen, The valley Hall effect in MoS_2 transistors, *Science* 344(6191), 1489 (2014)
7. J. Lu, O. Zheliuk, I. Leermakers, N. F. Yuan, U. Zeitler, K. T. Law, and J. Ye, Evidence for two-dimensional Ising superconductivity in gated MoS_2, *Science* 350(6266), 1353 (2015)
8. K. S. Novoselov, A. K. Geim, S. V. Morozov, D. e. Jiang, Y. Zhang, S. V. Dubonos, I. V. Grigorieva, and A. A. Firsov, Electric field effect in atomically thin carbon films, *Science* 306(5696), 666 (2004)
9. J. Wang, X. Xu, T. Cheng, L. Gu, R. Qiao, Z. Liang, D. Ding, H. Hong, P. Zheng, Z. Zhang, Z. Zhang, S. Zhang, G. Cui, C. Chang, C. Huang, J. Qi, J. Liang, C. Liu, Y. Zuo, G. Xue, X. Fang, J. Tian, M. Wu, Y. Guo, Z. Yao, Q. Jiao, L. Liu, P. Gao, Q. Li, R. Yang, G. Zhang, Z. Tang, D. Yu, E. Wang, J. Lu, Y. Zhao, S. Wu, F. Ding, and K. Liu, Dual-coupling-guided epitaxial growth of wafer-scale single-crystal WS_2 monolayer on vicinal a-plane sapphire, *Nat. Nanotechnol.* 17(1), 33 (2022)
10. X. Xu, Z. Zhang, L. Qiu, J. Zhuang, L. Zhang, H. Wang, C. Liao, H. Song, R. Qiao, P. Gao, Z. Hu, L. Liao, Z. Liao, D. Yu, E. Wang, F. Ding, H. Peng, and K. Liu, Ultrafast growth of single-crystal graphene assisted by a continuous oxygen supply, *Nat. Nanotechnol.* 11(11), 930 (2016)
11. C. Liu, X. Xu, L. Qiu, M. Wu, R. Qiao, L. Wang, J. Wang, J. Niu, J. Liang, X. Zhou, Z. Zhang, M. Peng, P. Gao, W. Wang, X. Bai, D. Ma, Y. Jiang, X. Wu, D. Yu, E. Wang, J. Xiong, F. Ding, and K. Liu, Kinetic modulation of graphene growth by fluorine through spatially confined decomposition of metal fluorides, *Nat. Chem.* 11(8), 730 (2019)
12. H. U. Kim, V. Kanade, M. Kim, K. S. Kim, B. S. An, H. Seok, H. Yoo, L. E. Chaney, S. I. Kim, C. W. Yang, G. Y. Yeom, D. Whang, J. H. Lee, and T. Kim, Wafer-scale and low-temperature growth of 1T-WS_2 film for efficient and stable hydrogen evolution reaction, *Small* 16(6), 1905000 (2020)
13. Y. C. Lin, C. H. Yeh, H. C. Lin, M. D. Siao, Z. Liu, H. Nakajima, T. Okazaki, M. Y. Chou, K. Suenaga, and P. W. Chiu, Stable 1T tungsten disulfide monolayer and its junctions: Growth and atomic structures, *ACS Nano* 12(12), 12080 (2018)
14. J. Gao, Y. D. Kim, L. Liang, J. C. Idrobo, P. Chow, J. Tan, B. Li, L. Li, B. G. Sumpter, T. M. Lu, V. Meunier, J. Hone, and N. Koratkar, Transition-metal substitution doping in synthetic atomically thin semiconductors, *Adv. Mater.* 28(44), 9735 (2016)
15. S. Umrao, J. Jeon, S. M. Jeon, Y. J. Choi, and S. Lee, A homogeneous atomic layer $MoS_{2(1-x)}$ Se_{2x} alloy prepared by low-pressure chemical vapor deposition, and its properties, *Nanoscale* 9(2), 594 (2017)
16. Y. Yoo, Z. P. Degregorio, and J. E. Johns, Seed crystal homogeneity controls lateral and vertical heteroepitaxy of monolayer MoS_2 and WS_2, *J. Am. Chem. Soc.* 137(45), 14281 (2015)
17. Y. Gao, Y. L. Hong, L. C. Yin, Z. Wu, Z. Yang, M. L. Chen, Z. Liu, T. Ma, D. M. Sun, Z. Ni, X. L. Ma, H. M. Cheng, and W. Ren, Ultrafast growth of high-quality monolayer WSe_2 on Au, *Adv. Mater.* 29(29), 1700990 (2017)
18. J. Chen, X. Zhao, G. Grinblat, Z. Chen, S. J. Tan, W. Fu, Z. Ding, I. Abdelwahab, Y. Li, D. Geng, Y. Liu, K. Leng, B. Liu, W. Liu, W. Tang, S. A. Maier, S. J. Pennycook, and K. P. Loh, Homoepitaxial growth of large-scale highly organized transition metal dichalcogenide patterns, *Adv. Mater.* 30(4), 1704674 (2018)
19. S. Y. Kim, J. Kwak, C. V. Ciobanu, and S. Y. Kwon, Recent developments in controlled vapor-phase growth of 2D group 6 transition metal dichalcogenides, *Adv. Mater.* 31(20), 1804939 (2019)
20. H. Li, X. Wang, X. Zhu, X. Duan, and A. Pan, Composition modulation in one-dimensional and two-dimensional chalcogenide semiconductor nanostructures, *Chem. Soc. Rev.* 47(20), 7504 (2018)
21. S. L. Shang, G. Lindwall, Y. Wang, J. M. Redwing, T. Anderson, and Z. K. Liu, Lateral versus vertical growth of two-dimensional layered transition-metal dichalcogenides: Thermodynamic insight into MoS_2,

Nano Lett. 16(9), 5742 (2016)
22. Y. Gong, J. Lin, X. Wang, G. Shi, S. Lei, Z. Lin, X. Zou, G. Ye, R. Vajtai, B. I. Yakobson, H. Terrones, M. Terrones, B. K. Tay, J. Lou, S. T. Pantelides, Z. Liu, W. Zhou, and P. M. Ajayan, Vertical and in-plane heterostructures from WS_2/MoS_2 monolayers, *Nat. Mater.* 13(12), 1135 (2014)
23. P. Yang, X. Zou, Z. Zhang, M. Hong, J. Shi, S. Chen, J. Shu, L. Zhao, S. Jiang, X. Zhou, Y. Huan, C. Xie, P. Gao, Q. Chen, Q. Zhang, Z. Liu, and Y. Zhang, Batch production of 6-inch uniform monolayer molybdenum disulfide catalyzed by sodium in glass, *Nat. Commun.* 9(1), 979 (2018)
24. L. Yu, D. El-Damak, U. Radhakrishna, X. Ling, A. Zubair, Y. Lin, Y. Zhang, M. H. Chuang, Y. H. Lee, D. Antoniadis, J. Kong, A. Chandrakasan, and T. Palacios, Design, modeling, and fabrication of chemical vapor deposition grown MoS_2 circuits with E-mode FETs for large-area electronics, *Nano Lett.* 16(10), 6349 (2016)
25. R. Cheng, F. Wang, L. Yin, Z. Wang, Y. Wen, T. A. Shifa, and J. He, High-performance, multifunctional devices based on asymmetric van der Waals heterostructures, *Nat. Electron.* 1(6), 356 (2018)
26. H. Xue, Y. Dai, W. Kim, Y. Wang, X. Bai, M. Qi, K. Halonen, H. Lipsanen, and Z. Sun, High photoresponsivity and broadband photodetection with a band-engineered $WSe_2/SnSe_2$ heterostructure, *Nanoscale* 11(7), 3240 (2019)
27. L. Yin, P. He, R. Cheng, F. Wang, F. Wang, Z. Wang, Y. Wen, and J. He, Robust trap effect in transition metal dichalcogenides for advanced multifunctional devices, *Nat. Commun.* 10(1), 4133 (2019)
28. M. Si, P. Y. Liao, G. Qiu, Y. Duan, and P. D. Ye, Ferroelectric field-effect transistors based on MoS_2 and $CuInP_2S_6$ two-dimensional van der Waals heterostructure, *ACS Nano* 12(7), 6700 (2018)
29. Y. Wang, X. Bai, J. Chu, H. Wang, G. Rao, X. Pan, X. Du, K. Hu, X. Wang, C. Gong, C. Yin, C. Yang, C. Yan, C. Wu, Y. Shuai, X. Wang, M. Liao, and J. Xiong, Record-low subthreshold-swing negative-capacitance 2D field-effect transistors, *Adv. Mater.* 32(46), 2005353 (2020)
30. B. Zhou, Z. Li, J. Wang, X. Niu, and C. Luan, Tunable valley splitting and an anomalous valley Hall effect in hole-doped WS_2 by proximity coupling with a ferromagnetic MnO_2 monolayer, *Nanoscale* 11(28), 13567 (2019)
31. A. Dankert and S. P. Dash, Electrical gate control of spin current in van der Waals heterostructures at room temperature, *Nat. Commun.* 8(1), 16093 (2017)
32. O. L. Sanchez, D. Ovchinnikov, S. Misra, A. Allain, and A. Kis, Valley polarization by spin injection in a light-emitting van der Waals heterojunction, *Nano Lett.* 16(9), 5792 (2016)
33. J. Lee, K. F. Mak, and J. Shan, Electrical control of the valley Hall effect in bilayer MoS_2 transistors, *Nat. Nanotechnol.* 11(5), 421 (2016)
34. D. Schmitt, J. P. Bange, W. Bennecke, A. AlMutairi, G. Meneghini, K. Watanabe, T. Taniguchi, D. Steil, D. R. Luke, R. T. Weitz, S. Steil, G. S. M. Jansen, S. Brem, E. Malic, S. Hofmann, M. Reutzel, and S. Mathias, Formation of moiré interlayer excitons in space and time, *Nature* 608(7923), 499 (2022)
35. Z. Zhang, P. Chen, X. Yang, Y. Liu, H. Ma, J. Li, B. Zhao, J. Luo, X. Duan, and X. Duan, Ultrafast growth of large single crystals of monolayer WS_2 and WSe_2, *Natl. Sci. Rev.* 7(4), 737 (2020)
36. M. C. Chang, P. H. Ho, M. F. Tseng, F. Y. Lin, C. H. Hou, I. Lin, H. Wang, P. P. Huang, C. H. Chiang, Y. C. Yang, I. T. Wang, H. Y. Du, C. Y. Wen, J. J. Shyue, C. W. Chen, K. H. Chen, P. W. Chiu, and L. C. Chen, Fast growth of large-grain and continuous MoS_2 films through a self-capping vapor-liquid-solid method, *Nat. Commun.* 11(1), 3682 (2020)
37. Z. Zhang, X. Yang, K. Liu, and R. Wang, Epitaxy of 2D materials toward single crystals, *Adv. Sci. (Weinh.)* 9(8), 2105201 (2022)
38. T. Wu, X. Zhang, Q. Yuan, J. Xue, G. Lu, Z. Liu, H. Wang, H. Wang, F. Ding, Q. Yu, X. Xie, and M. Jiang, Fast growth of inch-sized single-crystalline graphene from a controlled single nucleus on Cu–Ni alloys, *Nat. Mater.* 15(1), 43 (2016)
39. H. Wang, X. Xu, J. Li, L. Lin, L. Sun, X. Sun, S. Zhao, C. Tan, C. Chen, W. Dang, H. Ren, J. Zhang, B. Deng, A. L. Koh, L. Liao, N. Kang, Y. Chen, H. Xu, F. Ding, K. Liu, H. Peng, and Z. Liu, Surface monocrystallization of copper foil for fast growth of large single-crystal graphene under free molecular flow, *Adv. Mater.* 28(40), 8968 (2016)
40. L. Wang, X. Xu, L. Zhang, R. Qiao, M. Wu, Z. Wang, S. Zhang, J. Liang, Z. Zhang, Z. Zhang, W. Chen, X. Xie, J. Zong, Y. Shan, Y. Guo, M. Willinger, H. Wu, Q. Li, W. Wang, P. Gao, S. Wu, Y. Zhang, Y. Jiang, D. Yu, E. Wang, X. Bai, Z. J. Wang, F. Ding, and K. Liu, Epitaxial growth of a 100-square-centimetre single-crystal hexagonal boron nitride monolayer on copper, *Nature* 570(7759), 91 (2019)
41. J. S. Lee, S. H. Choi, S. J. Yun, Y. I. Kim, S. Boandoh, J. H. Park, B. G. Shin, H. Ko, S. H. Lee, Y. M. Kim, Y. H. Lee, K. K. Kim, and S. M. Kim, Wafer-scale single-crystal hexagonal boron nitride film via self-collimated grain formation, *Science* 362(6416), 817 (2018)
42. K. A. N. Duerloo, Y. Li, and E. J. Reed, Structural phase transitions in two-dimensional Mo- and W-dichalcogenide monolayers, *Nat. Commun.* 5(1), 4214 (2014)
43. X. Xu, S. Chen, S. Liu, X. Cheng, W. Xu, P. Li, Y. Wan, S. Yang, W. Gong, K. Yuan, P. Gao, Y. Ye, and L. Dai, Millimeter-scale single-crystalline semiconducting $MoTe_2$ via solid-to-solid phase transformation, *J. Am. Chem. Soc.* 141(5), 2128 (2019)
44. X. Xu, Y. Pan, S. Liu, B. Han, P. Gu, S. Li, W. Xu, Y. Peng, Z. Han, J. Chen, P. Gao, and Y. Ye, Seeded 2D epitaxy of large-area single-crystal films of the van der Waals semiconductor 2H $MoTe_2$, *Science* 372(6538), 195 (2021)
45. G. Fiori, F. Bonaccorso, G. Iannaccone, T. Palacios, D. Neumaier, A. Seabaugh, S. K. Banerjee, and L. Colombo, Electronics based on two-dimensional materials, *Nat. Nanotechnol.* 9(10), 768 (2014)
46. W. M. Arden, The international technology roadmap for semiconductors — Perspectives and challenges for the next 15 years, *Curr. Opin. Solid State Mater. Sci.* 6(5), 371 (2002)
47. Z. Lin, Y. Liu, U. Halim, M. Ding, Y. Liu, Y. Wang, C.

Jia, P. Chen, X. Duan, C. Wang, F. Song, M. Li, C. Wan, Y. Huang, and X. Duan, Solution-processable 2D semiconductors for high-performance large-area electronics, *Nature* 562(7726), 254 (2018)

48. K. Kaasbjerg, K. S. Thygesen, and K. W. Jacobsen, Phonon-limited mobility in n-type single-layer MoS_2 from first principles, *Phys. Rev. B* 85(11), 115317 (2012)
49. N. Li, Q. Wang, C. Shen, Z. Wei, H. Yu, J. Zhao, X. Lu, G. Wang, C. He, L. Xie, J. Zhu, L. Du, R. Yang, D. Shi, and G. Zhang, Large-scale flexible and transparent electronics based on monolayer molybdenum disulfide field-effect transistors, *Nat. Electron.* 3(11), 711 (2020)
50. M. Seol, M. H. Lee, H. Kim, K. W. Shin, Y. Cho, I. Jeon, M. Jeong, H. I. Lee, J. Park, and H. J. Shin, High-throughput growth of Wafer-scale monolayer transition metal dichalcogenide via vertical ostwald ripening, *Adv. Mater.* 32(42), 2003542 (2020)
51. Z. Cai, B. Liu, X. Zou, and H. M. Cheng, Chemical vapor deposition growth and applications of two-dimensional materials and their heterostructures, *Chem. Rev.* 118(13), 6091 (2018)
52. L. H. Zeng, D. Wu, S. H. Lin, C. Xie, H. Y. Yuan, W. Lu, S. P. Lau, Y. Chai, L. B. Luo, Z. J. Li, and Y. H. Tsang, Controlled synthesis of 2D palladium diselenide for sensitive photodetector applications, *Adv. Funct. Mater.* 29(1), 1806878 (2019)
53. P. Lv, X. Zhang, X. Zhang, W. Deng, and J. Jie, High-sensitivity and fast-response graphene/crystalline silicon Schottky junction-based near-IR photodetectors, *IEEE Electron Device Lett.* 34(10), 1337 (2013)
54. Y. Zhang, Y. Yu, L. Mi, H. Wang, Z. Zhu, Q. Wu, Y. Zhang, and Y. Jiang, *In situ* fabrication of vertical multilayered MoS_2/Si homotype heterojunction for high-speed visible-near-infrared photodetectors, *Small* 12(8), 1062 (2016)
55. K. Novoselov, A. Mishchenko, A. Carvalho, and A. H. Castro Neto, 2D materials and van der Waals heterostructures, *Science* 353(6298), aac9439 (2016)
56. J. Shi, X. Chen, L. Zhao, Y. Gong, M. Hong, Y. Huan, Z. Zhang, P. Yang, Y. Li, Q. Zhang, Q. Zhang, L. Gu, H. Chen, J. Wang, S. Deng, N. Xu, and Y. Zhang, Chemical vapor deposition grown wafer-scale 2D tantalum diselenide with robust charge-density-wave order, *Adv. Mater.* 30(44), 1804616 (2018)
57. X. Xi, L. Zhao, Z. Wang, H. Berger, L. Forró, J. Shan, and K. F. Mak, Strongly enhanced charge-density-wave order in monolayer $NbSe_2$, *Nat. Nanotechnol.* 10(9), 765 (2015)
58. D. L. Duong, G. Ryu, A. Hoyer, C. Lin, M. Burghard, and K. Kern, Raman characterization of the charge density wave phase of 1T-$TiSe_2$: From bulk to atomically thin layers, *ACS Nano* 11(1), 1034 (2017)
59. X. Xu, Z. Zhang, J. Dong, D. Yi, J. Niu, M. Wu, L. Lin, R. Yin, M. Li, J. Zhou, S. Wang, J. Sun, X. Duan, P. Gao, Y. Jiang, X. Wu, H. Peng, R. S. Ruoff, Z. Liu, D. Yu, E. Wang, F. Ding, and K. Liu, Ultrafast epitaxial growth of metre-sized single-crystal graphene on industrial Cu foil, *Sci. Bull. (Beijing)* 62(15), 1074 (2017)
60. P. Wang, D. Yang, and X. Pi, Toward wafer-scale production of 2D transition metal chalcogenides, *Adv. Electron. Mater.* 7(8), 2100278 (2021)
61. L. Onsager, Crystal Statistics. I. A two-dimensional model with an order-disorder transition, *Phys. Rev.* 65, 3 (1944)
62. P. C. Hohenberg, Existence of long-range order in one and two dimensions, *Phys. Rev.* 158(2), 383 (1967)
63. N. D. Mermin and H. Wagner, Absence of ferromagnetism or antiferromagnetism in one- or two-dimensional isotropic Heisenberg models, *Phys. Rev. Lett.* 17(22), 1133 (1966)
64. J. M. Kosterlitz and D. Thouless, Long range order and metastability in two dimensional solids and superfluids (Application of dislocation theory), *J. Phys. C* 5(11), L124 (1972)
65. J. M. Kosterlitz and D. J. Thouless, Ordering, metastability and phase transitions in two-dimensional systems, *J. Phys. C* 6(7), 1181 (1973)
66. J. A. Wilson and A. Yoffe, The transition metal dichalcogenides discussion and interpretation of the observed optical, electrical and structural properties, *Adv. Phys.* 18(73), 193 (1969)
67. W. Li, X. Qian, and J. Li, Phase transitions in 2D materials, *Nat. Rev. Mater.* 6(9), 829 (2021)
68. D. H. Keum, S. Cho, J. H. Kim, D. H. Choe, H. J. Sung, M. Kan, H. Kang, J. Y. Hwang, S. W. Kim, H. Yang, K. J. Chang, and Y. H. Lee, Bandgap opening in few-layered monoclinic $MoTe_2$, *Nat. Phys.* 11(6), 482 (2015)
69. W. Hou, A. Azizimanesh, A. Sewaket, T. Peña, C. Watson, M. Liu, H. Askari, and S. M. Wu, Strain-based room-temperature non-volatile $MoTe_2$ ferroelectric phase change transistor, *Nat. Nanotechnol.* 14(7), 668 (2019)
70. S. Cho, S. Kim, J. H. Kim, J. Zhao, J. Seok, D. H. Keum, J. Baik, D. H. Choe, K. J. Chang, K. Suenaga, S. W. Kim, Y. H. Lee, and H. Yang, Phase patterning for ohmic homojunction contact in $MoTe_2$, *Science* 349(6248), 625 (2015)
71. Y. Wang, J. Xiao, H. Zhu, Y. Li, Y. Alsaid, K. Y. Fong, Y. Zhou, S. Wang, W. Shi, Y. Wang, A. Zettl, E. J. Reed, and X. Zhang, Structural phase transition in monolayer $MoTe_2$ driven by electrostatic doping, *Nature* 550(7677), 487 (2017)
72. H. U. Kim, H. Seok, W. S. Kang, and T. Kim, The first progress of plasma-based transition metal dichalcogenide synthesis: A stable 1T phase and promising applications, *Nanoscale Adv.* 4(14), 2962 (2022)
73. J. Q. Zhu, Z. C. Wang, H. Yu, N. Li, J. Zhang, J. L. Meng, M. Z. Liao, J. Zhao, X. B. Lu, L. J. Du, R. Yang, D. Shi, Y. Jiang, and G. Y. Zhang, Argon plasma induced phase transition in monolayer MoS_2, *J. Am. Chem. Soc.* 139(30), 10216 (2017)
74. M. S. Sokolikova, and C. Mattevi, Direct synthesis of metastable phases of 2D transition metal dichalcogenides, *Chem. Soc. Rev.* 49(12), 3952 (2020)
75. M. S. Choi, B. Cheong, C. H. Ra, S. Lee, J. H. Bae, S. Lee, G. D. Lee, C. W. Yang, J. Hone, and W. J. Yoo, Electrically driven reversible phase changes in layered In_2Se_3 crystalline film, *Adv. Mater.* 29(42), 1703568 (2017)
76. W. Zhang and M. Wuttig, Phase change materials and superlattices for non-volatile memories, *Phys. Status Solidi Rapid Res. Lett.* 13(4), 1900130 (2019)

77. S. Mori, S. Hatayama, Y. Shuang, D. Ando, and Y. Sutou, Reversible displacive transformation in MnTe polymorphic semiconductor, *Nat. Commun.* 11(1), 85 (2020)
78. S. J. Lee, Z. Lin, X. Duan, and Y. Huang, Doping on demand in 2D devices, *Nat. Electron.* 3(2), 77 (2020)
79. P. Luo, F. Zhuge, Q. Zhang, Y. Chen, L. Lv, Y. Huang, H. Li, and T. Zhai, Doping engineering and functionalization of two-dimensional metal chalcogenides, *Nanoscale Horiz.* 4(1), 26 (2019)
80. K. Zhang, B. M. Bersch, J. Joshi, R. Addou, C. R. Cormier, C. Zhang, K. Xu, N. C. Briggs, K. Wang, S. Subramanian, K. Cho, S. Fullerton-Shirey, R. M. Wallace, P. M. Vora, and J. A. Robinson, Tuning the electronic and photonic properties of monolayer MoS_2 via in situ rhenium substitutional doping, *Adv. Funct. Mater.* 28(16), 1706950 (2018)
81. A. Nipane, D. Karmakar, N. Kaushik, S. Karande, and S. Lodha, Few-layer MoS_2 p-type devices enabled by selective doping using low energy phosphorus implantation, *ACS Nano* 10(2), 2128 (2016)
82. B. Tang, Z. G. Yu, L. Huang, J. Chai, S. L. Wong, J. Deng, W. Yang, H. Gong, S. Wang, K. W. Ang, Y. W. Zhang, and D. Chi, Direct n-to p-type channel conversion in monolayer/few-layer WS_2 field-effect transistors by atomic nitrogen treatment, *ACS Nano* 12(3), 2506 (2018)
83. X. Tang and L. Z. Kou, 2D Janus transition metal dichalcogenides: Properties and applications, *Phys. Status Solidi B* 259(4), 8 (2022)
84. A. Y. Lu, H. Zhu, J. Xiao, C. P. Chuu, Y. Han, M. H. Chiu, C. C. Cheng, C. W. Yang, K. H. Wei, Y. Yang, Y. Wang, D. Sokaras, D. Nordlund, P. Yang, D. A. Muller, M. Y. Chou, X. Zhang, and L. J. Li, Janus monolayers of transition metal dichalcogenides, *Nat. Nanotechnol.* 12(8), 744 (2017)
85. J. Zhang, S. Jia, I. Kholmanov, L. Dong, D. Er, W. Chen, H. Guo, Z. Jin, V. B. Shenoy, L. Shi, and J. Lou, Janus monolayer transition-metal dichalcogenides, *ACS Nano* 11(8), 8192 (2017)
86. T. Hu, F. Jia, G. Zhao, J. Wu, A. Stroppa, and W. Ren, Intrinsic and anisotropic Rashba spin splitting in Janus transition-metal dichalcogenide monolayers, *Phys. Rev. B* 97(23), 235404 (2018)
87. L. Dong, J. Lou, and V. B. Shenoy, Large in-plane and vertical piezoelectricity in Janus transition metal dichalchogenides, *ACS Nano* 11(8), 8242 (2017)
88. C. Liu, X. Yan, X. Song, S. Ding, D. W. Zhang, and P. Zhou, A semi-floating gate memory based on van der Waals heterostructures for quasi-non-volatile applications, *Nat. Nanotechnol.* 13(5), 404 (2018)
89. W. Shi, S. Kahn, L. Jiang, S. Y. Wang, H. Z. Tsai, D. Wong, T. Taniguchi, K. Watanabe, F. Wang, M. F. Crommie, and A. Zettl, Reversible writing of high-mobility and high-carrier-density doping patterns in two-dimensional van der Waals heterostructures, *Nat. Electron.* 3(2), 99 (2020)
90. J. W. Chen, S. T. Lo, S. C. Ho, S. S. Wong, T. H. Y. Vu, X. Q. Zhang, Y. D. Liu, Y. Y. Chiou, Y. X. Chen, and J. C. Yang, A gate-free monolayer WSe_2 p-n diode, *Nat. Commun.* 9(1), 1 (2018)
91. G. Wu, B. Tian, L. Liu, W. Lv, S. Wu, X. Wang, Y. Chen, J. Li, Z. Wang, S. Wu, H. Shen, T. Lin, P. Zhou, Q. Liu, C. Duan, S. Zhang, X. Meng, S. Wu, W. Hu, X. Wang, J. Chu, and J. Wang, Programmable transition metal dichalcogenide homojunctions controlled by nonvolatile ferroelectric domains, *Nat. Electron.* 3(1), 43 (2020)
92. L. Ju, J. Jr Velasco, E. Huang, S. Kahn, C. Nosiglia, H. Z. Tsai, W. Yang, T. Taniguchi, K. Watanabe, Y. Zhang, G. Zhang, M. Crommie, A. Zettl, and F. Wang, Photoinduced doping in heterostructures of graphene and boron nitride, *Nat. Nanotechnol.* 9(5), 348 (2014)
93. D. Xiang, T. Liu, J. Xu, J. Y. Tan, Z. Hu, B. Lei, Y. Zheng, J. Wu, A. Neto, L. Liu, and W. Chen, Two-dimensional multibit optoelectronic memory with broadband spectrum distinction, *Nat. Commun.* 9(1), 2966 (2018)
94. W. K. Liu, K. M. Whitaker, K. R. Kittilstved, and D. R. Gamelin, Stable photogenerated carriers in magnetic semiconductor nanocrystals, *J. Am. Chem. Soc.* 128(12), 3910 (2006)
95. J. Wang, L. Wang, S. Yu, T. Ding, D. Xiang, and K. Wu, Spin blockade and phonon bottleneck for hot electron relaxation observed in n-doped colloidal quantum dots, *Nat. Commun.* 12(1), 550 (2021)
96. H. Li, H. Liu, L. Zhou, X. Wu, Y. Pan, W. Ji, B. Zheng, Q. Zhang, X. Zhuang, X. Zhu, X. Wang, X. Duan, and A. Pan, Strain-tuning atomic substitution in two-dimensional atomic crystals, *ACS Nano* 12(5), 4853 (2018)
97. X. Liu, J. Wu, W. Yu, L. Chen, Z. Huang, H. Jiang, J. He, Q. Liu, Y. Lu, D. Zhu, W. Liu, P. Cao, S. Han, X. Xiong, W. Xu, J. P. Ao, K. W. Ang, and Z. He, Monolayer $W_xMo_{1-x}S_2$ grown by atmospheric pressure chemical vapor deposition: Bandgap engineering and field effect transistors, *Adv. Funct. Mater.* 27(13), 1606469 (2017)
98. J. Zhou, J. Lin, H. Sims, C. Jiang, C. Cong, J. A. Brehm, Z. Zhang, L. Niu, Y. Chen, Y. Zhou, Y. Wang, F. Liu, C. Zhu, T. Yu, K. Suenaga, R. Mishra, S. T. Pantelides, Z. G. Zhu, W. Gao, Z. Liu, and W. Zhou, Synthesis of co-doped MoS_2 monolayers with enhanced valley splitting, *Adv. Mater.* 32(11), 1906536 (2020)
99. S. Wang, Y. Rong, Y. Fan, M. Pacios, H. Bhaskaran, K. He, and J. H. Warner, Shape evolution of monolayer MoS_2 crystals grown by chemical vapor deposition, *Chem. Mater.* 26(22), 6371 (2014)
100. H. Huang, J. Zha, S. Li, and C. Tan, Two-dimensional alloyed transition metal dichalcogenide nanosheets: Synthesis and applications, *Chin. Chem. Lett.* 33(1), 163 (2022)
101. X. Duan, C. Wang, Z. Fan, G. Hao, L. Kou, U. Halim, H. Li, X. Wu, Y. Wang, J. Jiang, A. Pan, Y. Huang, R. Yu, and X. Duan, Synthesis of $WS_{2x}Se_{2-2x}$ alloy nanosheets with composition-tunable electronic properties, *Nano Lett.* 16(1), 264 (2016)
102. Z. Lai, Q. He, T. H. Tran, D. Repaka, D. D. Zhou, Y. Sun, S. Xi, Y. Li, A. Chaturvedi, C. Tan, B. Chen, G. H. Nam, B. Li, C. Ling, W. Zhai, Z. Shi, D. Hu, V. Sharma, Z. Hu, Y. Chen, Z. Zhang, Y. Yu, X. Renshaw Wang, R. V. Ramanujan, Y. Ma, K. Hippalgaonkar, and H. Zhang, Metastable 1T′-phase group VIB transition metal dichalcogenide crystals, *Nat. Mater.* 20(8), 1113 (2021)
103. W. Wen, Y. Zhu, X. Liu, H. P. Hsu, Z. Fei, Y. Chen, X. Wang, M. Zhang, K. H. Lin, F. S. Huang, Y. P.

Wang, Y. S. Huang, C. H. Ho, P. H. Tan, C. Jin, and L. Xie, Anisotropic spectroscopy and electrical properties of 2D $ReS_{2(1-x)}Se_{2x}$ alloys with distorted 1T structure, *Small* 13(12), 1603788 (2017)

104. D. Wang, X. Zhang, G. Guo, S. Gao, X. Li, J. Meng, Z. Yin, H. Liu, M. Gao, L. Cheng, J. You, and R. Wang, Large-area synthesis of layered $HfS_{2(1-x)}Se_{2x}$ alloys with fully tunable chemical compositions and bandgaps, *Adv. Mater.* 30(44), 1803285 (2018)
105. S. Susarla, A. Kutana, J. A. Hachtel, V. Kochat, A. Apte, R. Vajtai, J. C. Idrobo, B. I. Yakobson, C. S. Tiwary, and P. M. Ajayan, Quaternary 2D transition metal dichalcogenides (TMDs) with tunable bandgap, *Adv. Mater.* 29(35), 1702457 (2017)
106. S. Susarla, J. A. Hachtel, X. Yang, A. Kutana, A. Apte, Z. Jin, R. Vajtai, J. C. Idrobo, J. Lou, B. I. Yakobson, C. S. Tiwary, and P. M. Ajayan, Thermally induced 2D alloy-heterostructure transformation in quaternary alloys, *Adv. Mater.* 30(45), 1804218 (2018)
107. X. Zhang, H. Nan, S. Xiao, X. Wan, X. Gu, A. Du, Z. Ni, and K. K. Ostrikov, Transition metal dichalcogenides bilayer single crystals by reverse-flow chemical vapor epitaxy, *Nat. Commun.* 10(1), 598 (2019)
108. Y. Shi, W. Zhou, A. Y. Lu, W. Fang, Y. H. Lee, A. L. Hsu, S. M. Kim, K. K. Kim, H. Y. Yang, L. J. Li, J. C. Idrobo, and J. Kong, van der Waals epitaxy of MoS_2 layers using graphene as growth templates, *Nano Lett.* 12(6), 2784 (2012)
109. M. Li, Y. Zhu, T. Li, Y. Lin, H. Cai, S. Li, H. Ding, N. Pan, and X. Wang, One-step CVD fabrication and optoelectronic properties of SnS_2/SnS vertical heterostructures, *Inorg. Chem. Front.* 5(8), 1828 (2018)
110. Q. Fu, X. Wang, J. Zhou, J. Xia, Q. Zeng, D. Lv, C. Zhu, X. Wang, Y. Shen, X. Li, Y. Hua, F. Liu, Z. Shen, C. Jin, and Z. Liu, One-step synthesis of metal/semiconductor heterostructure NbS_2/MoS_2, *Chem. Mater.* 30(12), 4001 (2018)
111. L. Zhao, J. Jia, Z. Yang, J. Yu, A. Wang, Y. Sang, W. Zhou, and H. Liu, One-step synthesis of CdS nanoparticles/MoS_2 nanosheets heterostructure on porous molybdenum sheet for enhanced photocatalytic H_2 evolution, *Appl. Catal. B* 210, 290 (2017)
112. R. Ai, X. Guan, J. Li, K. Yao, P. Chen, Z. Zhang, X. Duan, and X. Duan, Growth of single-crystalline cadmium iodide nanoplates, CdI_2/MoS_2 (WS_2, WSe_2) van der Waals heterostructures, and patterned arrays, *ACS Nano* 11(3), 3413 (2017)
113. Y. Shimazaki, I. Schwartz, K. Watanabe, T. Taniguchi, M. Kroner, and A. Imamoğlu, Strongly correlated electrons and hybrid excitons in a moiré heterostructure, *Nature* 580(7804), 472 (2020)
114. Y. Cao, V. Fatemi, A. Demir, S. Fang, S. L. Tomarken, J. Y. Luo, J. D. Sanchez-Yamagishi, K. Watanabe, T. Taniguchi, E. Kaxiras, R. C. Ashoori, and P. Jarillo-Herrero, Correlated insulator behaviour at half-filling in magic-angle graphene superlattices, *Nature* 556(7699), 80 (2018)
115. Y. Cao, V. Fatemi, S. Fang, K. Watanabe, T. Taniguchi, E. Kaxiras, and P. Jarillo-Herrero, Unconventional superconductivity in magic-angle graphene superlattices, *Nature* 556(7699), 43 (2018)
116. G. Chen, L. Jiang, S. Wu, B. Lyu, H. Li, B. L. Chittari, K. Watanabe, T. Taniguchi, Z. Shi, J. Jung, Y. Zhang, and F. Wang, Evidence of a gate-tunable Mott insulator in a trilayer graphene moiré superlattice, *Nat. Phys.* 15(3), 237 (2019)
117. G. Chen, A. L. Sharpe, P. Gallagher, I. T. Rosen, E. J. Fox, L. Jiang, B. Lyu, H. Li, K. Watanabe, T. Taniguchi, J. Jung, Z. Shi, D. Goldhaber-Gordon, Y. Zhang, and F. Wang, Signatures of tunable superconductivity in a trilayer graphene moiré superlattice, *Nature* 572(7768), 215 (2019)
118. E. C. Regan, D. Wang, C. Jin, M. I. Bakti Utama, B. Gao, X. Wei, S. Zhao, W. Zhao, Z. Zhang, K. Yumigeta, M. Blei, J. D. Carlström, K. Watanabe, T. Taniguchi, S. Tongay, M. Crommie, A. Zettl, and F. Wang, Mott and generalized Wigner crystal states in WSe_2/WS_2 moiré superlattices, *Nature* 579(7799), 359 (2020)
119. H. S. Arora, R. Polski, Y. Zhang, A. Thomson, Y. Choi, H. Kim, Z. Lin, I. Z. Wilson, X. Xu, J. H. Chu, K. Watanabe, T. Taniguchi, J. Alicea, and S. Nadj-Perge, Superconductivity in metallic twisted bilayer graphene stabilized by WSe_2, *Nature* 583(7816), 379 (2020)
120. C. Jin, E. C. Regan, A. Yan, M. Iqbal Bakti Utama, D. Wang, S. Zhao, Y. Qin, S. Yang, Z. Zheng, S. Shi, K. Watanabe, T. Taniguchi, S. Tongay, A. Zettl, and F. Wang, Observation of moiré excitons in WSe_2/WS_2 heterostructure superlattices, *Nature* 567(7746), 76 (2019)
121. Y. Tang, L. Li, T. Li, Y. Xu, S. Liu, K. Barmak, K. Watanabe, T. Taniguchi, A. H. MacDonald, J. Shan, and K. F. Mak, Simulation of Hubbard model physics in WSe_2/WS_2 moiré superlattices, *Nature* 579(7799), 353 (2020)
122. F. Wu, T. Lovorn, E. Tutuc, and A. H. MacDonald, Hubbard model physics in transition metal dichalcogenide moiré bands, *Phys. Rev. Lett.* 121(2), 026402 (2018)
123. X. Q. Zhang, C. H. Lin, Y. W. Tseng, K. H. Huang, and Y. H. Lee, Synthesis of lateral heterostructures of semiconducting atomic layers, *Nano Lett.* 15(1), 410 (2015)
124. S. Goossens, G. Navickaite, C. Monasterio, S. Gupta, J. J. Piqueras, R. Pérez, G. Burwell, I. Nikitskiy, T. Lasanta, T. Galán, E. Puma, A. Centeno, A. Pesquera, A. Zurutuza, G. Konstantatos, and F. Koppens, Broadband image sensor array based on graphene–CMOS integration, *Nat. Photonics* 11(6), 366 (2017)
125. X. Duan, C. Wang, J. C. Shaw, R. Cheng, Y. Chen, H. Li, X. Wu, Y. Tang, Q. Zhang, A. Pan, J. Jiang, R. Yu, Y. Huang, and X. Duan, Lateral epitaxial growth of two-dimensional layered semiconductor heterojunctions, *Nat. Nanotechnol.* 9(12), 1024 (2014)
126. G. Shao, Y. Lu, J. Hong, X. X. Xue, J. Huang, Z. Xu, X. Lu, Y. Jin, X. Liu, H. Li, S. Hu, K. Suenaga, Z. Han, Y. Jiang, S. Li, Y. Feng, A. Pan, Y. C. Lin, Y. Cao, and S. Liu, Seamlessly splicing metallic $Sn_xMo_{1-x}S_2$ at MoS_2 edge for enhanced photoelectrocatalytic performance in microreactor, *Adv. Sci. (Weinh.)* 7(24), 2002172 (2020)
127. X. Zhang, Z. Jin, L. Wang, J. A. Hachtel, E. Villarreal, Z. Wang, T. Ha, Y. Nakanishi, C. S. Tiwary, J. Lai, L. Dong, J. Yang, R. Vajtai, E. Ringe, J. C. Idrobo, B. I.

Yakobson, J. Lou, V. Gambin, R. Koltun, and P. M. Ajayan, Low contact barrier in 2H/1T′ $MoTe_2$ in-plane heterostructure synthesized by chemical vapor deposition, *ACS Appl. Mater. Interfaces* 11(13), 12777 (2019)

128. K. Ye, L. X. Liu, Y. J. Liu, A. M. Nie, K. Zhai, J. Y. Xiang, B. C. Wang, F. S. Wen, C. P. Mu, Z. S. Zhao, Y. J. Gong, Z. Y. Liu, and Y. J. Tian, Lateral bilayer MoS_2-WS_2 heterostructure photodetectors with high responsivity and detectivity, *Adv. Opt. Mater.* 7(20), 1900815 (2019)
129. Y. D. Yoo, Z. P. Degregorio, and J. E. Johns, Seed crystal homogeneity controls lateral and vertical heteroepitaxy of monolayer MoS_2 and WS_2, *J. Am. Chem. Soc.* 137(45), 14281 (2015)
130. Z. Zhang, Z. Huang, J. Li, D. Wang, Y. Lin, X. Yang, H. Liu, S. Liu, Y. Wang, B. Li, X. Duan, and X. Duan, Endoepitaxial growth of monolayer mosaic heterostructures, *Nat. Nanotechnol.* 17(5), 493 (2022)
131. K. Bogaert, S. Liu, J. Chesin, D. Titow, S. Gradecak, and S. Garaj, Diffusion-mediated synthesis of MoS_2/WS_2 lateral heterostructures, *Nano Lett.* 16(8), 5129 (2016)
132. H. L. Li, X. P. Wu, H. J. Liu, B. Y. Zheng, Q. L. Zhang, X. L. Zhu, Z. We, X. J. Zhuang, H. Zhou, W. X. Tang, X. F. Duan, and A. L. Pan, Composition-modulated two-dimensional semiconductor lateral heterostructures via layer-selected atomic substitution, *ACS Nano* 11(1), 961 (2017)
133. X. F. Li, M. W. Lin, J. H. Lin, B. Huang, A. A. Puretzky, C. Ma, K. Wang, W. Zhou, S. T. Pantelides, M. F. Chi, I. Kravchenko, J. Fowlkes, C. M. Rouleau, D. B. Geohegan, and K. Xiao, Two-dimensional GaSe/$MoSe_2$ misfit bilayer heterojunctions by van der Waals epitaxy, *Sci. Adv.* 2(4), e1501882 (2016)
134. G. L. Shao, Y. Z. Lu, J. H. Hong, X. X. Xue, J. Q. Huang, Z. Y. Xu, X. C. Lu, Y. Y. Jin, X. Liu, H. M. Li, S. Hu, K. Suenaga, Z. Han, Y. Jiang, S. S. Li, Y. X. Feng, A. L. Pan, Y. C. Lin, Y. Cao, and S. Liu, Seamlessly splicing metallic $Sn_xMo_{1-x}S_2$ at MoS_2 edge for enhanced photoelectrocatalytic performance in microreactor, *Adv. Sci. (Weinh.)* 7(24), 2002172 (2020)
135. M. L. Tsai, M. Y. Li, J. R. D. Retamal, K. T. Lam, Y. C. Lin, K. Suenaga, L. J. Chen, G. Liang, L. J. Li, and J. H. He, Single atomically sharp lateral monolayer p–n heterojunction solar cells with extraordinarily high power conversion efficiency, *Adv. Mater.* 29(32), 1701168 (2017)
136. P. K. Sahoo, S. Memaran, Y. Xin, L. Balicas, and H. R. Gutiérrez, One-pot growth of two-dimensional lateral heterostructures via sequential edge-epitaxy, *Nature* 553(7686), 63 (2018)
137. Z. Zhou, Y. Zhang, X. Zhang, X. Niu, G. Wu, and J. Wang, Suppressing photoexcited electron–hole recombination in $MoSe_2$/WSe_2 lateral heterostructures via interface-coupled state engineering: A time-domain *ab initio* study, *J. Mater. Chem. A* 8(39), 20621 (2020)
138. Y. Liu, X. Duan, H. J. Shin, S. Park, Y. Huang, and X. Duan, Promises and prospects of two-dimensional transistors, *Nature* 591(7848), 43 (2021)
139. L. Cheng, and Y. Liu, What limits the intrinsic mobility of electrons and holes in two dimensional metal dichalcogenides, *J. Am. Chem. Soc.* 140(51), 17895 (2018)
140. S. K. Pandey, H. Alsalman, J. G. Azadani, N. Izquierdo, T. Low, and S. A. Campbell, Controlled p-type substitutional doping in large-area monolayer WSe_2 crystals grown by chemical vapor deposition, *Nanoscale* 10(45), 21374 (2018)
141. S. S. Han, J. H. Kim, C. Noh, J. H. Kim, E. Ji, J. Kwon, S. M. Yu, T. J. Ko, E. Okogbue, K. H. Oh, H. S. Chung, Y. J. Jung, G. H. Lee, and Y. Jung, Horizontal-to-vertical transition of 2D layer orientation in low-temperature chemical vapor deposition-grown $PtSe_2$ and its influences on electrical properties and device applications, *ACS Appl. Mater. Interfaces* 11(14), 13598 (2019)
142. Y. Gu, H. Cai, J. Dong, Y. Yu, A. N. Hoffman, C. Liu, A. D. Oyedele, Y. C. Lin, Z. Ge, A. A. Puretzky, G. Duscher, M. F. Chisholm, P. D. Rack, C. M. Rouleau, Z. Gai, X. Meng, F. Ding, D. B. Geohegan, and K. Xiao, Two-dimensional palladium diselenide with strong in-plane optical anisotropy and high mobility grown by chemical vapor deposition, *Adv. Mater.* 32(19), 1906238 (2020)
143. J. Wu, C. Qiu, H. Fu, S. Chen, C. Zhang, Z. Dou, C. Tan, T. Tu, T. Li, Y. Zhang, Z. Zhang, L. M. Peng, P. Gao, B. Yan, and H. Peng, Low residual carrier concentration and high mobility in 2D semiconducting Bi_2O_2Se, *Nano Lett.* 19(1), 197 (2019)
144. P. Kang, V. Michaud-Rioux, X. Kong, G. Yu, and H. Guo, Calculated carrier mobility of h-BN/γ-InSe/h-BN van der Waals heterostructures, *2D Mater.* 4(4), 045014 (2017)
145. L. Xie, M. Liao, S. Wang, H. Yu, L. Du, J. Tang, J. Zhao, J. Zhang, P. Chen, X. Lu, G. Wang, G. Xie, R. Yang, D. Shi, and G. Zhang, Graphene-contacted ultrashort channel monolayer MoS_2 transistors, *Adv. Mater.* 29(37), 1702522 (2017)
146. A. Nourbakhsh, A. Zubair, R. N. Sajjad, A. Tavakkoli K. G, W. Chen, S. Fang, X. Ling, J. Kong, M. S. Dresselhaus, E. Kaxiras, K. K. Berggren, D. Antoniadis, and T. Palacios, MoS_2 field-effect transistor with sub-10 nm channel length, *Nano Lett.* 16(12), 7798 (2016)
147. X. Zou, L. Liu, J. Xu, H. Wang, and W. M. Tang, Few-layered MoS_2 field-effect transistors with a vertical channel of sub-10 nm, *ACS Appl. Mater. Interfaces* 12(29), 32943 (2020)
148. H. Zhang, B. Shi, L. Xu, J. Yan, W. Zhao, Z. Zhang, Z. Zhang, and J. Lu, Sub-5 nm monolayer MoS_2 transistors toward low-power devices, *ACS Appl. Electron. Mater.* 3(4), 1560 (2021)
149. F. Wu, H. Tian, Y. Shen, Z. Hou, J. Ren, G. Gou, Y. Sun, Y. Yang, and T. L. Ren, Vertical MoS_2 transistors with sub-1-nm gate lengths, *Nature* 603(7900), 259 (2022)
150. A. Daus, S. Vaziri, V. Chen, Ç. Köroğlu, R. W. Grady, C. S. Bailey, H. R. Lee, K. Schauble, K. Brenner, and E. Pop, High-performance flexible nanoscale transistors based on transition metal dichalcogenides, *Nat. Electron.* 4(7), 495 (2021)
151. Q. Zhang, X. F. Wang, S. H. Shen, Q. Lu, X. Liu, H. Li, J. Zheng, C. P. Yu, X. Zhong, L. Gu, T. L. Ren, and L. Jiao, Simultaneous synthesis and integration of two-dimensional electronic components, *Nat. Electron.* 2(4), 164 (2019)
152. Z. Q. Fan, X. W. Jiang, J. Chen, and J. W. Luo,

Improving performances of in-plane transition-metal dichalcogenide Schottky barrier field-effect transistors, *ACS Appl. Mater. Interfaces* 10(22), 19271 (2018)
153. M. H. Chiu, H. L. Tang, C. C. Tseng, Y. Han, A. Aljarb, J. K. Huang, Y. Wan, J. H. Fu, X. Zhang, W. H. Chang, D. A. Muller, T. Takenobu, V. Tung, and L. J. Li, Metal-guided selective growth of 2D materials: Demonstration of a bottom-up CMOS inverter, *Adv. Mater.* 31(18), 1900861 (2019)
154. V. P. H. Hu, C. W. Su, Y. W. Lee, T. Y. Ho, C. C. Cheng, T. C. Chen, T. Y. T. Hung, J. F. Li, Y. G. Chen, and L. J. Li, Energy-efficient monolithic 3-D SRAM cell with BEOL MoS_2 FETs for SoC scaling, *IEEE Trans. Electron Dev.* 67(10), 4216 (2020)
155. V. P. H. Hu, C. W. Su, C. C. Yu, C. J. Liu, and C. Y. Weng, in: 2021 IEEE International Symposium on Circuits and Systems (ISCAS), 1–5 (IEEE)
156. C. S. Pang, N. Thakuria, S. K. Gupta, and Z. Chen, in: 2018 IEEE International Electron Devices Meeting (IEDM), 22.22. 21–22.22. 24 (IEEE)
157. C. Navarro, S. Karg, C. Marquez, S. Navarro, C. Convertino, C. Zota, L. Czornomaz, and F. Gamiz, Capacitor-less dynamic random access memory based on a III–V transistor with a gate length of 14 nm, *Nat. Electron.* 2(9), 412 (2019)
158. A. Sebastian, M. Le Gallo, R. Khaddam-Aljameh, and E. Eleftheriou, Memory devices and applications for in-memory computing, *Nat. Nanotechnol.* 15(7), 529 (2020)
159. Y. Wang, H. Tang, Y. Xie, X. Chen, S. Ma, Z. Sun, Q. Sun, L. Chen, H. Zhu, J. Wan, Z. Xu, D. W. Zhang, P. Zhou, and W. Bao, An in-memory computing architecture based on two-dimensional semiconductors for multiply-accumulate operations, *Nat. Commun.* 12(1), 3347 (2021)
160. S. Wang, X. Liu, and P. Zhou, The road for 2D semiconductors in the silicon age, *Adv. Mater.* 34(48), 2106886 (2021)
161. E. Yoshida and T. Tanaka, A capacitorless 1T-DRAM technology using gate-induced drain-leakage (GIDL) current for low-power and high-speed embedded memory, *IEEE Trans. Electron Dev.* 53(4), 692 (2006)
162. G. Migliato Marega, Y. Zhao, A. Avsar, Z. Wang, M. Tripathi, A. Radenovic, and A. Kis, Logic-in-memory based on an atomically thin semiconductor, *Nature* 587(7832), 72 (2020)
163. A. Di Bartolomeo, L. Genovese, F. Giubileo, L. Iemmo, G. Luongo, T. Foller, and M. Schleberger, Hysteresis in the transfer characteristics of MoS_2 transistors, *2D Mater.* 5(1), 015014 (2017)
164. T. Liu, D. Xiang, Y. Zheng, Y. Wang, X. Wang, L. Wang, J. He, L. Liu, and W. Chen, Nonvolatile and programmable photodoping in $MoTe_2$ for photoresist-free complementary electronic devices, *Adv. Mater.* 30(52), 1804470 (2018)
165. K. Tang, Y. Wang, C. Gong, C. Yin, M. Zhang, X. Wang, and J. Xiong, Electronic and photoelectronic memristors based on 2D materials, *Adv. Electron. Mater.* 8(4), 2101099 (2022)
166. S. G. Sarwat, B. Kersting, T. Moraitis, V. P. Jonnalagadda, and A. Sebastian, Phase-change memtransistive synapses for mixed-plasticity neural computations, *Nat. Nanotechnol.* 17(5), 507 (2022)
167. V. K. Sangwan, H. S. Lee, H. Bergeron, I. Balla, M. E. Beck, K. S. Chen, and M. C. Hersam, Multi-terminal memtransistors from polycrystalline monolayer molybdenum disulfide, *Nature* 554(7693), 500 (2018)
168. R. Xu, H. Jang, M. H. Lee, D. Amanov, Y. Cho, H. Kim, S. Park, H. Shin, and D. Ham, Vertical MoS_2 double-layer memristor with electrochemical metallization as an atomic-scale synapse with switching thresholds approaching 100 mV, *Nano Lett.* 19(4), 2411 (2019)
169. A. Karmakar, A. Al-Mahboob, C. E. Petoukhoff, O. Kravchyna, N. S. Chan, T. Taniguchi, K. Watanabe, and K. M. Dani, Dominating interlayer resonant energy transfer in type-II 2D heterostructure, *ACS Nano* 16(3), 3861 (2022)
170. K. A. Zhang, T. N. Zhang, G. H. Cheng, T. X. Li, S. X. Wang, W. Wei, X. H. Zhou, W. W. Yu, Y. Sun, P. Wang, D. Zhang, C. G. Zeng, X. J. Wang, W. D. Hu, H. J. Fan, G. Z. Shen, X. Chen, X. F. Duan, K. Chang, and N. Dai, Interlayer transition and infrared photodetection in atomically thin type-II $MoTe_2/MoS_2$ van der Waals heterostructures, *ACS Nano* 10(3), 3852 (2016)
171. H. Xue, Y. Y. Dai, W. Kim, Y. D. Wang, X. Y. Bai, M. Qi, K. Halonen, H. Lipsanen, and Z. P. Sun, High photoresponsivity and broadband photodetection with a band-engineered $WSe_2/SnSe_2$ heterostructure, *Nanoscale* 11(7), 3240 (2019)
172. C. J. Zhou, S. Raju, B. Li, M. Chan, Y. Chai, and C. Y. Yang, Self-driven metal–semiconductor–metal WSe_2 photodetector with asymmetric contact geometries, *Adv. Funct. Mater.* 28(45), 1802954 (2018)
173. J. Yuan, T. Sun, Z. X. Hu, W. Z. Yu, W. L. Ma, K. Zhang, B. Q. Sun, S. P. Lau, Q. L. Bao, S. H. Lin, and S. J. Li, Wafer-scale fabrication of two-dimensional $PtS_2/PtSe_2$ heterojunctions for efficient and broad band photodetection, *ACS Appl. Mater. Interfaces* 10(47), 40614 (2018)
174. D. Wu, Y. E. Wang, L. H. Zeng, C. Jia, E. P. Wu, T. T. Xu, Z. F. Shi, Y. T. Tian, X. J. Li, and Y. H. Tsang, Design of 2D layered $PtSe_2$ heterojunction for the high-performance, room-temperature, broadband, infrared photodetector, *ACS Photonics* 5(9), 3820 (2018)
175. Y. Li, J. Fu, X. Y. Mao, C. Chen, H. Liu, M. Gong, and H. L. Zeng, Enhanced bulk photovoltaic effect in two-dimensional ferroelectric $CuInP_2S_6$, *Nat. Commun.* 12(1), 5896 (2021)
176. V. M. Fridkin, Bulk photovoltaic effect in noncentrosymmetric crystals, *Crystallogr. Rep.* 46(4), 654 (2001)
177. A. M. Cook, B. M. Fregoso, F. de Juan, S. Coh, and J. E. Moore, Design principles for shift current photovoltaics, *Nat. Commun.* 8(1), 14176 (2017)
178. Y. J. Zhang, T. Ideue, M. Onga, F. Qin, R. Suzuki, A. Zak, R. Tenne, J. H. Smet, and Y. Iwasa, Enhanced intrinsic photovoltaic effect in tungsten disulfide nanotubes, *Nature* 570(7761), 349 (2019)
179. T. Akamatsu, T. Ideue, L. Zhou, Y. Dong, S. Kitamura, M. Yoshii, D. Y. Yang, M. Onga, Y. Nakagawa, K. Watanabe, T. Taniguchi, J. Laurienzo, J. W. Huang, Z. L. Ye, T. Morimoto, H. T. Yuan, and Y. Iwasa, A van der Waals interface that creates in-plane polarization and a spontaneous photovoltaic effect, *Science* 372(6537), 68 (2021)

180. J. Jiang, Z. Z. Chen, Y. Hu, Y. Xiang, L. F. Zhang, Y. P. Wang, G. C. Wang, and J. Shi, Flexo-photovoltaic effect in MoS_2, *Nat. Nanotechnol.* 16(8), 894 (2021)
181. Q. S. Wang, Y. Wen, K. M. Cai, R. Q. Cheng, L. Yin, Y. Zhang, J. Li, Z. X. Wang, F. Wang, F. M. Wang, T. A. Shifa, C. Jiang, H. Yang, and J. He, Nonvolatile infrared memory in MoS_2/PbS van der Waals heterostructures, *Sci. Adv.* 4(4), eaap7916 (2018)
182. L. Yin, P. He, R. Q. Cheng, F. Wang, F. M. Wang, Z. X. Wang, Y. Wen, and J. He, Robust trap effect in transition metal dichalcogenides for advanced multi-functional devices, *Nat. Commun.* 10(1), 4133 (2019)
183. M. O'Neil, J. Marohn, and G. McLendon, Dynamics of electron-hole pair recombination in semiconductor clusters, *J. Phys. Chem.* 94(10), 4356 (1990)
184. Y. C. Jiang, A. P. He, R. Zhao, Y. Chen, G. Z. Liu, H. Lu, J. L. Zhang, Q. Zhang, Z. Wang, C. Zhao, M. S. Long, W. D. Hu, L. Wang, Y. P. Qi, J. Gao, Q. Y. Wu, X. T. Ge, J. Q. Ning, A. T. S. Wee, and C. W. Qiu, Coexistence of photoelectric conversion and storage in van der Waals heterojunctions, *Phys. Rev. Lett.* 127(21), 217401 (2021)
185. J. Junquera and P. Ghosez, Critical thickness for ferroelectricity in perovskite ultrathin films, *Nature* 422(6931), 506 (2003)
186. D. D. Fong, G. B. Stephenson, S. K. Streiffer, J. A. Eastman, O. Auciello, P. H. Fuoss, and C. Thompson, Ferroelectricity in ultrathin perovskite films, *Science* 304(5677), 1650 (2004)
187. S. N. Shirodkar and U. V. Waghmare, Emergence of ferroelectricity at a metal-semiconductor transition in a 1T monolayer of MoS_2, *Phys. Rev. Lett.* 112(15), 157601 (2014)
188. S. G. Yuan, X. Luo, H. L. Chan, C. C. Xiao, Y. W. Dai, M. H. Xie, and J. H. Hao, Room-temperature ferroelectricity in $MoTe_2$ down to the atomic monolayer limit, *Nat. Commun.* 10(1), 1775 (2019)
189. Z. Y. Fei, W. J. Zhao, T. A. Palomaki, B. S. Sun, M. K. Miller, Z. Y. Zhao, J. Q. Yan, X. D. Xu, and D. H. Cobden, Ferroelectric switching of a two-dimensional metal, *Nature* 560(7718), 336 (2018)
190. W. H. Huang, F. Wang, L. Yin, R. Q. Cheng, Z. X. Wang, M. G. Sendeku, J. J. Wang, N. N. Li, Y. Y. Yao, and J. He, Gate-coupling-enabled robust hysteresis for nonvolatile memory and programmable rectifier in van der Waals ferroelectric heterojunctions, *Adv. Mater.* 32(14), 1908040 (2020)
191. Q. Zhang, H. Xiong, Q. F. Wang, L. P. Xu, M. H. Deng, J. Z. Zhang, D. Fuchs, W. W. Li, L. Y. Shang, Y. W. Li, Z. G. Hu, and J. H. Chu, Tunable multi-bit nonvolatile memory based on ferroelectric field-effect transistors, *Adv. Electron. Mater.* 8(5), 2101189 (2022)
192. J. Jo and C. Shin, Negative capacitance field effect transistor with hysteresis-free sub-60-mV/decade switching, *IEEE Electron Device Lett.* 37(3), 245 (2016)
193. X. Q. Liu, R. R. Liang, G. Y. Gao, C. F. Pan, C. S. Jiang, Q. Xu, J. Luo, X. M. Zou, Z. Y. Yang, L. Liao, and Z. L. Wang, MoS_2 negative-capacitance field-effect transistors with subthreshold swing below the physics limit, *Adv. Mater.* 30(28), 1800932 (2018)
194. F. Wang, J. Liu, W. H. Huang, R. Q. Cheng, L. Yin, J. J. Wang, M. G. Sendeku, Y. Zhang, X. Y. Zhan, C. X. Shan, Z. X. Wang, and J. He, Subthermionic field-effect transistors with sub-5 nm gate lengths based on van der Waals ferroelectric heterostructures, *Sci. Bull. (Beijing)* 65(17), 1444 (2020)
195. Y. Wang, X. Y. Bai, J. W. Chu, H. B. Wang, G. F. Rao, X. Q. Pan, X. C. Du, K. Hu, X. P. Wang, C. H. Gong, C. J. Yin, C. Yang, C. Y. Yan, C. Y. Wu, Y. Shuai, X. F. Wang, M. Liao, and J. Xiong, Record-low Subthreshold-Swing negative-capacitance 2D field-effect transistors, *Adv. Mater.* 32(46), 2005353 (2020)
196. C. G. Qiu, F. Liu, L. Xu, B. Deng, M. M. Xiao, J. Si, L. Lin, Z. Y. Zhang, J. Wang, H. Guo, H. L. Peng, and L. M. Peng, Dirac-source field-effect transistors as energy-efficient, high-performance electronic switches, *Science* 361(6400), 387 (2018)
197. A. Weston, E. G. Castanon, V. Enaldiev, F. Ferreira, S. Bhattacharjee, S. G. Xu, H. Corte-Leon, Z. F. Wu, N. Clark, A. Summerfield, T. Hashimoto, Y. Z. Gao, W. D. Wang, M. Hamer, H. Read, L. Fumagalli, A. V. Kretinin, S. J. Haigh, O. Kazakova, A. K. Geim, V. I. Fal'ko, and R. Gorbachev, Interfacial ferroelectricity in marginally twisted 2D semiconductors, *Nat. Nanotechnol.* 17(4), 390 (2022)
198. Z. Wen, C. Li, D. Wu, A. D. Li, and N. B. Ming, Ferroelectric-field-effect-enhanced electroresistance in metal/ferroelectric/semiconductor tunnel junctions, *Nat. Mater.* 12(7), 617 (2013)
199. T. Li, P. Sharma, A. Lipatov, H. Lee, J. W. Lee, M. Y. Zhuravlev, T. R. Paudel, Y. A. Genenko, C. B. Eom, E. Y. Tsymbal, A. Sinitskii, and A. Gruverman, Polarization-mediated modulation of electronic and transport properties of hybrid MoS_2–$BaTiO_3$–$SrRuO_3$ tunnel junctions, *Nano Lett.* 17(2), 922 (2017)
200. P. Chaudhary, P. Buragohain, M. Kozodaev, S. Zarubin, V. Mikheev, A. Chouprik, A. Lipatov, A. Sinitskii, A. Zenkevich, and A. Gruverman, Electroresistance effect in MoS_2–$Hf_{0.5}Zr_{0.5}O_2$ heterojunctions, *Appl. Phys. Lett.* 118(8), 083106 (2021)
201. M. H. Park, Y. H. Lee, H. J. Kim, Y. J. Kim, T. Moon, K. D. Kim, J. Muller, A. Kersch, U. Schroeder, T. Mikolajick, and C. S. Hwang, Ferroelectricity and antiferroelectricity of doped thin HfO_2-based films, *Adv. Mater.* 27(11), 1811 (2015)
202. A. Chernikova, M. Kozodaev, A. Markeev, D. Negrov, M. Spiridonov, S. Zarubin, O. Bak, P. Buragohain, H. Lu, E. Suvorova, A. Gruverman, and A. Zenkevich, Ultrathin $Hf_{0.5}Zr_{0.5}O_2$ ferroelectric films on Si, *ACS Appl. Mater. Interfaces* 8(11), 7232 (2016)
203. F. Ambriz-Vargas, G. Kolhatkar, M. Broyer, A. Hadj-Youssef, R. Nouar, A. Sarkissian, R. Thomas, C. Gomez-Yanez, M. A. Gauthier, and A. Ruediger, A complementary metal oxide semiconductor process-compatible ferroelectric tunnel junction, *ACS Appl. Mater. Interfaces* 9(15), 13262 (2017)
204. A. Chouprik, A. Chernikova, A. Markeev, V. Mikheev, D. Negrov, M. Spiridonov, S. Zarubin, and A. Zenkevich, Electron transport across ultrathin ferroelectric $Hf_{0.5}Zr_{0.5}O_2$ films on Si, *Microelectron. Eng.* 178, 250 (2017)
205. H. Ryu, H. N. Wu, F. B. Rao, and W. J. Zhu, Ferroelectric tunneling junctions based on aluminum oxide/zirconium-doped hafnium oxide for neuromorphic computing, *Sci. Rep.* 9(1), 20383 (2019)

206. J. Xiao, Y. Wang, H. Wang, C. D. Pemmaraju, S. Q. Wang, P. Muscher, E. J. Sie, C. M. Nyby, T. P. Devereaux, X. F. Qian, X. Zhang, and A. M. Lindenberg, Berry curvature memory through electrically driven stacking transitions, *Nat. Phys.* 16(10), 1028 (2020)
207. X. R. Wang, K. Yasuda, Y. Zhang, S. Liu, K. Watanabe, T. Taniguchi, J. Hone, L. Fu, and P. Jarillo-Herrero, Interfacial ferroelectricity in rhombohedral-stacked bilayer transition metal dichalcogenides, *Nat. Nanotechnol.* 17(4), 367 (2022)
208. S. Datta and B. Das, Electronic analog of the electrooptic modulator, *Appl. Phys. Lett.* 56(7), 665 (1990)
209. M. Hossain, B. Qin, B. Li, and X. D. Duan, Synthesis, characterization, properties and applications of two-dimensional magnetic materials, *Nano Today* 42, 101338 (2022)
210. A. Dankert, and S. P. Dash, Electrical gate control of spin current in van der Waals heterostructures at room temperature, *Nat. Commun.* 8(1), 16093 (2017)
211. L. A. Benítez, J. F. Sierra, W. Savero Torres, A. Arrighi, F. Bonell, M. V. Costache, and S. O. Valenzuela, Strongly anisotropic spin relaxation in graphene-transition metal dichalcogenide heterostructures at room temperature, *Nat. Phys.* 14(3), 303 (2018)
212. F. J. Jedema, A. T. Filip, and B. J. van Wees, Electrical spin injection and accumulation at room temperature in an all-metal mesoscopic spin valve, *Nature* 410(6826), 345 (2001)
213. S. O. Valenzuela, Nonlocal electronic spin detection, spin accumulation and the spin Hall effect, *Int. J. Mod. Phys. B* 23(11), 2413 (2009)
214. B. Raes, A. W. Cummings, F. Bonell, M. V. Costache, J. F. Sierra, S. Roche, and S. O. Valenzuela, Spin precession in anisotropic media, *Phys. Rev. B* 95(8), 085403 (2017)
215. S. W. Jiang, L. Z. Li, Z. F. Wang, J. Shan, and K. F. Mak, Spin tunnel field-effect transistors based on two-dimensional van der Waals heterostructures, *Nat. Electron.* 2(4), 159 (2019)
216. H. L. Lin, F. G. Yan, C. Hu, Q. S. Lv, W. K. Zhu, Z. A. Wang, Z. M. Wei, K. Chang, and K. Y. Wang, Spin-valve effect in $Fe_3GeTe_2/MoS_2/Fe_3GeTe_2$ van der Waals heterostructures, *ACS Appl. Mater. Interfaces* 12(39), 43921 (2020)
217. W. Yang, Y. Cao, J. C. Han, X. Y. Lin, X. H. Wang, G. D. Wei, C. Lv, A. Bournel, and W. S. Zhao, Spin-filter induced large magnetoresistance in 2D van der Waals magnetic tunnel junctions, *Nanoscale* 13(2), 862 (2021)
218. K. Zollner, M. D. Petrovic, K. Dolui, P. Plechac, B. K. Nikolic, and J. Fabian, Scattering-induced and highly tunable by gate damping-like spin–orbit torque in graphene doubly proximitized by two-dimensional magnet $Cr_2Ge_2Te_6$ and monolayer WS_2, *Phys. Rev. Res.* 2(4), 043057 (2020)
219. R. Fiederling, M. Keim, G. Reuscher, W. Ossau, G. Schmidt, A. Waag, and L. W. Molenkamp, Injection and detection of a spin-polarized current in a light-emitting diode, *Nature* 402(6763), 787 (1999)
220. Y. Ye, J. Xiao, H. L. Wang, Z. L. Ye, H. Y. Zhu, M. Zhao, Y. Wang, J. H. Zhao, X. B. Yin, and X. Zhang, Electrical generation and control of the valley carriers in a monolayer transition metal dichalcogenide, *Nat. Nanotechnol.* 11(7), 598 (2016)
221. D. Zhong, K. L. Seyler, X. Y. Linpeng, N. P. Wilson, T. Taniguchi, K. Watanabe, M. A. McGuire, K. M. C. Fu, D. Xiao, W. Yao, and X. D. Xu, Layer-resolved magnetic proximity effect in van der Waals heterostructures, *Nat. Nanotechnol.* 15(3), 187 (2020)
222. J. Pu and T. Takenobu, Monolayer transition metal dichalcogenides as light sources, *Adv. Mater.* 30(33), 1707627 (2018)
223. Y. J. Zhang, T. Oka, R. Suzuki, J. T. Ye, and Y. Iwasa, Electrically switchable chiral light-emitting transistor, *Science* 344(6185), 725 (2014)
224. J. Lee, Z. F. Wang, H. C. Xie, K. F. Mak, and J. Shan, Valley magnetoelectricity in single-layer MoS_2, *Nat. Mater.* 16(9), 887 (2017)
225. J. Son, K. H. Kim, Y. H. Ahn, H. W. Lee, and J. Lee, Strain engineering of the Berry curvature dipole and valley magnetization in monolayer MoS_2, *Phys. Rev. Lett.* 123(3), 036806 (2019)
226. Y. Y. Chen, J. Q. Ma, Z. Y. Liu, J. Z. Li, X. F. Duan, and D. H. Li, Manipulation of valley pseudospin by selective spin injection in chiral two-dimensional perovskite/monolayer transition metal dichalcogenide heterostructures, *ACS Nano* 14(11), 15154 (2020)
227. J. Pu, W. J. Zhang, H. Matsuoka, Y. Kobayashi, Y. Takaguchi, Y. Miyata, K. Matsuda, Y. Miyauchi, and T. Takenobu, Room-temperature chiral light-emitting diode based on strained monolayer semiconductors, *Adv. Mater.* 33(36), 2100601 (2021)
228. J. R. Schaibley, H. Y. Yu, G. Clark, P. Rivera, J. S. Ross, K. L. Seyler, W. Yao, and X. D. Xu, Valleytronics in 2D materials, *Nat. Rev. Mater.* 1(11), 16055 (2016)
229. A. Rycerz, J. Tworzydlo, and C. W. J. Beenakker, Valley filter and valley valve in graphene, *Nat. Phys.* 3(3), 172 (2007)
230. J. Lee, K. F. Mak, and J. Shan, Electrical control of the valley Hall effect in bilayer MoS_2 transistors, *Nat. Nanotechnol.* 11(5), 421 (2016)
231. C. H. Jin, J. Kim, M. I. B. Utama, E. C. Regan, H. Kleemann, H. Cai, Y. X. Shen, M. J. Shinner, A. Sengupta, K. Watanabe, T. Taniguchi, S. Tongay, A. Zettl, and F. Wang, Imaging of pure spin-valley diffusion current in WS_2–WSe_2 heterostructures, *Science* 360(6391), 893 (2018)
232. D. Unuchek, A. Ciarrocchi, A. Avsar, Z. Sun, K. Watanabe, T. Taniguchi, and A. Kis, Valley-polarized exciton currents in a van der Waals heterostructure, *Nat. Nanotechnol.* 14(12), 1104 (2019)
233. L. F. Li, L. Shao, X. W. Liu, A. Y. Gao, H. Wang, B. J. Zheng, G. Z. Hou, K. Shehzad, L. W. Yu, F. Miao, Y. Shi, Y. Xu, and X. M. Wang, Room-temperature valleytronic transistor, *Nat. Nanotechnol.* 15(9), 743 (2020)
234. C. Y. Jiang, A. Rasmita, H. Ma, Q. H. Tan, Z. W. Zhang, Z. M. Huang, S. Lai, N. Z. Wang, S. Liu, X. Liu, T. Yu, Q. H. Xiong, and W. B. Gao, A room-temperature gate-tunable bipolar valley Hall effect in molybdenum disulfide/tungsten diselenide heterostructures, *Nat. Electron.* 5(1), 23 (2021)
235. J. Ingla-Aynés, F. Herling, J. Fabian, L. E. Hueso, and F. Casanova, Electrical control of valley-Zeeman spin-orbit-coupling-induced spin precession at room temper-

ature, *Phys. Rev. Lett.* 127(4), 047202 (2021)
236. M. S. Hossain, M. K. Ma, K. A. Villegas-Rosales, Y. J. Chung, L. N. Pfeiffer, K. W. West, K. W. Baldwin, and M. Shayegan, Spontaneous valley polarization of itinerant electrons, *Phys. Rev. Lett.* 127(11), 116601 (2021)
237. B. Huang, M. A. McGuire, A. F. May, D. Xiao, P. Jarillo-Herrero, and X. D. Xu, Emergent phenomena and proximity effects in two-dimensional magnets and heterostructures, *Nat. Mater.* 19(12), 1276 (2020)
238. J. Lee, W. Heo, M. Cha, K. Watanabe, T. Taniguchi, J. Kim, S. Cha, D. Kim, M. H. Jo, and H. Choi, Ultrafast non-excitonic valley Hall effect in MoS_2/WTe_2 heterobilayers, *Nat. Commun.* 12(1), 1635 (2021)
239. Y. K. Luo, J. S. Xu, T. C. Zhu, G. Z. Wu, E. J. McCormick, W. B. Zhan, M. R. Neupane, and R. K. Kawakami, Opto-valleytronic spin injection in monolayer MoS_2/few-layer graphene hybrid spin valves, *Nano Lett.* 17(6), 3877 (2017)
240. S. Cha, M. Noh, J. Kim, J. Son, H. Bae, D. Lee, H. Kim, J. Lee, H. S. Shin, S. Sim, S. Yang, S. Lee, W. Shim, C. H. Lee, M. H. Jo, J. S. Kim, D. Kim, and H. Choi, Generation, transport and detection of valley-locked spin photocurrent in WSe_2-graphene-Bi_2Se_3 heterostructures, *Nat. Nanotechnol.* 13(10), 910 (2018)
241. H. T. Yuan, X. Q. Wang, B. Lian, H. J. Zhang, X. F. Fang, B. Shen, G. Xu, Y. Xu, S. C. Zhang, H. Y. Hwang, and Y. Cui, Generation and electric control of spin–valley-coupled circular photogalvanic current in WSe_2, *Nat. Nanotechnol.* 9(10), 851 (2014)
242. A. Rasmita, C. Y. Jiang, H. Ma, Z. R. Ji, R. Agarwal, and W. B. Gao, Tunable geometric photocurrent in van der Waals heterostructure, *Optica* 7(9), 1204 (2020)
243. F. Sattari, and S. Mirershadi, Effect of the strain on spin-valley transport properties in MoS_2 superlattice, *Sci. Rep.* 11(1), 17617 (2021)
244. S. N. Miao, T. M. Wang, X. Huang, D. X. Chen, Z. Lian, C. Wang, M. Blei, T. Taniguchi, K. Watanabe, S. Tongay, Z. H. Wang, D. Xiao, Y. T. Cui, and S. F. Shi, Strong interaction between interlayer excitons and correlated electrons in WSe_2/WS_2 moire superlattice, *Nat. Commun.* 12(1), 3608 (2021)
245. D. Huang, J. Choi, C. K. Shih, and X. Q. Li, Excitons in semiconductor moire superlattices, *Nat. Nanotechnol.* 17(3), 227 (2022)
246. C. H. Bao, P. Z. Tang, D. Sun, and S. Y. Zhou, Light-induced emergent phenomena in 2D materials and topological materials, *Nat. Rev. Phys.* 4(1), 33 (2021)
247. N. P. Wilson, W. Yao, J. Shan, and X. D. Xu, Excitons and emergent quantum phenomena in stacked 2D semiconductors, *Nature* 599(7885), 383 (2021)
248. Y. Y. Wang, F. P. Li, W. Wei, B. B. Huang, and Y. Dai, Interlayer coupling effect in van der Waals heterostructures of transition metal dichalcogenides, *Front. Phys.* 16(1), 13501 (2021)
249. S. Klimmer, O. Ghaebi, Z. Y. Gan, A. George, A. Turchanin, G. Cerullo, and G. Soavi, All-optical polarization and amplitude modulation of second-harmonic generation in atomically thin semiconductors, *Nat. Photonics* 15(11), 837 (2021)
250. D. Wijethunge, L. Zhang, C. Tang, and A. Du, Tuning band alignment and optical properties of 2D van der Waals heterostructure via ferroelectric polarization switching, *Front. Phys.* 15(6), 63504 (2020)
251. Q. Yun, L. Li, Z. Hu, Q. Lu, B. Chen, and H. Zhang, Layered transition metal dichalcogenide-based nanomaterials for electrochemical energy storage, *Adv. Mater.* 32(1), 1903826 (2020)
252. E. Cha, M. D. Patel, J. Park, J. Hwang, V. Prasad, K. Cho, and Choi, MoS_2 as an efficient protective layer for lithium metal anodes in high-performance Li–S batteries, *Nat. Nanotechnol.* 13(4), 337 (2018)
253. J. Yang, A. R. Mohmad, Y. Wang, R. Fullon, X. Song, F. Zhao, I. Bozkurt, M. Augustin, E. J. Santos, H. S. Shin, W. Zhang, D. Voiry, H. Y. Jeong, and M. Chhowalla, Ultrahigh-current-density niobium disulfide catalysts for hydrogen evolution, *Nat. Mater.* 18(12), 1309 (2019)
254. Y. Ouyang, C. Ling, Q. Chen, Z. Wang, L. Shi, and J. Wang, Activating inert basal planes of MoS_2 for hydrogen evolution reaction through the formation of different intrinsic defects, *Chem. Mater.* 28(12), 4390 (2016)
255. Y. He, P. Tang, Z. Hu, Q. He, C. Zhu, L. Wang, Q. Zeng, P. Golani, G. Gao, W. Fu, Z. Huang, C. Gao, J. Xia, X. Wang, X. Wang, C. Zhu, Q. M. Ramasse, A. Zhang, B. An, Y. Zhang, S. Martí-Sánchez, J. R. Morante, L. Wang, B. K. Tay, B. I. Yakobson, A. Trampert, H. Zhang, M. Wu, Q. J. Wang, J. Arbiol, and Z. Liu, Engineering grain boundaries at the 2D limit for the hydrogen evolution reaction, *Nat. Commun.* 11(1), 57 (2020)
256. W. Y. Chen, X. Jiang, S. N. Lai, D. Peroulis, and L. Stanciu, Nanohybrids of a MXene and transition metal dichalcogenide for selective detection of volatile organic compounds, *Nat. Commun.* 11(1), 1302 (2020)
257. W. Su, S. Zhang, C. Liu, Q. Tian, X. Liu, K. Li, Y. Lv, L. Liao, and X. Zou, Interlayer transition induced infrared response in ReS_2/2D Perovskite van der Waals heterostructure photodetector, *Nano Lett.* 22(24), 10192 (2022)
258. Y. Wen, P. He, Y. Yao, Y. Zhang, R. Cheng, L. Yin, N. Li, J. Li, J. Wang, Z. Wang, C. Liu, X. Fang, C. Jiang, Z. Wei, and J. He, Bridging the van der Waals interface for advanced optoelectronic devices, *Adv. Mater.* 32(7), 1906874 (2020)
259. Y. Wen, P. He, Q. Wang, Y. Yao, Y. Zhang, S. Hussain, Z. Wang, R. Cheng, L. Yin, M. Getaye Sendeku, F. Wang, C. Jiang, and J. He, Gapless van der Waals heterostructures for infrared optoelectronic devices, *ACS Nano* 13(12), 14519 (2019)
260. Y. Wen, L. Yin, P. He, Z. Wang, X. Zhang, Q. Wang, T. A. Shifa, K. Xu, F. Wang, X. Zhan, F. Wang, C. Jiang, and J. He, Integrated high-performance infrared phototransistor arrays composed of nonlayered PbS–MoS_2 heterostructures with edge contacts, *Nano Lett.* 16(10), 6437 (2016)
261. Z. Wang, H. Xia, P. Wang, X. Zhou, C. Liu, Q. Zhang, F. Wang, M. Huang, S. Chen, P. Wu, Y. Chen, J. Ye, S. Huang, H. Yan, L. Gu, J. Miao, T. Li, X. Chen, W. Lu, P. Zhou, and W. Hu, Controllable doping in 2D layered materials, *Adv. Mater.* 33(48), 2104942 (2021)
262. X. Zhang, B. Liu, L. Gao, H. Yu, X. Liu, J. Du, J. Xiao, Y. Liu, L. Gu, Q. Liao, Z. Kang, Z. Zhang, and Y. Zhang, Near-ideal van der Waals rectifiers based on all-two-dimensional Schottky junctions, *Nat. Commun.*

12(1), 1522 (2021)
263. Y. Wen, Z. Liu, Y. Zhang, C. Xia, B. Zhai, X. Zhang, G. Zhai, C. Shen, P. He, R. Cheng, L. Yin, Y. Yao, M. Getaye Sendeku, Z. Wang, X. Ye, C. Liu, C. Jiang, C. Shan, Y. Long, and J. He, Tunable room-temperature ferromagnetism in two-dimensional Cr_2Te_3, *Nano Lett.* 20(5), 3130 (2020)
264. Z. Guo, L. Wang, M. Han, E. Zhao, L. Zhu, W. Guo, J. Tan, B. Liu, X. Q. Chen, and J. Lin, One-step growth of bilayer 2H–1T′ $MoTe_2$ van der Waals heterostructures with interlayer-coupled resonant phonon vibration, *ACS Nano* 16(7), 11268 (2022)
265. M. Bian, L. Zhu, X. Wang, J. Choi, R. V. Chopdekar, S. Wei, L. Wu, C. Huai, A. Marga, Q. Yang, Y. C. Li, F. Yao, T. Yu, S. A. Crooker, X. M. Cheng, R. F. Sabirianov, S. Zhang, J. Lin, Y. Hou, and H. Zeng, Dative epitaxy of commensurate monocrystalline covalent van der Waals moiré supercrystal, *Adv. Mater.* 34(17), 2200117 (2022)
266. L. Zhang, G. Wang, Y. Zhang, Z. Cao, Y. Wang, T. Cao, C. Wang, B. Cheng, W. Zhang, X. Wan, J. Lin, S. J. Liang, and F. Miao, Tuning electrical conductance in bilayer MoS_2 through defect-mediated interlayer chemical bonding, *ACS Nano* 14(8), 10265 (2020)
267. L. Tang, R. Xu, J. Tan, Y. Luo, J. Zou, Z. Zhang, R. Zhang, Y. Zhao, J. Lin, X. Zou, B. Liu, and H. M. Cheng, Modulating electronic structure of monolayer transition metal dichalcogenides by substitutional Nb-doping, *Adv. Funct. Mater.* 31(5), 2006941 (2021)
268. J. Zou, Z. Cai, Y. Lai, J. Tan, R. Zhang, S. Feng, G. Wang, J. Lin, B. Liu, and H. M. Cheng, Doping concentration modulation in vanadium-doped monolayer molybdenum disulfide for synaptic transistors, *ACS Nano* 15(4), 7340 (2021)
269. Q. Lv, J. Tan, Z. Wang, L. Yu, B. Liu, J. Lin, J. Li, Z. H. Huang, F. Kang, and R. Lv, Femtomolar-level molecular sensing of monolayer tungsten diselenide induced by heteroatom doping with long-term stability, *Adv. Funct. Mater.* 32(34), 2200273 (2022)
270. J. Lin, J. Zhou, S. Zuluaga, P. Yu, M. Gu, Z. Liu, S. T. Pantelides, and K. Suenaga, Anisotropic ordering in 1T′ molybdenum and tungsten ditelluride layers alloyed with sulfur and selenium, *ACS Nano* 12(1), 894 (2018)
271. P. Yu, J. Lin, L. Sun, Q. L. Le, X. Yu, G. Gao, C. H. Hsu, D. Wu, T. R. Chang, Q. Zeng, F. Liu, Q. J. Wang, H. T. Jeng, H. Lin, A. Trampert, Z. Shen, K. Suenaga, and Z. Liu, Metal-semiconductor phase-transition in $WSe_{2(1-x)}Te_{2x}$ monolayer, *Adv. Mater.* 29(4), 1603991 (2017)
272. Y. Gong, Z. Liu, A. R. Lupini, G. Shi, J. Lin, S. Najmaei, Z. Lin, A. L. Elías, A. Berkdemir, G. You, H. Terrones, M. Terrones, R. Vajtai, S. T. Pantelides, S. J. Pennycook, J. Lou, W. Zhou, and P. M. Ajayan, Band gap engineering and layer-by-layer mapping of selenium-doped molybdenum disulfide, *Nano Lett.* 14(2), 442 (2014)
273. M. Cheng, J. Yang, X. Li, H. Li, R. Du, J. Shi, and J. He, Improving the device performances of two-dimensional semiconducting transition metal dichalcogenides: Three strategies, *Front. Phys.* 17(6), 63601 (2022)
274. P. Luo, C. Liu, J. Lin, X. Duan, W. Zhang, C. Ma, Y. Lv, X. Zou, Y. Liu, F. Schwierz, W. Qin, L. Liao, J. He, and X. Liu, Molybdenum disulfide transistors with enlarged van der Waals gaps at their dielectric interface via oxygen accumulation, *Nat. Electron.* 5(12), 849 (2022)
275. X. Zhang, H. Yu, W. Tang, X. Wei, L. Gao, M. Hong, Q. Liao, Z. Kang, Z. Zhang, and Y. Zhang, All-van-der-Waals barrier-free contacts for high-mobility transistors, *Adv. Mater.* 34(34), 2109521 (2022)
276. X. Zhang, Z. Kang, L. Gao, B. Liu, H. Yu, Q. Liao, Z. Zhang, and Y. Zhang, Molecule-upgraded van der waals contacts for Schottky-barrier-free electronics, *Adv. Mater.* 33(45), 2104935 (2021)
277. W. Huang, F. Wang, L. Yin, R. Cheng, Z. Wang, M. G. Sendeku, J. Wang, N. Li, Y. Yao, and J. He, Gate-coupling-enabled robust hysteresis for nonvolatile memory and programmable rectifier in van der Waals ferroelectric heterojunctions, *Adv. Mater.* 32(14), 1908040 (2020)
278. Z. Yang, L. Liao, F. Gong, F. Wang, Z. Wang, X. Liu, X. Xiao, W. Hu, J. He, and X. Duan, WSe_2/GeSe heterojunction photodiode with giant gate tunability, *Nano Energy* 49, 103 (2018)
279. J. Cao, Z. Wang, X. Zhan, Q. Wang, M. Safdar, Y. Wang, and J. He, Vertical SnSe nanorod arrays: From controlled synthesis and growth mechanism to thermistor and photoresistor, *Nanotechnology* 25(10), 105705 (2014)
280. M. Mirza, J. Wang, L. Wang, J. He, and C. Jiang, Response enhancement mechanism of NO_2 gas sensing in ultrathin pentacene field-effect transistors, *Org. Electron.* 24, 96 (2015)